The Preparation of Silicon and Silver-Based Nanomaterials for Biological Applications

by

Cemre Mertoglu

A thesis submitted in partial fulfillment of the requirements for the degree of

Master of Science

Department of Chemistry
University of Alberta

Abstract

Mesoporous silica nanoparticles (MSNPs) are used in catalysis, drug delivery, controlled drug release, imaging and biosensing applications due to their stability, high pore volumes, large surface area and non-toxicity. Although MSNPs have many advantages in biological applications, they lack optical properties. This limits the functionality of these materials in terms of in-situ response. Therefore, combining mesoporous silica with nanoparticles results in hybrid materials that provide unique systems for biosensing. One drawback of using these hybrid materials in sensing applications is the non-selective nature of the system as the pores of mesoporous silica do not discriminate between the molecules of interest and other molecules in the sensing medium. For this reason, molecular imprinting is essential to produce hybrid materials with the needed selectivity. This thesis focuses on work related to combining the nanoparticles with surface imprinted mesoporous silica. Possible applications of these hybrid materials are then studied.

Chapter 1 introduces the concepts of nanoparticles, mesoporous silica, and molecular imprinting. Synthesis routes, properties and applications of these materials are discussed.

In Chapter 2, we aim to prepare silicon nanoparticles (SiNPs) embedded in surface imprinted mesoporous silica. SiNPs were prepared by high temperature processing of hydrogen silsesquioxane (HSQ) and the surface of the SiNPs were passivated with dodecyl groups. Encapsulation of SiNPs in mesoporous silica (MSNPs-SiNPs) was performed via a sol-gel reaction. Surface modification of MSNPs-SiNPs was achieved by introducing vinyl groups followed by radical initiated polymerization. The polymer (ethylene glycol dimethacrylate) was molecularly imprinted using ibuprofen (IBU) as a template molecule. Throughout this investigation we assessed the surface chemistry of the MSNPs-SiNPs by Fourier-transform infrared (FTIR). The successful preparation of the imprinted polymer on the surface of the particles

was assessed by transmission electron microscopy (TEM) and scanning electron microscopy (SEM). With this hybrid material in hand, we turned our attention toward determining the template loading/release efficiency of the material.

Chapter 3 describes the preparation of AgNPs embedded in surface imprinted mesoporous silica. The AgNPs were prepared using a chemical reduction method and subsequent encapsulation of AgNPs in mesoporous silica was performed via a sol-gel reaction. The surface modification of the AgNPs embedded mesoporous silica was again achieved by the introduction of vinyl groups followed by radical initiated polymerization on the surface of the MSNPs-AgNPs. The polymer (poly(N-isopropyl acrylamide)-co-poly(acrylamide)) was molecularly imprinted using urea as a template molecule. Following the methodology in Chapter 2, the surface chemistry of the MSNPs-AgNPs was investigated using Fourier-transform infrared (FTIR), Thermogravimetric analysis (TGA), and Dynamic light scattering (DLS). The successful preparation of the imprinted polymer on the surface of the particles was evaluated by TGA and Scanning electron microscopy (SEM). Next, we turned our attention toward determining the template loading/release efficiency of this hybrid material.

Finally, Chapter 4 summarizes the outcome of the experimental results and describes relevant future directions.

Preface

This thesis is an original work by Cemre Mertoglu. The research was conducted under the supervision of Professor Jonathan G. C. Veinot at the Department of Chemistry, University of Alberta. No part of this thesis has been published previously.

In Chapter 2, I was responsible for the project scope, experimental planning, data collection, data analysis, and writing the chapter. Sarah Milliken and I Teng (Emily) Cheong helped me with the preparation of silicon nanoparticles. Dr. Jonathan G. C. Veinot supervised the project and was involved with the thesis composition.

In Chapter 3, I was responsible for the project scope, experimental planning, data collection, data analysis, and writing the chapter. Dr. Jonathan G. C. Veinot supervised the project and was involved with the thesis composition.

In Chapter 4, I was responsible for writing the chapter which includes the original ideas for future directions developed by me and with input from my supervisor Dr. Jonathan G. C. Veinot.

Acknowledgements

First, I would like to thank my supervisor, Dr. Jonathan G. C. Veinot, for his support and guidance throughout my graduate study. I deeply appreciate the opportunity he provided. His mentorship has been crucial in shaping my research and academic development, and I am grateful for his dedication.

I would like to thank my supervisory committee members, Dr. Arthur Mar, and Dr. Michael Serpe for their valuable advice and comments throughout my graduate study.

I feel very fortunate to work with the Veinot group. I am especially grateful to Sarah Milliken, I Teng (Emily) Cheong and Kevin O'Connor for helping me to start my research in the group. I would like to thank all the past and present group members, Yingjie (Jay) He, Riley Hooper, Chuyi (Martin) Ni, Jonathan Trach, Cole Butler, Madison Chevalier, Brayden Glockzin, Abbie Rubletz, Mia Dolanjski, Suni Guo, Christina Zafeiridou, Chantell Fernandes and Dominic Lavergne for their support and friendship throughout my study. A special thank you to Dr. John Washington for reviewing this thesis.

I extend my gratitude to the ATUMS community for the opportunity to participate in a research exchange visit at the Technical University of Munich. I am especially thankful to Leah Veinot and Sergei Vagin for their help in organizing my stay in Munich. I would like to thank Prof. Professor Bernhard Rieger for hosting me and allowing me to work in his lab at the Technical University of Munich. I want to express my appreciation to Moritz Kleybolte for helping me with the onboarding process into the research team at the Technical University of Munich.

I would like to thank the technical support staff of the analytical lab, machine shop, electronic shop, and glass shop. I also want to thank NanoFAB and SEM lab staff in the Department of Earth and Atmospheric Sciences.

I am especially grateful to Eric Lautner for his unwavering support and understanding. I appreciate your presence in my life.

I am deeply grateful to my parents, Mustafa and Beyhan Mertoglu for their support throughout this journey. Your encouragement has been crucial to me, allowing me to navigate through challenges, and I cannot thank you enough for always being there for me.

Table of Contents

List of Tables

List of Figures

List of Symbols, Nomenclature and Abbreviations

AgNPs	Silver nanoparticles
alkyl-SiNPs	Alkyl functionalized silicon nanoparticles
°C	Degree Celsius
cm^{-1}	Wavenumber
CTAB	Cetrimonium bromide
DLS	Dynamic light scattering
EDX	Energy dispersive X-ray spectroscopy
FTIR	Fourier transform infrared spectroscopy
HF	Hydrofluoric acid
H-SiNPs	Hydride-terminated SiNPs
HSQ	Hydrogen silsesquioxane
LSPR	Localized surface plasmon resonance
MIPs	Molecular imprinted polymers
MSNPs	Mesoporous silica nanoparticles
MSNPs-SiNPs	Mesoporous silica encapsulated silicon nanoparticles
MSNPs-AgNPs	Mesoporous silica encapsulated silver nanoparticles
MIPs-MSNPs-AgNPs	Surface molecularly imprinted MSNPs-AgNPs
MIPs-MSNPs-SiNPs	Surface molecularly imprinted MSNPs-SiNPs
NIPs-MSNPs-AgNPs	Nonimprinted polymer on the surface of MSNPs-AgNPs
NIPs-MSNPs-SiNPs	Nonimprinted polymer on the surface of MSNPs-SiNPs
nm	Nanometer
PL	Photoluminescence
QD	Quantum dot
SEM	Scanning electron microscopy
SERS	Surface-enhanced Raman scattering
SiNPs	Silicon nanoparticles
SiNPs/SiO_2	Silicon nanoparticles embedded in the silica matrix
SiO_2	Silica

SPR	Surface plasmon resonance
TEM	Transmission electron microscopy
TGA	Thermogravimetric analysis
UV	Ultraviolet
vinyl-MSNPs-AgNPs	Vinyl functionalized MSNPs-AgNPs
vinyl-MSNPs-SiNPs	Vinyl functionalized MSNPs-SiNPs

Chapter 1

Introduction

1.1 Nanomaterials and Quantum Dots

In 1959, Richard Feynman gave his lecture "There is Plenty of Room at the Bottom" at the annual meeting of the American Physical Society held at the California Institute of Technology.[1] This marked the start of modern society's fascination with nanotechnology. During his presentation, Feynman posited that it would be possible to manipulate atoms and molecules to create nanoscale machines.[1] In order to create such machines, new instrumentation was needed to measure the properties of these small "nano" structures.[1,2] Instruments (e.g., mass spectrometry, vacuum technology, microscopes, etc.) with the capabilities Feynman envisioned were developed and advanced in subsequent years/decades. These new tools and techniques for material analyses spurred efforts throughout the scientific community to fabricate and interrogate "nano" structures.[2] To understand what these "nano" structures are and why they garner the attention of scientists and engineers from many disciplines, the size dependent evolution from atoms to bulk materials must be appreciated.

Figure 1.1a illustrates the size dependent evolution from atoms to bulk materials.[3] Atoms have dimensions less than 1 nm and they are shown at the left end portion on the scale. In contrast, bulk materials are at the right end portion on the scale as their sizes exceed 100 nm in all dimensions. There is a "space" between atoms and bulk materials from 1 to 100 nm that is occupied

by nanomaterials. Decreasing the size of materials from bulk to nanoscale to atoms, the electronic band structure evolves (Figure 1.1b).[4] Bulk metals exhibit continuous bands where physical and chemical properties are independent of size. In bulk semiconductors, the energy gap (E_g) separating a fully occupied valence band from the unoccupied conduction band is a fixed parameter determined by the composition and structure of the material.[4] When the size of the bulk materials is diminished to less than 100 nm (nanoscale region), nanoparticles form and the band structure characteristic of bulk materials evolves. In the nanoscale size region, significant changes in the physical and chemical properties of the particles are also observed including, high surface area, catalytic activity, tailorable thermal and electrical conductivity.[4] Due to these distinct properties, materials in nanoscale have many applications in medicine,[5] agriculture,[6] food industries,[7] biotechnology,[8] environmental pollution detection,[9] electronics,[10] and batteries.[11] Further reduction in size to the lower limit of the nanoscale region (< 10 nm) is intriguing in terms of material electronic structure.[3] In particular, discrete energy levels become dominant when the size of the particles. The electronic band structure of these small particles is similar to that of a molecule where molecular orbitals with LUMO (lowest unoccupied molecular orbital) and HOMO (highest occupied molecular orbital) states dominate.

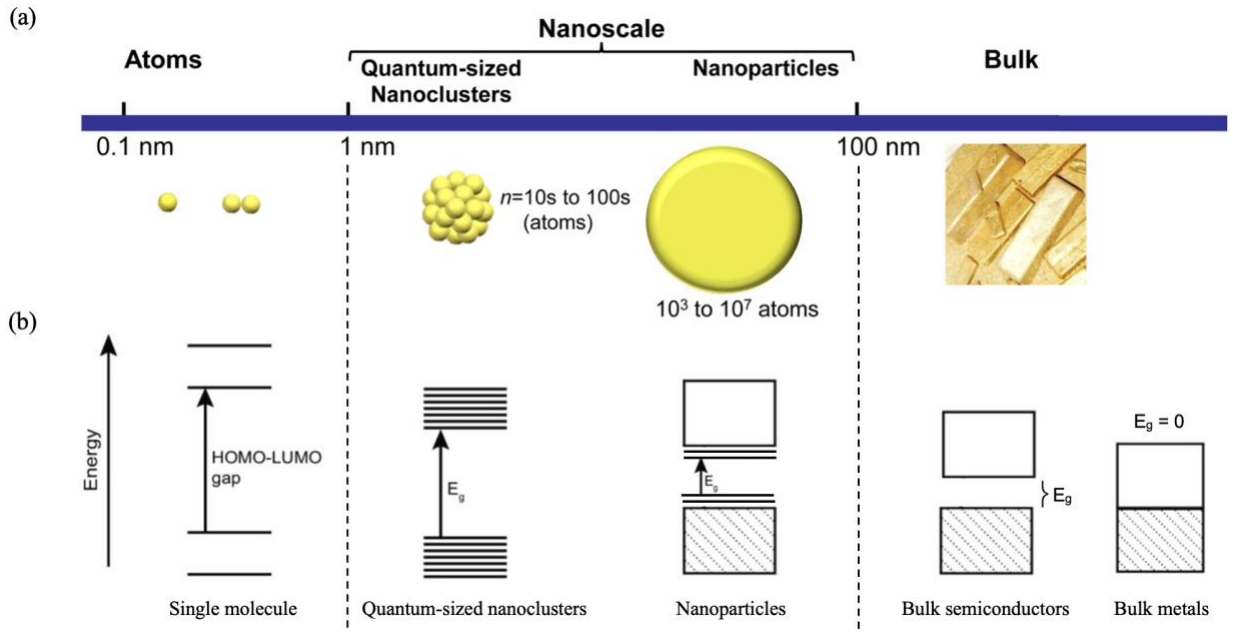

Figure 1.1. (a) The size evolution from atoms, to nanoscale, to bulk materials. The nanoscale region (1–100 nm) exhibits two distinct size regimes, quantum sized: 1–10 nm and nanoparticles: 10–100 nm. (b) Energy levels from molecules, to nanostructures, to bulk materials. Diatomic electronic states of a single molecule (where, HOMO = highest occupied molecular orbital, LUMO = lowest unoccupied molecular orbital), discreet energy levels in quantum-sized nanoclusters (where, E_g = HOMO-LUMO gap), band structure of nanoparticles, band structure of bulk semiconductors, and continuous band structure of bulk metals respectively. Adapted from reference 3.

Moreover, in sufficiently small particles (ca. 1–10 nm), the band gap is dependent on the particle size.[4] In order to understand the size dependency of the band gap, it is necessary to introduce semiconductor nanoparticles or quantum dots (QDs) that exhibit nanoscale dimensions (ca. 1 – 10 nm).[7] In bulk semiconductors, excitation of an electron from the valence band to the conduction band creates a vacancy (hole) in the valence band. Coulombic attraction between a negatively charged electron (e^-) and a positively charged hole (h^+) form electron-hole pair, called exciton.[12] Excitons have an average physical separation between the electron and hole known as Bohr radius, and this value depends on the material properties (e.g., dielectric constant). When the size of the particles is smaller than, or comparable to, the exciton Bohr radius, it results in the confinement of excitons in all dimensions.[12] This three-dimensional confinement of excitons

results in the drastic altering of the electronic structure in QDs (discrete energy levels) compared to bulk materials (continuous energy levels). This is called the quantum confinement effect (Figure 1.2).[13] The quantum confinement effect is the primary determinant in the size-dependent optical and electrical properties of nanomaterials as described by Moungi G. Bawendi, Louis E. Brus and Aleksey Yekimov who were awarded the Nobel Prize in Chemistry 2023 for the discovery and development of quantum dots.[14]

QDs exhibit bright, size-dependent photoluminescence (PL) that can be tuned by defining the material and particle size; this is complemented by their high surface-to-volume ratio and tunable surface chemistry which make them suitable for many applications such as sensing[15] and bioimaging.[16] As the definition suggests, QDs can be prepared from any semiconductor.[10] Given the vast array of possibilities, for convenience, the present discussion will be limited to QDs based upon group 14 elements.

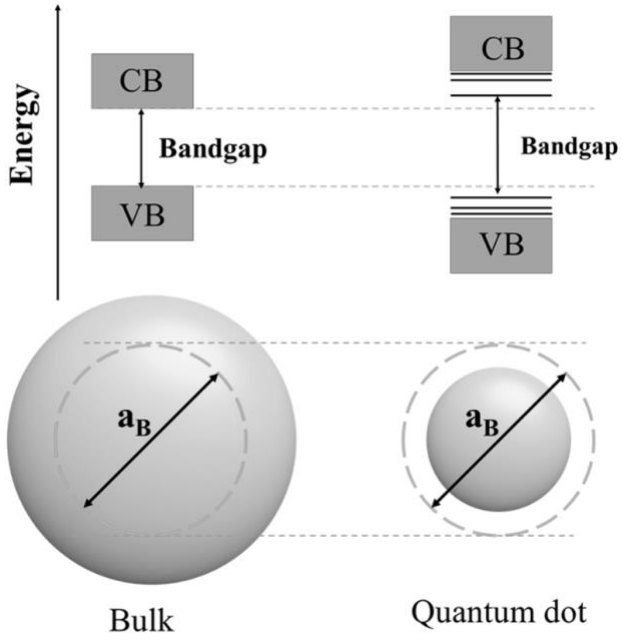

Figure 1.2. Quantum confinement effect, resulting in unique characteristics compared to the bulk form, a_B is the Bohr exciton diameter. Adapted from reference 13.

1.1.1 Group 14-Based Quantum Dots

While QDs possess may characteristics that make them attractive for a wide range of applications, their practical use, especially in biological applications, faces limitations due to their toxicity. Many QDs contain toxic heavy metals such as cadmium or lead, and the European Union has placed limits on the use of these materials in consumer devices.[17] As a result, there has been a concomitant increase in the study of non-toxic QDs, with a particular focus on Group 14 elements. Silicon, a Group 14 element, stands out as it has very high terrestrial abundance, and Si-based nanoparticles have environmentally friendly degradation routes. An intrinsic semiconductor, silicon shows distinct properties at the nanoscale such as size-dependent PL. Combining the non-toxicity and high quantum yield of silicon nanomaterials has led to promising results in biological applications such as bioimaging and biosensing.[18]

1.2 Silicon Nanoparticles

Semiconductors are classified as direct or indirect band gap depending on the alignment of the conduction band (CB) and the valence band (VB) (Figure 1.3). In a direct band gap semiconductor, the lowest point in the CB and highest point in the VB appear at the same momentum coordinate, the e^- and h^+ pair can form directly since the e^- can shift to the CB without a change in momentum (Figure 1.3a). In indirect band gap semiconductors, the lowest point in the CB and highest point in the VB appear at different momentum coordinates and the e^- cannot shift to the CB without changing momentum (Figure 1.3b).[19] This change in momentum requires a lattice vibration, a phonon. The phonon is a quantum mechanical description of thermal vibrations in the crystal lattice.[20] In an indirect semiconductor, the participation of a phonon in the photon absorption is essential for the conservation of momentum necessary for the transition of an electron

from the valence band to the conduction band which energetically corresponds to the band gap energy. [19,20] As the phonon absorption mediates electron-hole generation in the indirect band gap, conversely the phonon emission mediates radiative recombination of excitons. Therefore, both the formation and recombination of excitons occurs at a slower rate in indirect band semiconductors. This leads to decreased emission rates and lower emission efficiency as compared to direct band semiconductors.[20] However, silicon nanoparticles (SiNPs) are efficient light emitters even though they have an indirect band gap.[19,21] One explanation is based on the quantum confinement effect. Calculations have shown that confinement leads to a broadening of exciton wavefunctions that allows the VB and CB to align (Figure 1.3c).[22]

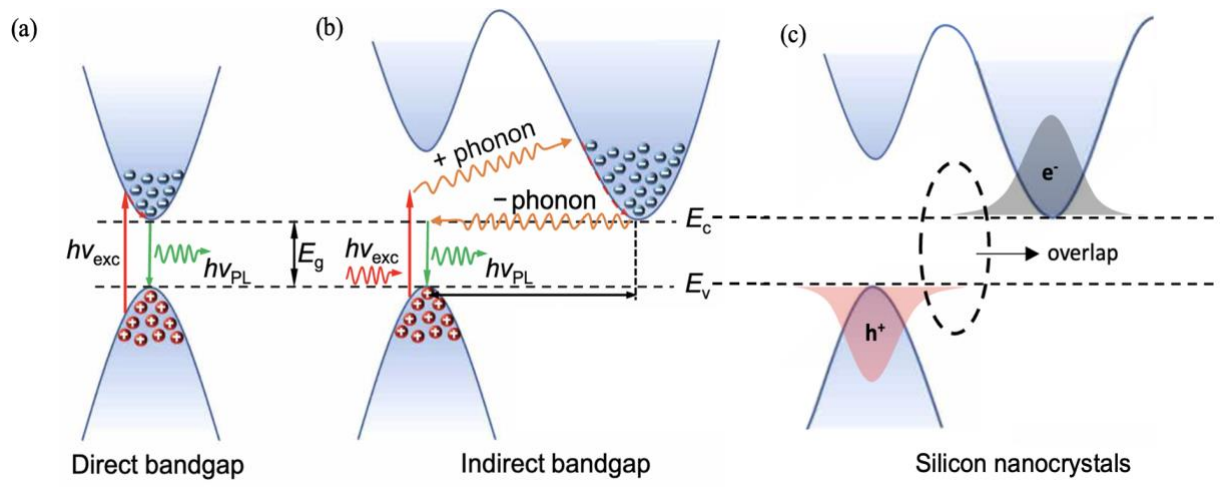

Figure 1.3. (a) Exciton formation in direct bandgap semiconductors (where, $h\nu_{exc}$ = excitation energy, $h\nu_{PL}$ = photoluminescence energy, E_g = bandgap energy). (b) Exciton formation and recombination in indirect bandgap semiconductors through phonon absorption and emission process, respectively. (c) Broadening of exciton wavefunctions in silicon nanoparticles. The x-axis represents the position of the excitons. Adapted from reference 22.

Silicon is an indirect band gap semiconductor and shows distinct optical properties (e.g., tunable PL with relatively high quantum yields) when the size is reduced to be comparable to bulk-Si exciton Bohr radius (ca. 4 nm). Applications exploiting both the PL and environmentally

friendly properties of SiNPs include bioimaging,[23] drug delivery,[24] sensing [25] and phototherapeutics[26].

1.2.1 Synthesis of Silicon Nanoparticles

There are two broad classifications of nanomaterial synthesis and that methods for the synthesis of SiNPs can be divided into - top-down and bottom-up. "Top-down" methods involve the synthesis of SiNPs from bulk silicon whereas the "bottom-up" methods involve the synthesis of SiNPs by assembling single atoms and molecules.[27] Top-down methods (e.g., electrochemical etching, mechanical grinding of bulk silicon and laser ablation) have been used to prepare free standing SiNPs. Common to all methods is some control over the structure/crystallinity, size, composition, surface chemistry of SiNPs with each method exhibiting its own advantages and challenges.[27]

Electrochemical etching of silicon wafer can be used for the synthesis of colloidal suspensions of SiNPs.[27] As a specific example, Hwang et al. prepared SiNPs by electrochemical etching of silicon in a polycarbonate cell to remove the surface oxide.[28] The silicon wafer was located between the platinum wires. Electrolyte, a HF/HNO_3/ethanol solution (v:v:v; 1:1:4), was slowly pumped into the cell at 5 mL/min. This yields to Si-H groups on the surface suitable for further functionalization. In this study, SiNPs with an average diameter of 2.7 nm were produced and showed an emission maximum at 410 nm with quantum yield of 20%. It should be noted that emission maximum for SiNPs (ca. 3 nm) is reported to be around 700 nm by the Veinot group.[29] Therefore, the emission maximum for 2.7 nm SiNPs shows a large blue-shift compared to the data reported in literature. This blue-shift is consistent with oxidation on the surface of SiNPs.[30] While

electrochemical etching method provides a straightforward synthesis of SiNPs from bulk silicon, control over the surface oxidation can be challenging.

Mechanical grinding of bulk silicon in a blender can also be used to synthesize SiNPs.[31] Five grams of silicon lumps were added to the blender and ground in 300 mL of deionized water. SiNPs were dispersed in water with an initial concentration of 16 g/L. Large particles with a significant size distribution (ca. 100-200 nm) were obtained. Although the mechanical grinding provides large-scale and low-cost fabrication of SiNPs, obtaining a narrow size distribution, along with smaller particles, is challenging.

Laser ablation, another top-down method, uses a high-power light source to break silicon wafers into fragments of SiNPs.[32] Small-sized SiNPs (ca. 3-5 nm) were produced in chloroform using pulsed laser ablation, followed by post-treatment with an isopropanol, HF, and hexane (v:v:v; 3:1:3) solution. Although laser ablation method provides a rapid synthesis route for the preparation of SiNPs, it requires high investment costs due to the high price of laser systems. Also, the control of particle size and morphology of the laser-ablated nanoparticles is quite difficult.[33]

Bottom-up methods (e.g., solution and gas-phase reactions, thermal decomposition of silicon-rich precursors) have been used to prepare SiNPs. In a bottom-up procedure, Swihart et al., produced SiNPs through the pyrolysis of silane (SiH_4) in a plasma reactor.[34] SiNPs ~13 nm in diameter were synthesized. This procedure is hampered by the heavily regulated use of SiH_4 gas which presents a significant safety hazard as it is toxic, pyrophoric, and can be unpredictable.[35]

SiNPs can also be produced by the reduction of silicon tetrachloride ($SiCl_4$) in the presence of a "capping agent".[27] Wilcoxon et al., prepared SiNPs from $SiCl_4$ at room temperature by using lithium aluminium hydride as the reducing agent in the presence of tetraoctylammonium bromide.[36] The SiNPs produced ranged in sizes from 2-10 nm and exhibited PL emission between

350-700 nm. During this reaction, SiH_4, a hazardous gas, was produced as a by-product.[37] The use of alternate solid-state precursors became favorable to in order to utilize less hazardous materials.

The Veinot group utilizes a method for synthesizing SiNPs via the high temperature processing of hydrogen silsesquioxane (HSQ) in a reducing environment (5% H_2 and 95% Ar).[29] Annealing this silicon rich oxide forms nanocrystalline silicon domains embedded within a silicon oxide matrix.[27] The sizes of the SiNPs are controlled by changing the annealing temperature and/or the time of annealing.[29] Figure 1.4. shows (a) the synthesis method and (b) bright-field transmission electron microscopy (TEM) images of SiNPs synthesized by procedure in (a).

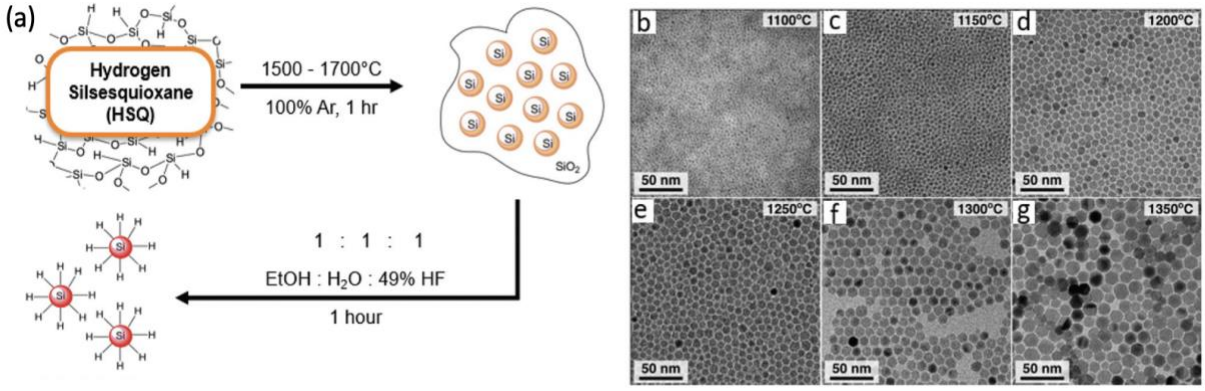

Figure 1.4. (a) Synthesis of SiNPs via thermally induced disproportionation of HSQ. (b-g) Bright-filed transmission electron microscopy (TEM) images of SiNPs. Taken from reference 29.

Selective etching of the silica (SiO_2) matrix using hydrofluoric (HF) acid liberates hydride-terminated SiNPs (H-SiNPs). Hydrosilylation is done to passivate the surface by converting Si-H bonds on the surface of the SiNPs to Si-C bonds. Hydrosilylation can be performed using a variety of alkenes via various functionalization methods such as heat, UV light, catalyst, and radical initiator (Scheme 1.1). Thermally-induced hydrosilylation using 1-dodecene is commonly used due to its simplicity and effectiveness. A typical thermally-induced hydrosilylation involves heating, under an inert atmosphere, a mixture of H-SiNPs and ligand (e.g., 1-dodecene) to

temperatures ranging from 100 to 190 °C. The ligand, for example 1-dodecene, acts as both the solvent and reactant and the high temperature triggers the homolytic breaking of the Si-H bond which then initiates the hydrosilylation reaction. Dodecane functionalized SiNPs synthesized by thermal hydrosilylation showed PL with emission peak maximum changing from 650 – 950 nm depending on the size of NC.[29]

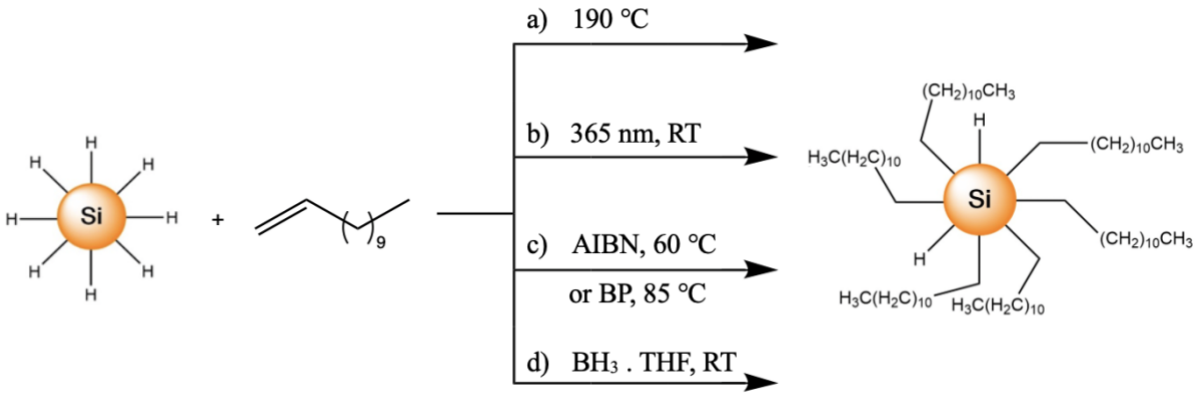

Scheme 1.1. Formation of dodecyl-functionalized Si-NCs by (a) thermally-, (b) photo-, (c) radical-initiated, and (d) Lewis acid catalyzed reactions. Taken from reference 29.

1.2.2 Applications of Silicon Nanoparticles

SiNPs have been investigated in a variety of applications. Not surprisingly, applications of SiNPs center on the PL properties of these species.[38] Organic light-emitting diodes (OLEDs) consist of a thin semiconductor layer that emits light under an applied voltage.[39] Cheng et al. fabricated an OLED using SiNPs functionalized with 1-dodecene (PL maximum at 800 nm). They observed a device power efficiency of 8.6%, the highest value reported to date for an OLED prepared using semiconductor nanoparticles.[40] Cho et al. prepared a thin films consisting of silicon quantum dots (SiQDs) for electrically stimulated light emission and observed emission ranging from infrared to blue.[41] These reports are both in keeping with the potential for incorporating SiNPs into light-emitting devices.

While utilizing PL emission is favourable for light-emitting device applications, the quenching the PL emission of SiNPs can be used in sensing applications. Gonzalez et al demonstrated the use of dodecyl functionalized SiNPs as sensors via the quenching of PL emission when these SiNPs were exposed to nitroaromatic compounds.[42] The quenching occurred via electron transfer from the CB of SiNPs to the π^* orbital of the nitroaromatic compounds. In another sensing application, Robidillo et al. produced a sensor based on the interaction of SiNPs with p-nitrophenyl-containing organophosphate nerve agents.[43] In addition, Robidillo et al. also prepared SiNPs containing covalently bound urease at the surface of the particle. The ammonia formed upon exposure to urea the quenched the PL, allowing for the detection of urea.[44]

Due to their non-toxicity, SiNPs have attracted interest for use in biological systems.[45] For example, Sailor et al. demonstrated that in biological systems porous silicon degrades to silicic acid that is then cleared from the body.[46] Fujioka et al. concluded that SiQDs are less toxic than metal containing QDs such as cadmium selenide (CdSe) QDs due to the release of heavy-metal ions upon exposure to UV light.[47] Further studies on the in vivo use of CdSe quantum dots showed intestinal cell death due to free Cd^{2+} ions present.[48] Cheng et al. found that SiQDs, with the high quantum yields (60–70%), in phospholipid micelles provided higher resistance against photobleaching compared to organic dyes.[49] Sailor et al. demonstrated the use of SiNPs in therapeutic applications by functionalizing SiNPs with a chemotherapeutic agent, doxorubicin, and using the system in a drug delivery application.[46] Porous materials provide large pore volumes that allow adsorption and desorption of therapeutic agents at controlled rates, leading to an improved therapeutic efficiency. For this reason, preparing a hybrid material by coating SiNPs with a material such as porous silica could improve the efficiency of drug delivery to biological systems.

The properties and use of porous silica in the preparation of this class of hybrid material will be discussed in detail in Section 1.4.

1.3 Silver Nanoparticles

Silver nanoparticles (AgNPs) are used in many fields (e.g., biosensing, environmental remediation, wound healing, pharmaceuticals, disinfectants, packaging, detergents, plastics) due to their anti-bacterial applications along with unique physical and chemical properties such as high specific surface area, high thermal and electrical conductivity, improved surface Raman scattering, and catalytic activity.[50]

1.3.1 Synthesis of Silver Nanoparticles

The syntheses of AgNPs are categorized, as with many nanoparticles, as either top-down or bottom-up. In the top-down approach, a bulk material is reduced in size into fine particles with a variety of techniques such as evaporation-condensation, laser ablation, and ball milling.[51] In the bottom-up approach, nanoparticles are synthesized by the assembly of atoms into nuclei that grow into nanoparticles.[52] Each general method has distinct advantages and challenges.

Evaporation-condensation can be used for the synthesis of AgNPs starting from bulk silver.[53] In a specific example, Scheibel et al. prepared AgNPs by evaporating bulk silver placed in a ceramic crucible and heated to temperatures between 1300-1400 ^{o}C in a tube furnace under a flow of nitrogen gas.[54] The metal vapor was carried out of the furnace and diluted with nitrogen gas. As the metal vapor exited the furnace, there was a sudden decrease in the temperature. Due to this temperature drop, the silver vapor condensed and subsequently formed the nanoparticles. In this study, AgNPs with an average diameter between 2-100 nm were produced. Although the

synthesis of the AgNPs is relatively straightforward and low-cost, a significant drawback is the very wide size distribution in the size of the particles.

Moreover, AgNPs can be synthesized by the laser ablation of metallic bulk materials in solution.[55] Using two lasers, a Nd:YAG (neodymium-doped yttrium aluminum garnet; Nd:$Y_3Al_5O_{12}$) pulsed laser (1064 nm, pulse length 10 ns) and a continuous wave diode pumped solid state laser (530 nm) AgNPs were synthesized starting from a high purity silver target (8 mm × 8 mm × 1.5 mm) in de-ionized water. AgNPs with an average diameter of 45 nm were produced. Although colloidal nanoparticles can be prepared by this laser ablation method without the use capping agents in the solution,[53] laser systems have high power consumption with high investment costs.[56]

Ball milling, another top-down method, can be used to synthesize AgNPs. In a typical procedure, milling balls and metal materials are placed in a container that rotates at a high speed in the presence of air or inert gas. In one report, AgNPs were synthesized by the mechano-chemical reduction of Ag_2O using graphite in a high energy ball mill under air.[57] AgNPs with an average diameter of 28 nm were produced after 22 h milling time. While ball milling provides a straightforward synthesis of AgNPs, it can be hampered by high processing times and limited size tunability.

Bottom-up methods (e.g., biosynthesis, chemical reduction) have been used to prepare AgNPs. In a biosynthetic bottom-up procedure, AgNPs with an average diameter between 7-23 nm were produced by incubating $AgNO_3$ with a fungus (A. terreus) for 48 h at 25 ^oC under dark conditions.[58] The biosynthesized AgNPs showed anti-microbial activity against various pathogens. Importantly, biosynthetic methods utilize sustainable and environmentally friendly reducing agents (e.g., polysaccharides, proteins) from microorganisms. However, microbe cultures require

sterile apparatus, glassware, and workspace as they are vulnerable to contamination. Also, it is challenging to control the characteristics of biosynthesised AgNPs because most of the microbes are sensitive to pH and temperature.[59]

Chemical reduction can also be used to prepare AgNPs. In a typical synthesis, a metal precursor (e.g., $AgNO_3$), reducing agent (e.g., $NaBH_4$, N_2H_4, sodium citrate), and stabilizing agents (e.g., polyvinyl pyrrolidone (PVP), polyvinyl alcohol (PVA), polyethylene glycol (PEG), chitosan, oleylamine, and glycerol) are combined.[60] The LaMer model gives insight into the process of the nanoparticle formation based on the atom-mediated nucleation and growth theory. This theory suggests the use of atoms as the building blocks for the nucleation and growth of the nanoparticles.[61] The nucleation and growth processes can be described by the LaMer curve. In order, this curve is divided into three regions: production of atoms, nucleation from the aggregation of atoms, and nanoparticle growth from the addition of atoms (Figure 1.5).[62] In region I, metal ions (e.g., Ag^+) are reduced to metal atoms. These metal atoms aggregate to form small clusters once the atomic concentration exceeds the supersaturation (C_{min}) point. In region II, this nucleation results in a decrease in the concentration of free atoms. Once the concentration of the metal atoms drops below C_{min}, nucleation slows, then stops. Several theories on the mechanism of the nucleation process have been proposed. Burst nucleation is the widely accepted mechanism for the nuclei formation.[62] Burst nucleation can be defined as a sudden increase in atomic concentration, followed by a rapid decrease below nucleation levels that prevents further nucleation. Finally, in region III, nuclei grow as metal atoms are deposited on their surfaces. The growing nuclei increase in size to a critical radius that corresponds to the minimum size required for the particle to form without being re-dissolved. These particles are "seeds" for nanoparticle formation. The seeds grow and evolve into the nanoparticles.[62,63] Also, several theories have been proposed for the

nanoparticle growth process. The most studied process is Ostwald ripening where the small nuclei (smaller than the critical size) dissolve and deposit on the large nuclei leading to coalescence.[64]

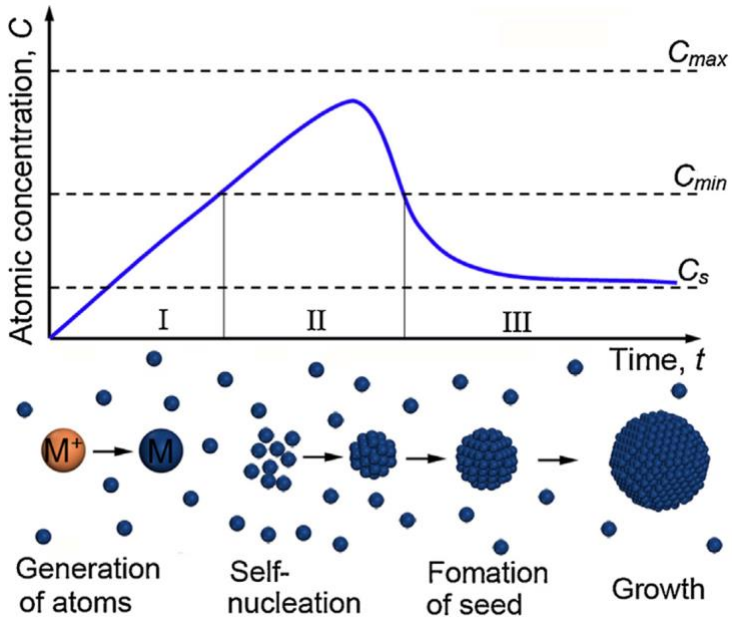

Figure 1.5. LaMer curve that describes the nucleation and growth processes (where, C_{max} = critical limiting supersaturation point, C_{min} = supersaturation point, and C_s = saturation concentration). Adapted from reference 61.

1.3.2 Properties and Applications of Silver Nanoparticles

There has been a significant interest in the use of silver nanoparticles (AgNPs) as they exhibit notable characteristics that include high electrical and heat conductivity, antibacterial and photocatalytic activity. [65] The optical properties of AgNPs are of particular interest. When AgNPs interact with an appropriate incident light, a collective oscillation of surface electrons, called plasmons, is observed. The oscillation of electrons on the metal nanoparticle surface due to the interaction with incident photons is known as surface plasmon resonance (SPR) (Figure 1.6a) and leads to the presence of an electromagnetic field localized on the AgNPs. This localized electromagnetic field results in significantly increased absorption and scattering intensities of AgNPs compared to non-plasmonic nanoparticles of the similar dimensions (Figure 1.6b).[66,67] The

SPR established in nanostructures is called localized surface plasmon resonance (LSPR); the frequency at which the resonance occurs is directly related to the energy of the surface plasmons.

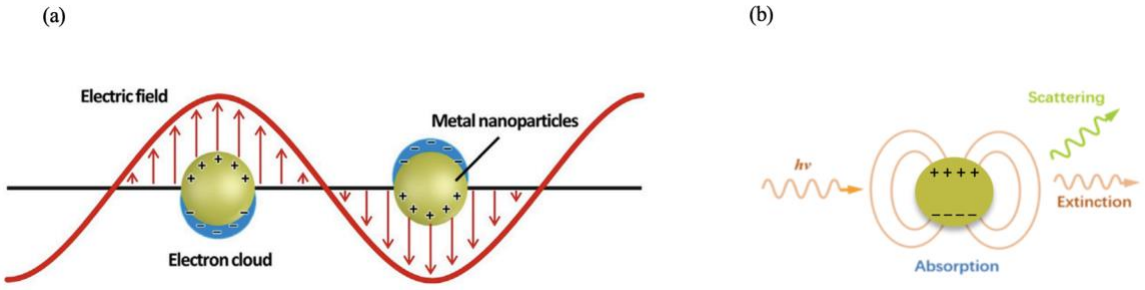

Figure 1.6. Oscillation of the electron cloud of a metal nanoparticle. Adapted from reference 61 and 66.

SPR depends on the composition, shape, size, and surface coating of the particles, and plasmonic nanomaterials are often used for sensing applications.[68] As a specific example, a portable device that uses a colorimetric method for the selective detection of lead (Pb) in water was designed.[69] AgNPs were embedded into cellulose paper strips and the concentration of Pb was determined by measuring changes in LSPR. The AgNPs showed a characteristic LSPR peak maximum at 400 nm; when Pb^{2+} was added (1–900 nM), the intensity of the Ag LSPR peak at 400 nm decreased, and a new peak emerged at wavelengths more than 600 nm with the increasing concentration of Pb^{2+} ions. The Ag LSPR peak decreases when the individual nanoparticles aggregate; instead, a new SPR peak emerges related to the aggregated NPs.

Collective electron oscillations in the nanoscale region generate large field enhancements within and near nanoparticles. The distribution of the electromagnetic field depends strongly on the size and shape of the nanoparticles used. For plasmonic nanoparticles, the strongest electromagnetic fields are located at sharp tips and edges. Such locations are known as “hot spots”. This large enhancement of the electric field around the surface of a nanoparticle can be used for sensing applications based on surface-enhanced Raman scattering (SERS).[66,70] In work reported

by Chen et al., an Ag/nanocellulose fiber SERS substrate was developed for in-situ food safety detection.[71] The nanocellulose fibers provided a flexible and a large surface area template for the nanoparticle growth. AgNPs were synthesized from $AgNO_3$ in situ, therefore, nanocellulose fiber is not only the solid support to AgNPs but also a stabilizing agent in the reaction. The prepared SERS substrate amplified the Raman signals of the target molecules and ppb-level detection of pesticides and veterinary drugs was achieved.

As discussed, the distinct optical properties of AgNPs allow for use in areas such as medicine,[72] food,[60] healthcare,[73] as well as in many consumer products such as cosmetics[74], soaps,[75] and plastic coatings.[76] AgNPs are used in the production of optical, electrical, and thermal devices and are also found in biosensors, imaging agents, and drug delivery agents due to their plasmonic properties.[66] There are several studies using AgNPs as biosensors, however, in these studies, free-standing AgNPs are not used. There are many studied describing the toxicity of AgNPs in biological applications in literature.[77,78,79] Thus, freestanding (or bare) AgNPs show toxicity in cell-based in vitro systems are not suitable for most biological applications.[77] Another reason for not using bare AgNPs in biological applications is due to their poor stability in biological systems.[80] AgNPs undergo aggregation in biological systems, resulting in complete loss of their biological activity. To overcome these challenges, AgNPs can be coated with various compounds to both mitigate toxicity and increase stability.[79] Porous materials (e.g., mesoporous silica, Section 1.4) have found use in biological applications such as drug delivery and biosensing due to their large surface area, controlled pores, and non-toxicity.[81] Therefore, combining the district optical properties of AgNPs with the nontoxicity and large surface area of mesoporous silica can provide a multifunctional hybrid material tailored for biological applications.

1.4 Mesoporous Silica

Mesoporous silica was first discovered by Beck et al. in 1992 as high surface area silica with pore sizes ranging from 2 to 50 nm. The synthesis was via the calcination of aluminosilicate gels in the presence of quaternary ammonium surfactants; the formation of the pores and optimization of pore size requires the use of a surfactant.[82] It was postulated that the synthesis occurred through a liquid-crystal templating (LCT) process as shown in Figure 1.7.[83,82]

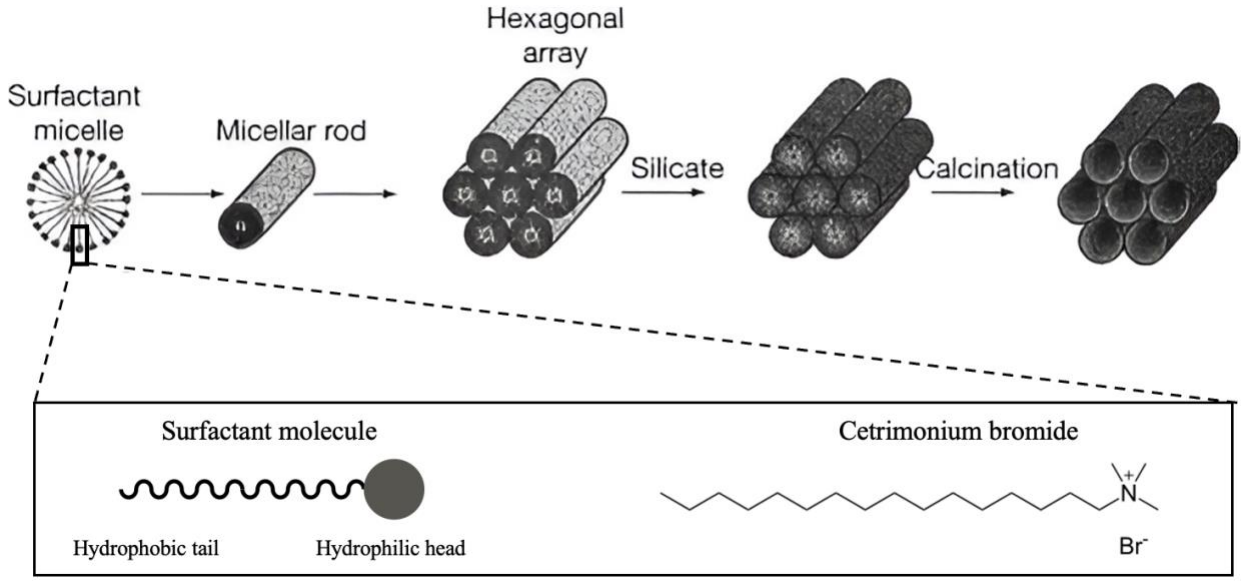

Figure 1.7. The suggested mechanism for the formation of mesoporous silica by LCT process. The structure of a surfactant molecule, and the example surfactant molecule (cetrimonium bromide). Adapted from reference 82.

As illustrated in Figure 1.7, the LCT process involves the formation of the self-assembly of surfactant molecules to form surfactant micelles, the assembly of surfactant micelles into the cylindrical micellar rods, the formation of hexagonal liquid crystal structures which act as a template, the adsorption of anionic silicates (e.g., $Si(OC_2H_5)_4$) on the positively charged surfactant micelles, and the removal of the internally bonded surfactant by calcination or solvent extraction to yield mesoporous silica, respectively.[82] The length of the carbon chain in the surfactant molecule

determines the size of the micelles, which then subsequently determine the diameters of the pores in the mesoporous silica.[84] In the LCT process, the formation of silicates is based on hydrolysis and condensation reactions, commonly known as sol-gel, and leads to a network of silicates surrounding the template.[85] Hydrolysis and condensation reactions occur with the use of a precursor (e.g., tetraethyl orthosilicate), creating a highly linked network composed of silica. The reaction scheme for hydrolysis and condensation reactions is given in Scheme 1.2. [85,86]

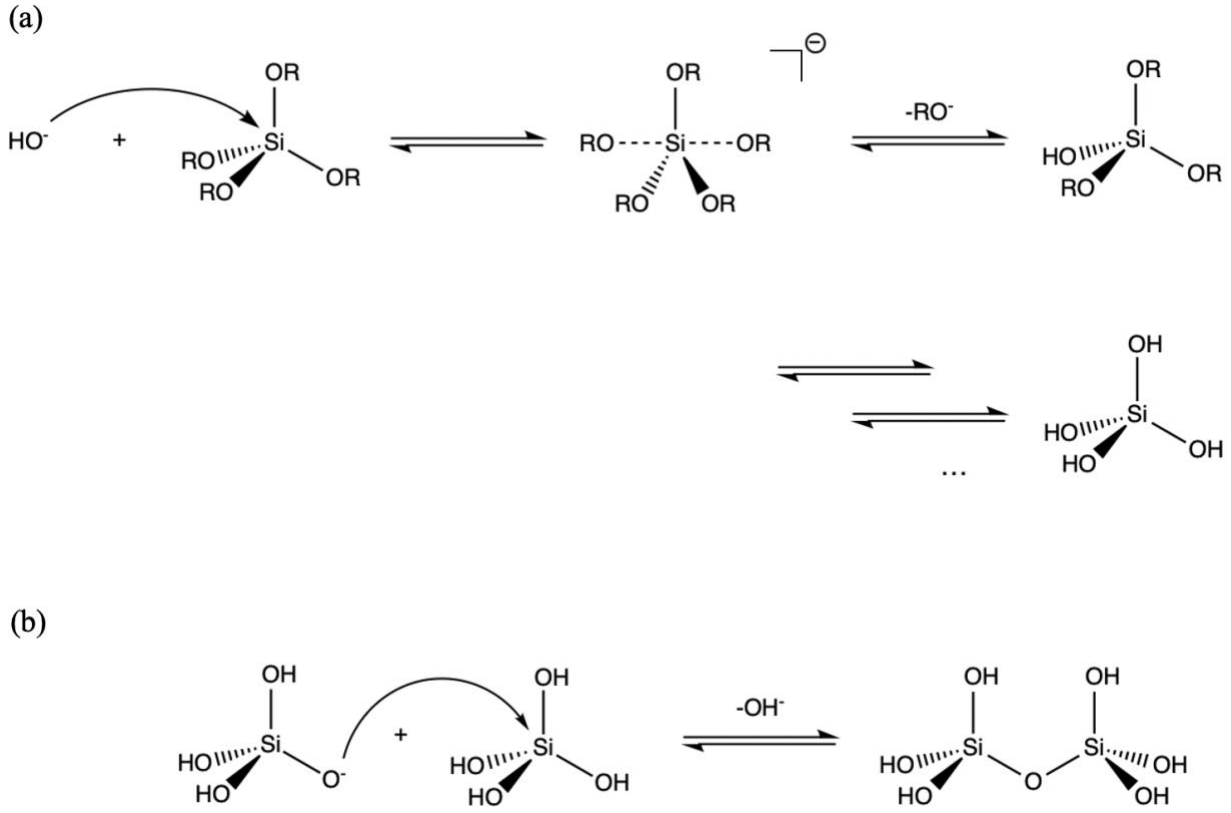

Scheme 1.2. Sol-gel reaction (where R=Et for tetraethyl orthosilicate); (a) hydrolysis, (b) condensation.

Surfactant removal is usually carried out either by calcination or extraction. Calcination promotes the condensation of unreacted silanol groups on the surface. Typical calcination temperatures are between 400–5500 ^{o}C. Extraction processes (e.g., extraction in acid/alcohol mixtures) can also be used for surfactant removal and they minimize the loss of surface silanols.

In general, sol-gel reactions are comparatively straightforward and cost-effective, making them useful for producing mesoporous silica nanoparticles (MSNPs) with defined structural and surface characteristics.[87]

1.4.1 Applications of Mesoporous Silica

Due to their stability, high pore volumes, and polar cage structure, the first investigations into the uses of mesoporous silica focused on applications related to adsorption and catalysis. Selected systems showed improvement in catalytic activity[88] and/or adsorbent capacity.[89] In 2001, the first application of mesoporous silica in drug delivery was reported. Specifically, MSNPs were used due to their large surface area, controlled pores, non-toxicity, and suitability for surface chemistry.[90] Subsequently, MSNPs have been used for drug delivery, controlled drug release, imaging and biosensing.[91] Although MSNPs have many advantages in biological applications, they lack optical properties. This limits the functionality of these materials in terms of in-situ response.[92]

A literature report described the encapsulation of cadmium selenide quantum dots (CdSe QDs) by the mesoporous silica to form water soluble luminescent QDs for biological imaging and drug delivery.[93] The toxicity of CdSe QDs in biological systems is a major concern. Mesoporous silica is used to encapsulate the QDs to reduce their toxicity by preventing any leakage of the core materials. However, it is not known if the mesoporous silica encapsulated CdSe QDs would stay intact inside biological systems or if the QDs could be degraded by certain mechanisms in vivo.[94]

Encapsulating gold nanoparticles (AuNPs) in mesoporous silica led to a hybrid material for drug delivery and plasmonic detection of the molecules of interest in biological systems.[95] Despite the low toxicity of AuNPs in biological systems, it was found that AuNPs can accumulate

in organs like liver, lung, and spleen.[96] Apart from this, it is important to take into account the non-biodegradability of AuNPs which can have an effect on the biocompatibility.[96]

Additionally, mesoporous silica coated gadolinium oxide nanoparticles (GdONPs) were synthesized and then studied as a potential MRI imaging agent.[97] Although GdONPs have high biocompatibility, their clinical usage has been hindered as a result of high cost.[97]

These reports illustrate a general theme regarding the formation of hybrid materials synthesized by combining mesoporous silica with selected nanoparticles. The resulting hybrid materials possess district properties and provide unique systems for drug-delivery, bioimaging, and biosensing. However, the previously mentioned systems rely on toxic and/or high-cost materials. SiNPs have size dependent luminescent properties and nontoxicity that makes them suitable for biological applications.[98] These materials are also well-known in our laboratories. AgNPs provide improved surface Raman scattering which is useful for sensing applications. Thus, preparing hybrid materials combining MSNPs and nanoparticles with distinct properties could merge the non-toxic and luminescent properties of SiNPs, plasmonic properties of AgNPs and the large surface area and adsorbent properties of MSNPs to create multifunctional materials tailored for biological applications.

A chemical sensor is defined as a device that transforms chemical information (e.g., the concentration of a molecule of interest) into a useful signal.[99] Sensing devices have been used in many fields such as medical diagnosis, food analysis and toxin detection in environmental analysis. A sensor must have high selectivity towards the molecule of interest as well as high sensitivity. In addition, for practical applications the sensor should be low cost. In biological systems, antibody sensors are based upon the response of an immobilized antibody to an antigen (analyte). Synthetic receptors have shown similarity to the natural antibody–antigen response; this provides additional

avenues and materials for sensor design.[100] One drawback of using hybrid materials of MSNPs with nanoparticles in sensing applications is the non-selective nature of the system. Controlling selectivity towards molecules of interest is a challenge because the pores of mesoporous silica do not discriminate between the molecules of interest and other molecules in the sensing medium. For this reason, molecular imprinting is essential to produce sensors with the needed selectivity.

1.5 Molecularly Imprinted Polymers

Research into molecular imprinted polymers (MIPs) has been active since the late 1990s. Importantly, MIPs exhibit properties close to those of natural receptors in terms of selectivity and can be modified for a wide range of target molecules.[99] MIPs offer an advantage in terms of operating temperature compared to natural receptors; natural receptors typically require body temperature whereas MIPs can be used at different temperatures depending on the polymer used. This has driven research into MIPs for applications into various fields such as sensing and bioimaging.[100]

1.5.1 Synthesis of Molecularly Imprinted Polymers

A standard synthesis of MIPs utilizes the polymerization of functional and cross-linking monomers around the template (Figure 1.8). The template can be an atom, ion, molecule, complex or a molecular, ionic, or macromolecular assembly, including micro-organisms. The template in Figure 1.8 is represented as a bulky structure referring to a macromolecular assembly. In our research, molecular templates are used. The synthesis begins with the interaction of functional monomers with the template molecules via covalent or noncovalent interactions to form a polymeric network. Covalent interactions are formed via reactive groups; non-covalent

interactions are often based on hydrogen-bonding. Acrylamide (AAm), methyl methacrylate (MMA) and methacrylic acid (MAA) are some of the most commonly used monomers. A cross-linking agent (e.g., ethylene glycol dimethacrylate, EGDMA) and an initiator (e.g., azobisisobutyronitrile, AIBN) are then added. The polymerization can be initiated by heat or ultraviolet radiation. Several methods (e.g., soxhlet extraction, solvent extraction, physically assisted solvent extraction, chemical cleavage-based extractions, solid-phase imprinting) can be used for template removal. The driving force for the removal of template molecules from the MIPs is the selective solubility of template molecules in the solvent. Also, exposure to solvents induces swelling in the polymer networks and encourages the chemical cleavage of the template molecules from the polymer matrix.[99,100] The cavities, formed after the template extraction, are selective for the template molecules in terms of size and chemical functionality. Thus, template molecules can rebind to these specific sites.[101]

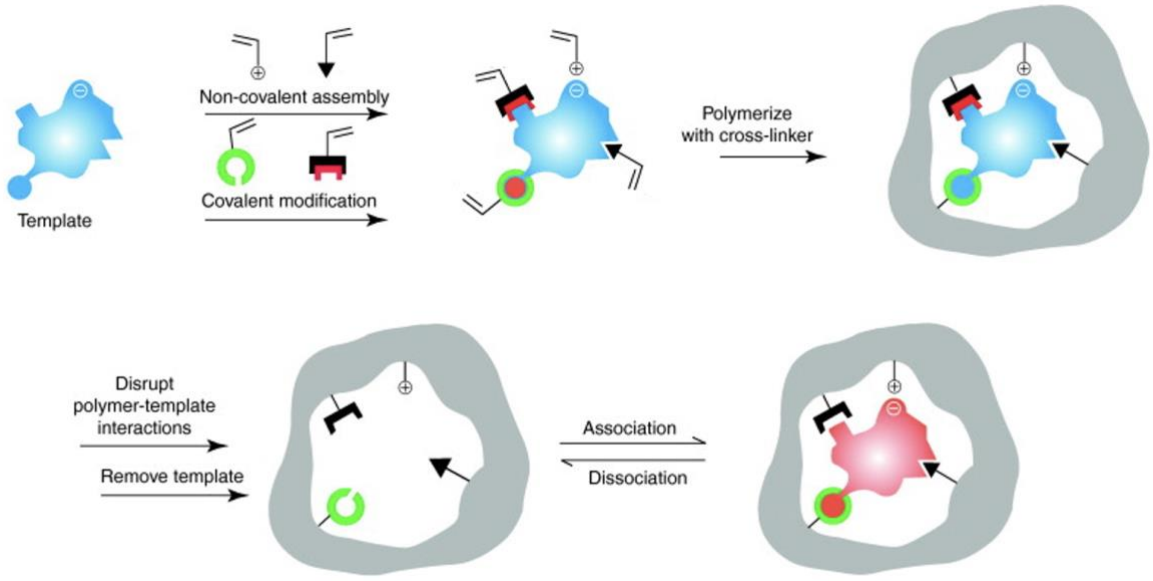

Figure 1.8. Representation of the production of MIPs. Adapted from reference 99.

While MIPs provide a selective platform to bind molecules of interest, they need to be paired with a response system as the detection of the target molecules depends on the change in the response system. These response systems can be electrochemical, gravimetric, or optical.[99]

Each individual material (SiNPs, AgNPs, MSNPs, and MIPs) has distinct advantages, and, in combination, could lead to improved biological sensing devices. The SiNPs are non-toxic and offer a tunable PL emission. AgNPs have plasmonic properties and provide improved Raman scattering. Thus, these materials can act as the response system. MSNPs are non-toxic and provide a large surface area with tunable pore size. The MIPs have high and tunable selectivity for target molecules. In this regard, the preparation of SiNPs encapsulated in the surface imprinted mesoporous silica and AgNPs encapsulated in the surface imprinted mesoporous silica were investigated. Once in hand, possible applications of these multifunctional hybrid materials were studied.

1.6 Thesis Scope

The preceding discussion introduced the concepts of 1) nanoparticles: SiNPs and AgNPs, 2) mesoporous silica, and 3) MIPs. The properties and applications of nanoparticles, mesoporous silica, and molecularly imprinted polymers have been reviewed. This thesis focuses on work related to incorporating the complementary advantages of each material by combining the multifunctional hybrid materials containing nanoparticles with surface imprinted mesoporous silica. Possible applications of these multifunctional hybrid materials are then studied.

In Chapter 2, we aim to prepare SiNPs embedded in surface imprinted mesoporous silica. SiNPs were prepared by high temperature processing of hydrogen silsesquioxane (HSQ), and the surface of the SiNPs were passivated with dodecyl groups. Encapsulation of SiNPs in mesoporous

silica (MSNPs-SiNPs) was performed via a sol-gel reaction. Surface modification of MSNPs-SiNPs was achieved by introducing vinyl groups followed by radical initiated polymerization. The polymer (ethylene glycol dimethacrylate) was molecularly imprinted using ibuprofen (IBU) as a template molecule. Throughout this investigation, we assessed the surface chemistry of the MSNPs-SiNPs via Fourier-transform infrared (FTIR). The successful preparation of the imprinted polymer on the surface of the particles was assessed by scanning electron microscopy (SEM). With this hybrid material in hand, we turned our attention toward determining the template loading/release efficiency of the material.

Chapter 3 describes the preparation of AgNPs embedded in surface imprinted mesoporous silica. The AgNPs were prepared using a chemical reduction method and subsequent encapsulation of AgNPs in mesoporous silica was performed via a sol-gel reaction. The surface modification of the AgNPs embedded mesoporous silica was achieved by the introduction of vinyl groups followed by radical initiated polymerization on the surface of the MSNPs-AgNPs. The polymer (poly(N-isopropyl acrylamide)-co-poly(acrylamide)) was molecularly imprinted using urea as a template molecule. Following the methodology in Chapter 2, the surface chemistry of the MSNPs-AgNPs was investigated using Fourier-transform infrared (FTIR), thermogravimetric analysis (TGA), and dynamic light scattering (DLS). The successful preparation of the imprinted polymer on the surface of the particles was evaluated by TGA and scanning electron microscopy (SEM). Similar to Chapter 2, we turned our attention toward determining the template loading/release efficiency of this hybrid material.

Finally, Chapter 4 summarizes the findings from the previous chapters and further explores relevant future research directions.

1.7 References

(1) Eberhard, W. G.; Wcislo, W. T. Plenty of Room at the Bottom? *Am. Sci.* **2012**, *100* (3), 226–233.

(2) Madkour, L. H. *Advanced Structured Materials, Nanoelectronic Materials Fundamentals and Applications*, **2019**.

(3) Jin, R.; Higaki, T. Open Questions on the Transition between Nanoscale and Bulk Properties of Metals. *Commun. Chem.* **2021**, *4* (1), 6–9.

(4) Riehle, F. S. The Rational Synthesis of Defect-Free CdE (E = S , Se) Nanocrystals From Precursor Reactivity to Surface Stability. **2013**.

(5) Tibbals, H. F. *Medical Nanotechnology and Nanomedicine, Perspectives in Nanotechnology Series*; **2011**.

(6) Mekuye, B.; Abera, B. Nanomaterials: An Overview of Synthesis, Classification, Characterization, and Applications. *Nano Sel.* **2023**, *4* (8), 486–501.

(7) Zhang, L.; Yang, X.; Yin, Z.; Sun, L. A Review on Carbon Quantum Dots: Synthesis, Photoluminescence Mechanisms and Applications. *Luminescence* **2022**, *37* (10), 1612–1638.

(8) Wang, E. C. W. and A. Z. Targeted Nanoparticles and Their Applications in Biology. *Library (Lond)*. **2014**, *6* (1), 576, 6(1), 9–26.

(9) Stander, L.; Theodore, L. Environmental Implications of Nanotechnology-an Update. *Int. J. Environ. Res. Public Health* **2011**, *8* (2), 470–479.

(10) García de Arquer, F. P.; Talapin, D. V.; Klimov, V. I.; Arakawa, Y.; Bayer, M.; Sargent, E. H. Semiconductor Quantum Dots: Technological Progress and Future Challenges. *Science* **2021**, *373*, 640.

(11) Verma, S.; Arya, S. *Applications of Quantum Dots in Batteries*; Elsevier Inc., **2021**, 287-318

(12) Beard, M. C. Multiple Exciton Generation in Semiconductor Quantum Dots. *J. Phys. Chem. Lett.* **2011**, *2* (11), 1282–1288.

(13) Xiang, X.: Wang, L.; Zhang, J.; Cheng, B.; Yu. J.; Macyk, W. Cadmium Chalcogenide (CdS, CdSe, CdTe) Quantum Dots for Solar-to-Fuel Conversion. *Adv. Photonics Res.* **2022**, *3* (11).

(14) Yu, K.; Schanze, K. S. Commemorating The Nobel Prize in Chemistry 2023 for the Discovery and Synthesis of Quantum Dots. *ACS Cent. Sci.* **2023**, *9* (11), 1989–1992.

(15) Kargozar, S.; Hoseini, S. J.; Milan, P. B.; Hooshmand, S.; Kim, H. W.; Mozafari, M. Quantum Dots: A Review from Concept to Clinic. *Biotechnol. J.* **2020**, *15* (12), 1–18.

(16) Galstyan, V. Quantum Dots: Perspectives in next-Generation Chemical Gas Sensors – A Review. *Anal. Chim. Acta* **2021**, *1152*, 238192.

(17) McVey, B. F. P.; Prabakar, S.; Gooding, J. J.; Tilley, R. D. Solution Synthesis, Surface Passivation, Optical Properties, Biomedical Applications, and Cytotoxicity of Silicon and Germanium Nanocrystals. *Chempluschem* **2017**, *82* (1), 60–73.

(18) Chang, H.; Sun, S. Q. Silicon Nanoparticles: Preparation, Properties, and Applications. *Chinese Phys. B* **2014**, *23* (8), 088102, 1-14.

(19) Delerue, C.; Allan, G.; Lannoo, M. Theoretical Aspects of the Luminescence of Porous Silicon. *Phys. Rev. B* **1993**, *48* (15), 11024–11036.

(20) De Mello Donegá, C. *Nanoparticles: Workhorses of Nanoscience*; 2014; Vol. 9783662448.

(21) Kůsová, K.; Hapala, P.; Valenta, J.; Jelínek, P.; Cibulka, O.; Ondič, L.; Pelant, I. Direct Bandgap Silicon: Tensile-Strained Silicon Nanocrystals. *Adv. Mater. Interfaces* **2014**, *1* (2), 1–9.

(22) Chen, Y.; Tan, C.; Wang, Z.; Miao, J.; Ge, X.; Zhao, T.; Liao, K.; Ge, H.; Wang, Y.; Wang, F.; Zhou, Y.; Wang, P.; Zhou, X.; Shan, C.; Peng, H.; Hu, W. Momentum-Matching and Band-Alignment van Der Waals Heterostructures for High-Efficiency Infrared Photodetection. *Sci. Adv.* **2022**, *8* (30), 092004, 1-9.

(23) Liang, J.; Huang, C.; Gong, X. Silicon Nanocrystals and Their Composites: Syntheses, Fluorescence Mechanisms, and Biological Applications. *ACS Sustain. Chem. Eng.* **2019**, *7* (22), 18213–18227.

(24) Robidillo, C. J. T.; Veinot, J. G. C. Functional Bio-Inorganic Hybrids from Silicon Quantum Dots and Biological Molecules. *ACS Appl. Mater. Interfaces* **2020**, *12* (47), 52251–52270.

(25) Chinnathambi, S.; Chen, S.; Ganesan, S.; Hanagata, N. Silicon Quantum Dots for Biological Applications. *Adv. Healthc. Mater.* **2014**, *3* (1), 10–29.

(26) Zhang, Y.; Cai, N.; Chan, V. Recent Advances in Silicon Quantum Dot-Based Fluorescent Biosensors. *Biosensors* **2023**, *13* (3), 1–16.

(27) Milliken, S.; Thiessen, A. N.; Cheong, I. T.; O'Connor, K. M.; Li, Z.; Hooper, R. W.;

Robidillo, C. J. T.; Veinot, J. G. C. “turning the Dials”: Controlling Synthesis, Structure, Composition, and Surface Chemistry to Tailor Silicon Nanoparticle Properties. *Nanoscale* **2021**, *13* (39), 16379–16404.

(28) Hwang, J.; Jeong, Y.; Lee, K. H.; Seo, Y.; Kim, J.; Hong, J. W.; Kamaloo, E.; Camesano, T. A.; Choi, J. Simple Preparation of Fluorescent Silicon Nanoparticles from Used Si Wafers. *Ind. Eng. Chem. Res.* **2015**, *54* (22), 5982–5989.

(29) Clark, R. J.; Aghajamali, M.; Gonzalez, C. M.; Hadidi, L.; Islam, M. A.; Javadi, M.; Mobarok, M. H.; Purkait, T. K.; Robidillo, C. J. T.; Sinelnikov, R.; Thiessen, A. N.; Washington, J.; Yu, H.; Veinot, J. G. C. From Hydrogen Silsesquioxane to Functionalized Silicon Nanocrystals. *Chem. Mater.* **2017**, *29* (1), 80–89.

(30) Yamauchi, Y.; Sakurai, T.; Hirohata, Y.; Hino, T.; Nishikawa, M. Blue Shift of Photoluminescence Spectrum of Porous Silicon by Helium Ion Irradiation. *Vacuum* **2002**, *66* (3–4), 415–418.

(31) Kim, T.; Lee, J. Silicon Nanoparticles: Fabrication, Characterization, Application and Perspectives. *Micro Nano Syst. Lett.* **2023**, *11* (1), 1-9.

(32) Švrček, V.; Sasaki, T.; Shimizu, Y.; Koshizaki, N. Blue Luminescent Silicon Nanocrystals Prepared by Ns Pulsed Laser Ablation in Water. *Appl. Phys. Lett.* **2006**, *89* (21), 1-3.

(33) Balachandran, A.; Sreenilayam, S. P.; Madanan, K.; Thomas, S.; Brabazon, D. Nanoparticle Production via Laser Ablation Synthesis in Solution Method and Printed Electronic Application - A Brief Review. *Results Eng.* **2022**, 100646.

(34) Gupta, A.; Swihart, M. T.; Wiggers, H. Luminescent Colloidal Dispersion of Silicon Quantum Dots from Microwave Plasma Synthesis: Exploring the Photoluminescence Behavior across the Visible Spectrum. *Adv. Funct. Mater.* **2009**, *19* (5), 696–703.

(35) Overview, E. Praxair Material Safety Data Sheet Praxair Material Safety Data Sheet. **2012**, 1–10.

(36) Wilcoxon, J. P.; Samara, G. A.; Provencio, P. N. Optical and Electronic Properties of Si Nanoclusters Synthesized in Inverse Micelles. *Phys. Rev. B - Condens. Matter Mater. Phys.* **1999**, *60* (4), 2704–2714.

(37) Veinot, J.; Fok, E.; Boates, K.; Macdonald, J. Chemical Safety : LiAlH4 Reduction of SiCl4. **2006**, *83* (51), 2006.

(38) Mangolini, L. Synthesis, Properties, and Applications of Silicon Nanocrystals. *J. Vac. Sci.*

Technol. B, Nanotechnol. Microelectron. Mater. Process. Meas. Phenom. **2013**, *31* (2).

(39) Cheng, K.; Anthony, R.; Kortshagen, U. R.; Holmes, R. J. High-Efficiency Silicon Nanocrystal Light-Emitting Devices. **2011**, 1952–1956.

(40) Cheng, K. Y.; Anthony, R.; Kortshagen, U. R.; Holmes, R. J. Hybrid Silicon Nanocrystal?Organic Light-Emitting Devices for Infrared Electroluminescence. *Nano Lett.* **2010**, *10* (4), 1154–1157.

(41) Kim, T. W.; Cho, C. H.; Kim, B. H.; Park, S. J. Quantum Confinement Effect in Crystalline Silicon Quantum Dots in Silicon Nitride Grown Using SiH4 and NH3. *Appl. Phys. Lett.* **2006**, *88* (12), 1-3.

(42) Gonzalez, C. M.; Iqbal, M.; Dasog, M.; Piercey, D. G.; Lockwood, R.; Klapötke, T. M.; Veinot, J. G. C. Detection of High-Energy Compounds Using Photoluminescent Silicon Nanocrystal Paper Based Sensors. *Nanoscale* **2014**, *6* (5), 2608–2612.

(43) Robidillo, C. J. T.; Wandelt, S.; Dalangin, R.; Zhang, L.; Yu, H.; Meldrum, A.; Campbell, R. E.; Veinot, J. G. C. Ratiometric Detection of Nerve Agents by Coupling Complementary Properties of Silicon-Based Quantum Dots and Green Fluorescent Protein. *ACS Appl. Mater. Interfaces* **2019**, *11* (36), 33478–33488.

(44) Robidillo, C. J. T.; Aghajamali, M.; Faramus, A.; Sinelnikov, R.; Veinot, J. G. C. Interfacing Enzymes with Silicon Nanocrystals through the Thiol-Ene Reaction. *Nanoscale* **2018**, *10* (39), 18706–18719.

(45) Su, Y.; Wang, C.; Hong, Z.; Sun, W. Thermal Disproportionation for the Synthesis of Silicon Nanocrystals and Their Photoluminescent Properties. *Front. Chem.* **2021**, *9* (August), 1–17.

(46) Park, J. H.; Gu, L.; Von Maltzahn, G.; Ruoslahti, E.; Bhatia, S. N.; Sailor, M. J. Biodegradable Luminescent Porous Silicon Nanoparticles for in Vivo Applications. *Nat. Mater.* **2009**, *8* (4), 331–336.

(47) Fujioka, K.; Hiruoka, M.; Sato, K.; Manabe, N.; Miyasaka, R.; Hanada, S.; Hoshino, A.; Tilley, R. D.; Manome, Y.; Hirakuri, K.; Yamamoto, K. Luminescent Passive-Oxidized Silicon Quantum Dots as Biological Staining Labels and Their Cytotoxicity Effects at High Concentration. *Nanotechnology* **2008**, *19* (41), 1-7.

(48) Wang, L.; Nagesha, D. K.; Selvarasah, S.; Dokmeci, M. R.; Carrier, R. L. Toxicity of CdSe Nanoparticles in Caco-2 Cell Cultures. **2012**, *15*, 1–15.

(49) Cheng, X.; Lowe, S. B.; Reece, P. J.; Gooding, J. J. Colloidal Silicon Quantum Dots: From Preparation to the Modification of Self-Assembled Monolayers (SAMs) for Bio-Applications. *Chem. Soc. Rev.* **2014**, *43* (8), 2680–2700.

(50) Ihtisham, M.; Noori, A.; Yadav, S.; Sarraf, M.; Kumari, P.; Brestic, M.; Imran, M.; Jiang, F.; Yan, X.; Rastogi, A. Silver Nanoparticle's Toxicological Effects and Phytoremediation. *Nanomaterials* **2021**, *11* (9), 1–18.

(51) Nie, P.; Zhao, Y.; Xu, H. Synthesis, Applications, Toxicity and Toxicity Mechanisms of Silver Nanoparticles: A Review. *Ecotoxicol. Environ. Saf.* **2023**, *253*, 114636.

(52) Daniel, M. C.; Astruc, D. Gold Nanoparticles: Assembly, Supramolecular Chemistry, Quantum-Size-Related Properties, and Applications Toward Biology, Catalysis, and Nanotechnology. *Chem. Rev.* **2004**, *104* (1), 293–346.

(53) Abou El-Nour, K. M. M.; Eftaiha, A.; Al-Warthan, A.; Ammar, R. A. A. Synthesis and Applications of Silver Nanoparticles. *Arab. J. Chem.* **2010**, *3* (3), 135–140.

(54) Scheibel, H. G.; Porstendörfer, J. Generation of Monodisperse Ag- and NaCl-Aerosols with Particle Diameters between 2 and 300 Nm. *J. Aerosol Sci.* **1983**, *14* (2), 113–126.

(55) Rafique, M.; Rafique, M. S.; Kalsoom, U.; Afzal, A.; Butt, S. H.; Usman, A. Laser Ablation Synthesis of Silver Nanoparticles in Water and Dependence on Laser Nature. *Opt. Quantum Electron.* **2019**, *51* (6), 1–11.

(56) Sportelli, M. C.; Izzi, M.; Volpe, A.; Clemente, M.; Picca, R. A.; Ancona, A.; Lugarà, P. M.; Palazzo, G.; Cioffi, N. The Pros and Cons of the Use of Laser Ablation Synthesis for the Production of Silver Nano-Antimicrobials. *Antibiotics* **2018**, *7* (3).

(57) Khayati, G. R.; Janghorban, K. The Nanostructure Evolution of Ag Powder Synthesized by High Energy Ball Milling. *Adv. Powder Technol.* **2012**, *23* (3), 393–397.

(58) Lotfy, W. A.; Alkersh, B. M.; Sabry, S. A.; Ghozlan, H. A. Biosynthesis of Silver Nanoparticles by Aspergillus Terreus: Characterization, Optimization, and Biological Activities. *Front. Bioeng. Biotechnol.* **2021**, *9*.

(59) Rosman, N. S. R.; Harun, N. A.; Idris, I.; Wan Ismail, W. I. Nanobiotechnology: Nature-Inspired Silver Nanoparticles towards Green Synthesis. *Energy Environ.* **2021**, *32* (7), 1183–1206.

(60) Iravani, S.; Korbekandi, H.; Mirmohammadi, S. V; Zolfaghari, B. Synthesis of Silver Nanoparticles: Chemical, PhysicIravani, S., Korbekandi, H., Mirmohammadi, S. V, &

Zolfaghari, B. (2014). Synthesis of Silver Nanoparticles: Chemical, Physical and Biological Methods. Research in Pharmaceutical Sciences, 9(6), 385–406. . *Res. Pharm. Sci.* **2014**, *9* (6), 385–406.

(61) Whitehead, C. B.; Özkar, S.; Finke, R. G. LaMer's 1950 Model of Particle Formation: A Review and Critical Analysis of Its Classical Nucleation and Fluctuation Theory Basis, of Competing Models and Mechanisms for Phase-Changes and Particle Formation, and Then of Its Application to Silver Halide, S. *Mater. Adv.* **2021**, *2* (1), 186–235.

(62) You, H.; Fang, J. Particle-Mediated Nucleation and Growth of Solution-Synthesized Metal Nanocrystals: A New Story beyond the LaMer Curve. *Nano Today* **2016**, *11* (2), 145–167.

(63) Jana, S. Advances in Nanoscale Alloys and Intermetallics: Low Temperature Solution Chemistry Synthesis and Application in Catalysis. *Dalt. Trans.* **2015**, *44* (43), 18692–18717.

(64) Liu, B.; Hu, X. *Hollow Micro- and Nanomaterials: Synthesis and Applications*; Elsevier Inc., 2020.

(65) Saravanan, M.; Barik, S. K.; MubarakAli, D.; Prakash, P.; Pugazhendhi, A. Synthesis of Silver Nanoparticles from Bacillus Brevis (NCIM 2533) and Their Antibacterial Activity against Pathogenic Bacteria. *Microb. Pathog.* **2018**, *116*, 221–226.

(66) Krajczewski, J.; Kołątaj, K.; Kudelski, A. Plasmonic Nanoparticles in Chemical Analysis. *RSC Adv.* **2017**, *7* (28), 17559–17576.

(67) Zhang, W.; Zi, X.; Bi, J.; Liu, G.; Cheng, H.; Bao, K.; Qin, L.; Wang, W. Plasmonic Nanomaterials in Dark Field Sensing Systems. *Nanomaterials* **2023**, *13* (13).

(68) Wang, L.; Hasanzadeh Kafshgari, M.; Meunier, M. Optical Properties and Applications of Plasmonic-Metal Nanoparticles. *Adv. Funct. Mater.* **2020**, *30* (51), 1–28.

(69) Amirjani, A.; Kamani, P.; Hosseini, H. R. M.; Sadrnezhaad, S. K. SPR-Based Assay Kit for Rapid Determination of Pb2+. *Anal. Chim. Acta* **2022**, *1220*, 340030.

(70) Cobley, C. M.; Skrabalak, S. E.; Campbell, D. J.; Xia, Y. Shape-Controlled Synthesis of Silver Nanoparticles for Plasmonic and Sensing Applications. *Plasmonics* **2009**, *4* (2), 171–179.

(71) Chen, J.; Huang, M.; Kong, L. Flexible Ag/Nanocellulose Fibers SERS Substrate and Its Applications for in-Situ Hazardous Residues Detection on Food. *Appl. Surf. Sci.* **2020**, *533*, 147454.

(72) Zahoor, M.; Nazir, N.; Iftikhar, M.; Naz, S.; Zekker, I.; Burlakovs, J.; Uddin, F.; Kamran, A. W.; Kallistova, A.; Pimenov, N.; Khan, F. A. A Review on Silver Nanoparticles: Classification, Various Methods of Synthesis, and Their Potential Roles in Biomedical Applications and Water Treatment. *Water (Switzerland)* **2021**, *13* (16), 1–28.

(73) Agnihotri, S.; Mukherji, S.; Mukherji, S. Size-Controlled Silver Nanoparticles Synthesized over the Range 5-100 Nm Using the Same Protocol and Their Antibacterial Efficacy. *RSC Adv.* **2014**, *4* (8), 3974–3983.

(74) Ong, W. T. J.; Nyam, K. L. Evaluation of Silver Nanoparticles in Cosmeceutical and Potential Biosafety Complications. *Saudi J. Biol. Sci.* **2022**, *29* (4), 2085–2094.

(75) Nowak, M.; Tolińska, A.; Marciniak, L.; Skrobańska, M.; Tylkowski, B.; Frankowski, M.; Kaczmarek, M. T.; Jastrzab, R. Green Preparation and Characterization of Silver Nanocolloids Used as Antibacterial Material in Soap. *J. Mater. Sci.* **2022**, *57* (18), 8481–8488.

(76) Villanueva, M. E.; Ghibaudo, M. F.; Tovar, G. I.; Copello, G. J.; Campo Dall' Orto, V. Oligomer-Stabilized Silver Nanoparticles for Antimicrobial Coatings for Plastics. *Nano-Structures and Nano-Objects* **2020**, *24*, 100610.

(77) Beck, F.; Loessl, M.; Baeumner, A. J. Signaling Strategies of Silver Nanoparticles in Optical and Electrochemical Biosensors: Considering Their Potential for the Point-of-Care. *Microchim. Acta* **2023**, *190* (3).

(78) Ibrahim, N.; Jamaluddin, N. D.; Tan, L. L.; Yusof, N. Y. M. A Review on the Development of Gold and Silver Nanoparticles-Based Biosensor as a Detection Strategy of Emerging and Pathogenic RNA Virus. *Sensors* **2021**, *21* (15).

(79) Loiseau, A.; Asila, V.; Boitel-Aullen, G.; Lam, M.; Salmain, M.; Boujday, S. Silver-Based Plasmonic Nanoparticles for and Their Use in Biosensing. *Biosensors* **2019**, *9* (2).

(80) Bélteky, P.; Rónavári, A.; Igaz, N.; Szerencsés, B.; Tóth, I. Y.; Pfeiffer, I.; Kiricsi, M.; Kónya, Z. Silver Nanoparticles: Aggregation Behavior in Biorelevant Conditions and Its Impact on Biological Activity. *Int. J. Nanomedicine* **2019**, *14*, 667–687.

(81) Porrang, S.; Davaran, S.; Rahemi, N.; Allahyari, S.; Mostafavi, E. How Advancing Are Mesoporous Silica Nanoparticles? A Comprehensive Review of the Literature. *Int. J. Nanomedicine* **2022**, *17*, 1803–1827.

(82) Mukhopadhyay, S.; Veroniaina, H.; Chimombe, T.; Han, L.; Zhenghong, W.; Xiaole, Q.

Synthesis and Compatibility Evaluation of Versatile Mesoporous Silica Nanoparticles with Red Blood Cells: An Overview. *RSC Adv.* **2019**, 9 (61), 35566-35578.

(83) Bruckner, J. R.; Bauhof, J.; Gebhardt, J.; Beurer, A. K.; Traa, Y.; Giesselmann, F. Mechanisms and Intermediates in the True Liquid Crystal Templating Synthesis of Mesoporous Silica Materials. *J. Phys. Chem. B* **2021**, *125* (12), 3197–3207.

(84) Nagaraj, M. Liquid Crystals Templating. **2020**, *Crystals*, 10, 648, 1–20.

(85) Hoffmann, F.; Fröba, M. Vitalising Porous Inorganic Silica Networks with Organic Functions—PMOs and Related Hybrid Materials. *Chem. Soc. Rev.* **2011**, *40* (2), 608–620.

(86) Steinbach, J. C.; Fait, F.; Mayer, H. A.; Kandelbauer, A. Sol-Gel-Controlled Size and Morphology of Mesoporous Silica Microspheres Using Hard Templates. *ACS Omega* **2023**, *8* (33), 30273–30284.

(87) Vallet-Regí, M.; Schüth, F.; Lozano, D.; Colilla, M.; Manzano, M. Engineering Mesoporous Silica Nanoparticles for Drug Delivery: Where Are We after Two Decades? *Chem. Soc. Rev.* **2022**, *51* (13), 5365–5451.

(88) Yu, X.; Williams, C. T. Recent Advances in the Applications of Mesoporous Silica in Heterogeneous Catalysis. *Catal. Sci. Technol.* **2022**, *12* (19), 5765–5794.

(89) Cashin, V. B.; Eldridge, D. S.; Yu, A.; Zhao, D. Surface Functionalization and Manipulation of Mesoporous Silica Adsorbents for Improved Removal of Pollutants: A Review. *Environ. Sci. Water Res. Technol.* **2018**, *4* (2), 110–128.

(90) Fowler, C. E.; Khushalani, D.; Lebeau, B.; Mann, S. Nanoscale Materials with Mesostructured Interiors. *Adv. Mater.* **2001**, *13* (9), 649–652.

(91) Hosseinpour, S.; Walsh, L. J.; Xu, C. Biomedical Application of Mesoporous Silica Nanoparticles as Delivery Systems: A Biological Safety Perspective. *J. Mater. Chem. B* **2020**, *8* (43), 9863–9876.

(92) Xu, B.; Li, S.; Shi, R.; Liu, H. Multifunctional Mesoporous Silica Nanoparticles for Biomedical Applications. *Signal Transduct. Target. Ther.* **2023**, *8* (1).

(93) Hu, X.; Zrazhevskiy, P.; Gao, X. Encapsulation of Single Quantum Dots with Mesoporous Silica. *Ann. Biomed. Eng.* **2009**, *37* (10), 1960–1966.

(94) Mancini, M. C.; Kairdolf, B. A.; Smith, A. M.; Nie, S. Oxidative Quenching and Degradation of Polymer-Encapsulated Quantum Dots: New Insights into the Long-Term Fate and Toxicity of Nanocrystals in Vivo. *J. Am. Chem. Soc.* **2008**, *130* (33), 10836–10837.

(95) Moreira, A. F.; Rodrigues, C. F.; Reis, C. A.; Costa, E. C.; Correia, I. J. Gold-Core Silica Shell Nanoparticles Application in Imaging and Therapy: A Review. *Microporous Mesoporous Mater.* **2018**, *270*, 168–179.

(96) Singh, P.; Pandit, S.; Mokkapati, V. R. S. S.; Garg, A.; Ravikumar, V.; Mijakovic, I. Gold Nanoparticles in Diagnostics and Therapeutics for Human Cancer. *Int. J. Mol. Sci.* **2018**, *19* (7).

(97) Li, Z.; Guo, J.; Zhang, M.; Li, G.; Hao, L. Gadolinium-Coated Mesoporous Silica Nanoparticle for Magnetic Resonance Imaging. *Front. Chem.* **2022**, *10*, 1–10.

(98) Alsharif, N. H.; Berger, C. E. M.; Varanasi, S. S.; Chao, Y.; Horrocks, B. R.; Datta, H. K. Alkyl-Capped Silicon Nanocrystals Lack Cytotoxicity and Have Enhanced Intracellular Accumulation in Malignant Cells via Cholesterol-Dependent Endocytosis. *Small* **2009**, *5* (2), 221–228.

(99) Leibl, N.; Haupt, K.; Gonzato, C.; Duma, L. Molecularly Imprinted Polymers for Chemical Sensing: A Tutorial Review. *Chemosensors* **2021**, *9* (6), 1–19.

(100) Belbruno, J. J. Molecularly Imprinted Polymers. *Chem. Rev.* **2019**, *119* (1), 94–119.

(101) Poma, A.; Turner, A. P. F.; Piletsky, S. A. Advances in the Manufacture of MIP Nanoparticles. *Trends Biotechnol.* **2010**, *28* (12), 629–637.

Chapter 2

Molecularly Imprinted Silica on Silicon Nanoparticles as Potential Materials for Drug Delivery

2.1 Introduction

Silicon, a Group 14 element, is notable for its abundance on Earth. As an intrinsic semiconductor, silicon exhibits unique characteristics at the nanoscale, including size-dependent photoluminescence. Combining the non-toxicity and photoluminescent properties of silicon nanomaterials led to promising results in biological applications such as bioimaging and biosensing.[1] Sailor et al. demonstrated the use of SiNPs in therapeutic applications by functionalizing them with doxorubicin, chemotherapeutic agent, and using the particles in drug delivery applications.[2] Porous materials provide large pore volumes that allow adsorption and desorption of therapeutic agents at controlled rates for improved therapeutic efficiency.[3] For this purpose, preparing hybrid materials by coating the SiNPs with porous silica shell could improve the efficiency of drug delivery to biological systems. Regli et al. prepared mesoporous silica encapsulated SiNPs for the drug release from the mesoporous shell.[4] It was concluded that the multifunctional material that combined the biocompatibility of both SiNPs and mesoporous silica hold potential as a drug delivery agent. Thus, preparing hybrid materials by combining the mesoporous silica and nanoparticles with distinct properties could merge the non-toxic and

luminescent properties of SiNPs, and the large surface area and adsorbent properties of mesoporous silica to create multifunctional materials tailored for biological applications.

One drawback of using hybrid materials of mesoporous silica with nanoparticles in drug delivery applications is the non-selective nature of the system. Molecular imprinting provides selectivity towards an imprinted drug molecule as well as controlled drug release.[5] For this reason, molecular imprinting is an attractive approach to produce materials with the needed selectivity.

Molecularly imprinted polymers (MIPs) exhibit properties close to those of natural receptors in terms of selectivity and can be modified for a wide range of target molecules.[6] Wang et al. demonstrated the preparation of MIP coated fluorescent SiNPs by using two templates, the extracellular region of human epidermal growth factor receptor-2 for targeted imaging and doxorubicin for therapy.[7] The imprinted sites on the MIP surface were used to recognize the corresponding protein that allowed MIP to specifically binds to target cells. The hybrid material was used for targeted imaging by taking advantage of the photoluminescent properties of SiNPs.

In this regard, we demonstrate the preparation of SiNPs encapsulated in surface imprinted mesoporous silica to combine the photoluminescent properties of SiNPs, non-toxicity and large surface area of mesoporous silica, and high selectivity of MIPs. Once in hand, possible applications of these multifunctional hybrid materials are investigated.

2.2 Experimental

2.2.1 Reagents and Materials

Hydrofluoric acid (48-50% HF (aq), Fisher Scientific), reagent grades of toluene (≥99.5%), hexanes (≥99%), chloroform (≥99.8%), sulfuric acid (H_2SO_4, 95.0-98.0%), ethanol (EtOH, 95%),

methanol (MeOH, ≥99.8%), ethyl acetate (EtOAc, ≥99.5%), were obtained from Sigma Aldrich. 1-dodecene (99%) was purchased from Sigma Aldrich. Trichlorosilane (99%), fuming sulfuric acid (reagent grade, 20% SO_3), glass beads (~5 mm), and 4 Å molecular sieves (beads, 4–8 mesh) were purchased from Millipore Sigma. Magnesium sulfate (reagent grade) was obtained from Caledon Laboratory Chemicals. Calcium carbonate (certified ACS grade) was purchased from Thermo Fisher Scientific. Cetrimonium bromide (CTAB), tetraethyl orthosilicate (TEOS, ≥99%), vinyltrimethoxysilane (98%), sodium hydroxide (NaOH, ≥98%, pellets, anhydrous), ethyl acetate (EtOAc, ≥99.5%) were purchased from Sigma-Aldrich. Ethylene glycol dimethacrylate (≥97.5%), 2,2′-azobis(2-methylpropionitrile) (AIBN, ≥98%), methacrylic acid (≥99%) and ibuprofen (IBU) were also obtained from Sigma Aldrich. Hydrochloric acid (HCl, 37%, reagent grade) was purchased from ACP Chemicals. Dry toluene was obtained from a solvent purification system (Innovative Technologies, Inc.) prior to use; all other reagents were used as received.

2.2.2 Preparation of Silicon Nanoparticles

2.2.2.1 Preparation of Hydrogen Silsesquioxane

Hydrogen silsesquioxane **(**HSQ) was synthesized using a modified literature preparation.[8] Briefly, dry toluene (210 mL) was added dropwise to a solution of concentrated sulfuric acid (70 mL) and fuming sulfuric acid (32.5 mL). Subsequently, a mixture of dry toluene (510 mL) and trichlorosilane (75 mL) was added dropwise to the solution with stirring. The resulting mixture was then stirred for 30 minutes. A water trap is used to monitor and remove hydrochloric acid gas formed during the reaction. Then, the entire mixture was placed in a separation funnel and washed with 600 mL of concentrated sulfuric acid. The aqueous layer was removed along with any

colourless precipitate. The organic layer was collected and dried over calcium carbonate (ca. 5 g) and magnesium sulphate (ca. 5 g). The toluene was evaporated via rotary evaporation and the resulting white solid product (~24 g) was kept under vacuum until further use. The product was used without further characterization.

2.2.2.2 Preparation of Silicon Nanoparticles Embedded in Silicon Dioxide

Silicon nanoparticles embedded in a silicon dioxide (SiNPs/SiO_2) matrix were synthesized using a method established by our laboratory.[8] Briefly, 3 g of HSQ was thermally processed in a tube furnace (the ramp rate is 4°C/min) under reducing atmosphere (5% H_2/95% Ar) at the peak processing temperature of 1300°C for an hour to obtain SiNPs with average size of 9 nm in a silicon oxide matrix. The resulting brown composite material was cooled to room temperature, and ground in ethanol to a fine slurry using an agate mortar and pestle. Following this, the slurry was put into a flask containing glass beads and subjected to shaking for 16 hours using a wrist action shaker to obtain a light brown powder.

2.2.2.3 Preparation of Hydride Terminated Silicon Nanoparticles

Liberation of the hydride-terminated silicon nanoparticles **(**H-SiNPs) from the SiNP/SiO_2 composite was carried out using HF etching.[8] SiNP/SiO_2 composite (500 mg) was weighed into a 50-mL Teflon beaker. 5 mL of ethanol was added followed by the sonication for 5 minutes to disperse the composite. With stirring, 5 mL water was added followed by the addition of 5 mL of 49% HF to the composite. The suspension changed colour (brown to pale yellow) over 40 min of stirring period, indicating the etching was complete. The H-SiNPs were extracted using toluene (3

x 20 mL), and centrifuged (3000 rpm for 10 min) to precipitate the SiNPs. The supernatant toluene was removed, and the precipitated H-SiNPs were used immediately.

2.2.2.4 Functionalization of Hydride Terminated Silicon Nanoparticles

A procedure established in our laboratory was used to functionalize the hydride-terminated SiNPs.[8] The precipitate of H-SiNPs that was obtained in Section 2.2.2.3 was resuspended in 50 mL of 1-dodecene via sonication. Thermally-induced hydrosilylation was performed by heating the suspension under Ar at 190°C for 24 h. The resultant product was well-dispersed and had an orange-brown colour. The alkyl functionalized SiNPs (alkyl-SiNPs) were purified by solvent/antisolvent washing using ethanol and methanol (3:1). This solvent combination provides solubility for the excess ligands as the particles are not dispersible. The particles were suspended in solvent/antisolvent via sonication and purified by three cycles of centrifuging/resuspension at 11000 rpm for 20 minutes/cycle. Then, the precipitate was collected and resuspended in toluene via sonication. The dispersion was filtered using a hydrophobic polytetrafluoroethylene (PTFE) filter (0.45 μm). The filtrate was transferred to a vial and stored at room temperature in the dark until further use. The alkyl-SiNPs were characterized by Fourier-transform infrared (FTIR) spectroscopy and scanning electron microscopy (SEM).

2.2.3 Encapsulation of Silicon Nanoparticles in Mesoporous Silica

Mesoporous silica encapsulated silicon nanoparticles (MSNPs-SiNPs) were synthesized using a variation of a procedure developed in our laboratory.[4] A chloroform dispersion of alkyl-SiNPs (50 mg/mL) was gradually added to a solution of CTAB (5 mL in water, 55 mM). The

resulting solution was transparent yellow. The CTAB/SiNPs mixture was stirred vigorously at 50°C for 30 min to form an emulsion. Subsequently, 45 mL of aqueous NaOH (13 mM), which had been pre-heated to 50°C, was added followed by the sequential addition of TEOS (0.5 mL, 2 mmol) and ethyl acetate (3 mL, 30 mmol). After the addition, the mixture turned from transparent yellow to cloudy pale-yellow consistent with the formation of MSNPs. The mixture was stirred for 3 hours. Following this, the precipitate was collected by centrifuging once at 11400 rpm for 20 minutes. Then, the precipitate was resuspended in EtOH:H_2O (v:v; 1:1) via sonication and purified by three cycles of centrifuging/resuspension at 11400 rpm for 20 minutes/cycle using EtOH:H_2O (v:v; 1:1) mixture to remove excess reagents and surface bonded CTAB. The particles obtained were transferred into a glass vial and suspended in EtOH (20 mL) for further use.

CTAB inside the pores of MSNPs was removed by adding HCl (0.1 M, 40 μL) to the particles in EtOH (20 mL) and heating the mixture to 70˚C. It was stirred vigorously for 24 h at 70˚C, followed by cooling to room temperature. The precipitate was collected by centrifuging once at 11400 rpm for 20 minutes. The precipitate was resuspended in EtOH:H_2O (v:v; 1:1) via sonication and purified by three cycles of centrifuging/resuspension at 11400 rpm for 20 minutes/cycle using EtOH:H_2O (v:v; 1:1) mixture. The precipitate was collected and resuspended in EtOH (20 mL) and stored in a glass vial until further use. The MSNPs-SiNPs were characterized using SEM, transmission electron microscopy (TEM), photoluminescence (PL) spectroscopy and FTIR spectroscopy.

2.2.4 Surface functionalization

The surface functionalization procedure was adapted from literature.[9] Alkene groups were introduced to the surface of the MSNPs-SiNPs to make the surface available for molecular

imprinting. Vinyltrimethyoxysilane (0.5 mL, 3 mmol) was added to a suspension of 5 mL MSNPs-SiNPs (prepared in Section 2.2.3) in EtOH:H_2O (v:v; 1:1) and the mixture was stirred for 24 h at 50˚C. The precipitate was collected by centrifuging once at 11400 rpm for 20 minutes. The precipitate was resuspended in EtOH:H_2O (v:v; 1:1) via sonication and purified by three cycles of centrifuging/resuspension at 11400 rpm for 20 minutes/cycle using EtOH:H_2O (v:v; 1:1) mixture. The pellet was collected and resuspended in EtOH (10 mL). The surface functionalized MSNPs-SiNPs were characterized using FTIR spectroscopy.

2.2.5 Molecular Imprinting on MSNPs

Surface molecular imprinting of the vinyl functionalized MSNPs-SiNPs (vinyl-MSNPs-SiNPs) was achieved by coating the surface with poly(ethylene glycol dimethacrylate).[9] Surface polymerization of the vinyl-MSNPs-SiNPs was achieved using MAA (56 μL, 0.7 mmol) as the monomer, EGDMA (0.6 mL, 3 mmol) as the cross-linking agent, AIBN (15 mg, 0.1 mmol) as the initiator and IBU (21 mg, 0.1 mmol) as the template. The vinyl-MSNPs-SiNPs (prepared in Section 2.2.4) were dispersed in 20 mL EtOH:H_2O (v:v; 1:1) with exposure to a bath sonicator and the dispersion was transferred into a 50 mL round bottom flask. The dispersion had a pale-yellow colour. The monomer, crosslinker and template were added sequentially to the reaction flask while stirring. Subsequently, the initiator was added and the mixture was stirred for 24 h at 75°C. The precipitate was collected by centrifuging once at 5000 rpm for 20 minutes. Then, it was resuspended in EtOH:H_2O (v:v; 1:1) via sonication and purified by three cycles of centrifuging/resuspension at 5000 rpm for 20 minutes/cycle using EtOH:H_2O (v:v; 1:1) mixture to remove the unreacted monomers, excess reagents, and surface bonded templates. The purified particles were suspended in EtOH (25 mL) for further use.

To remove the template, the surface molecularly imprinted MSNPs-SiNPs (MIPs-MSNPs-SiNPs) in EtOH (25 mL) were refluxed for 12 h. The precipitate was collected by centrifuging once at 5000 rpm for 20 minutes. Then, it was resuspended in EtOH:H_2O (v:v; 1:1) via sonication and purified by three cycles of centrifuging/resuspension at 5000 rpm for 20 minutes/cycle using EtOH:H_2O (v:v; 1:1) mixture to remove the extracted templates. MIPs-MSNPs-SiNPs were dried under vacuum and stored in a glass vial for further use. The MIPs-MSNPs-SiNPs were characterized by SEM, TEM, and FTIR spectroscopy. The identical procedure (except the template addition during polymerization and the template removal via extraction) was used to produce the MSNPs-SiNPs with the nonimprinted polymer on the surface (NIPs-MSNPs-SiNPs).

2.2.6 Template Release

To evaluate template release, template removed MIPs-MSNPs-SiNPs were first loaded with IBU. To do this, vacuum dried MIPs-MSNPs-SiNPs (15 mg, without the template) was suspended in 10 mL of EtOH:H_2O (v:v; 1:1) via sonication. IBU (5 mg/mL) in EtOH:H_2O (v:v; 1:1) was added to the MIPs-MSNPs-SiNPs. The mixture was stirred for 24 h at room temperature. The loaded particles were collected by centrifuging at 5000 rpm for 20 minutes. The loaded particles that remained as the precipitate were then resuspended in EtOH:H_2O (v:v; 1:1) via sonication and purified by three cycles of centrifuging/resuspension at 5000 rpm for 20 minutes/cycle using EtOH:H_2O (v:v; 1:1) to remove excess template. They were transferred to a clean test tube and 10 mL of phosphate buffer (0.1 M, pH=7.4) was added. The particles were suspended in phosphate buffer via sonicating briefly. The mixture was centrifuged for 5 minutes at 5000 rpm at predetermined time intervals. Then, 100 μL of the supernatant was extracted from the test tube into a vial and diluted to 5 mL with distilled water. The solutions were analysed using

UV-vis spectroscopy monitoring the absorption wavelength at 221 nm. The objective of this study was to determine the quantity of IBU that was released by the MIPs-MSNPs-SiNPs. Standard solutions were prepared with 1.2, 2.4, 3.6, 4.8 and 7.2 mg/mL of IBU using serial dilution method from a 10 mg/mL stock solution. The UV-vis spectra of the standards were recorded and a calibration curve was obtained.

2.2.7 Material Characterization and Instrumentation

FTIR spectra were acquired using a Thermo Nicolet 8700 FTIR Spectrometer. Samples were acquired as KBr pellets (powder samples prepared using ~1-3 mg sample per ~250 mg KBr). The FTIR spectrum of alkyl-SiNPs was obtained via preparing the sample using drop casting method from toluene suspension. SEM images were obtained using Zeiss Sigma Field Emission scanning electron microscope equipped with the secondary electron detector. SEM samples were suspended in EtOH (1-2 mL) and deposited onto the silica wafer sample stub. SEM sample of the alkyl-SiNPs was prepared by depositing the toluene suspension onto the silica wafer sample stub. The samples were dried in air. The size distribution analyses were done using ImageJ software and at least 300 particles were measured to obtain the average shifted histograms. TEM was performed on a JEOL JEMARM200CF S/TEM electron microscope at an accelerating voltage of 200 kV. Samples were drop-coated onto a carbon-coated copper grid. A Hewlett Packard 8453 UV-vis Spectrophotometer was used to obtain UV-vis data.

2.3 Results and Discussion

The preparation of MIPs-MSNPs-SiNPs allows the formation of a multifunctional hybrid material that combines the advantages of each constituent - the optical properties of SiNPs, nontoxicity and large surface area of mesoporous silica, and selectivity of MIPs. In present study, the synthesis and characterization of one such hybrid were explored.

2.3.1 Silicon Nanoparticles

Scheme 2.1 shows the formation of the SiNPs via the high temperature processing of HSQ under reducing atmosphere. HSQ was thermally processed under reducing atmosphere at the peak processing temperature of 1300°C to obtain SiNPs with average size of 9 nm in a silicon oxide matrix. The light brown powder indicated the presence of SiNPs. H-SiNPs from the SiNP/SiO_2 composite was obtained using HF etching. Finally, alkyl-SiNPs was prepared via thermally-induced hydrosilylation.

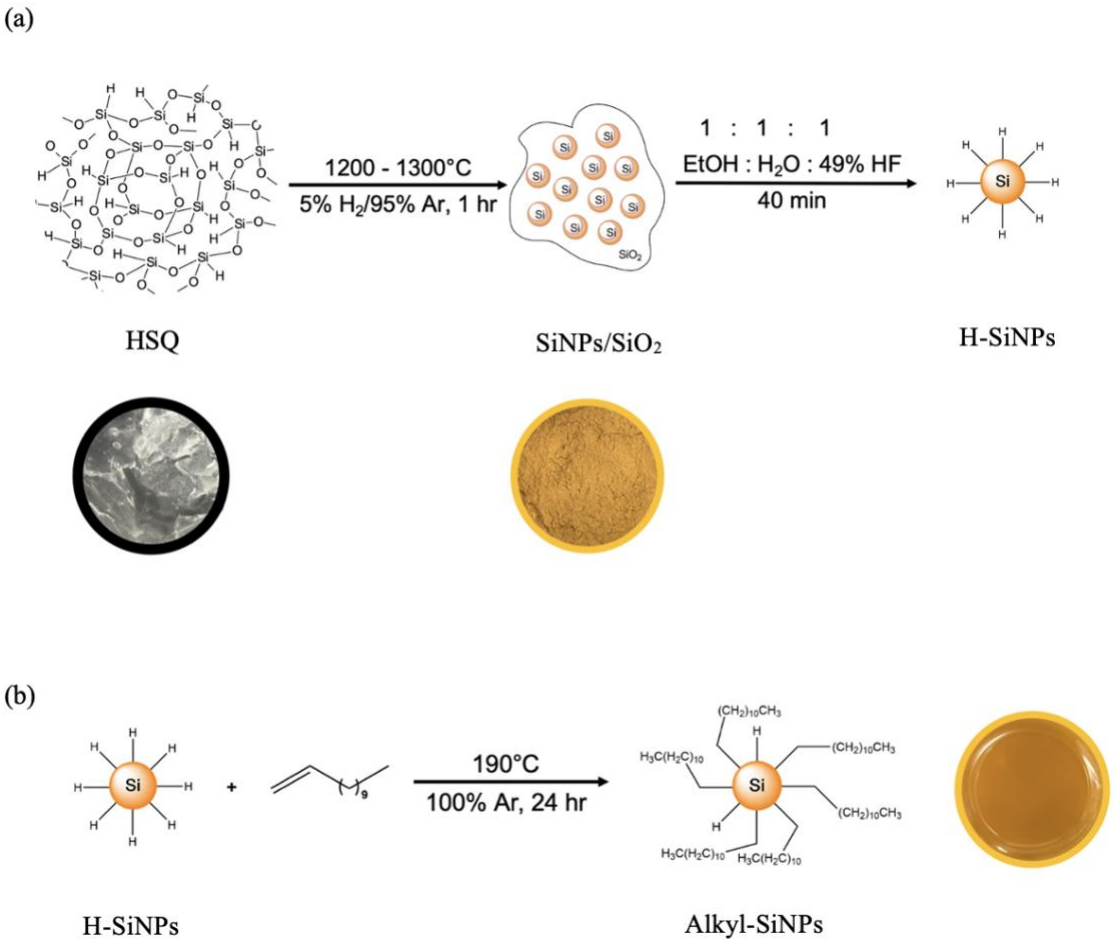

Scheme 2.1. The synthesis of SiNPs via the high temperature processing of HSQ. (a) The preparation of H-SiNPs, (b) The preparation of alkyl-SiNPs. Pictures show the colour of the samples.

Secondary electron scanning electron microscopy was used to determine the size and morphology of the alkyl-SiNPs (Figure 2.1a). For the size analysis, 300 particles were evaluated to obtain the average-shifted histogram (Figure 2.1b). The alkyl-SiNPs exhibit a pseudospherical shape with an average diameter of 10.1 ± 1.5 nm.

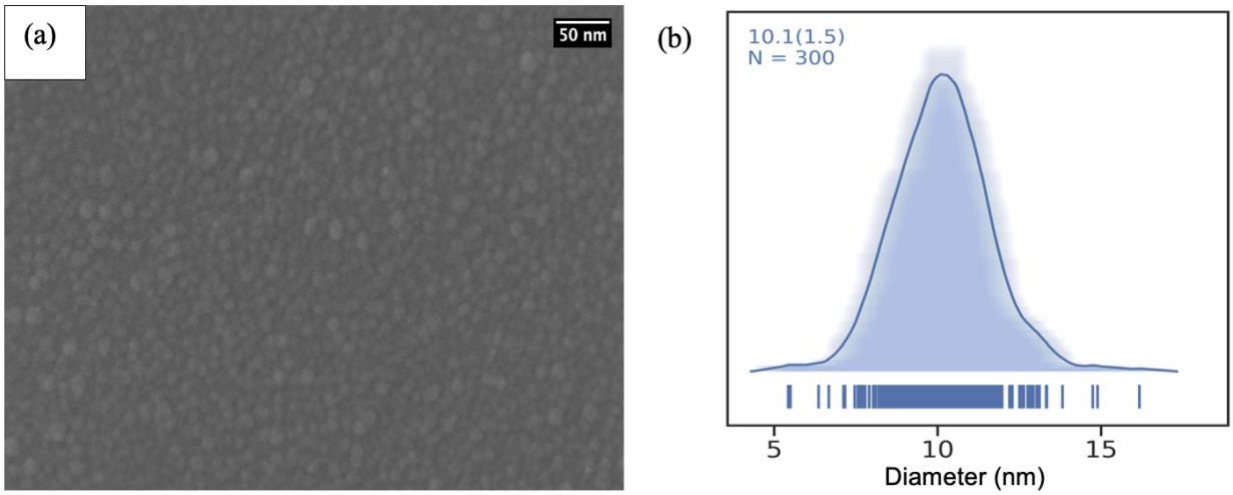

Figure 2.1. (a) Secondary electron SEM image of alkyl-SiNPs, (b) Average-shifted histogram of alkyl-SiNPs.

FTIR provides identification of the chemical bonds and the corresponding functional groups on the alkyl-SiNPs. FTIR spectrum of the alkyl-SiNPs is shown in Figure 2.2. Multiple peaks related to C-H stretching of the alkyl groups appeared at around 2900 cm^{-1}. The peak at 2173 cm^{-1} was attributed to characteristic Si−H vibrational mode. Consistent with previous literature, the presence of this peak indicated that the functionalization of the H-SiNPs was not complete.[8] The multiple peaks at around 1450 cm^{-1} were related to the C-H bending vibrations of the alkyl groups. Si-O stretching vibration appeared at 1039 cm^{-1}. The intensity of the Si−O stretching can serve as a qualitative indicator for the degree of surface oxidation and suggested that surface oxidation occurred during functionalization and handling.

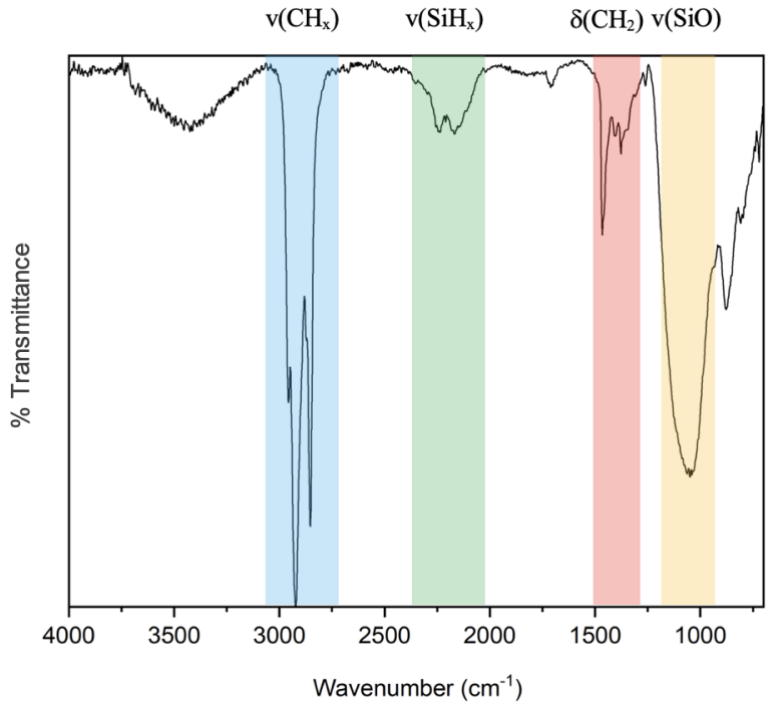

Figure 2.2. FTIR spectrum of the alkyl-SiNPs. The sample was prepared using drop casting method from toluene suspension.

2.3.2 Mesoporous Silica Encapsulation of Silicon Nanoparticles

We attempted to deposit mesoporous silica onto the surface of SiNPs described in Section 2.2.2 via a sol-gel approach. A schematic representation of the synthesis and the structure of the surfactant are shown in Scheme 2.2a and Scheme 2.2b, respectively. A chloroform dispersion of alkyl-SiNPs (50mg/mL) were gradually added to a solution of CTAB (5 mL in water, 55 mM) with vigorous stirring to form an emulsion. Subsequently, 45 mL of aqueous NaOH (13 mM), which had been pre-heated to 50°C, was added followed by the sequential addition of TEOS (0.5 mL, 2 mmol) and ethyl acetate (3 mL, 30 mmol). After stirred for 3 hours, the mixture turned from transparent yellow to cloudy pale-yellow, indicating the formation of MSNPs.

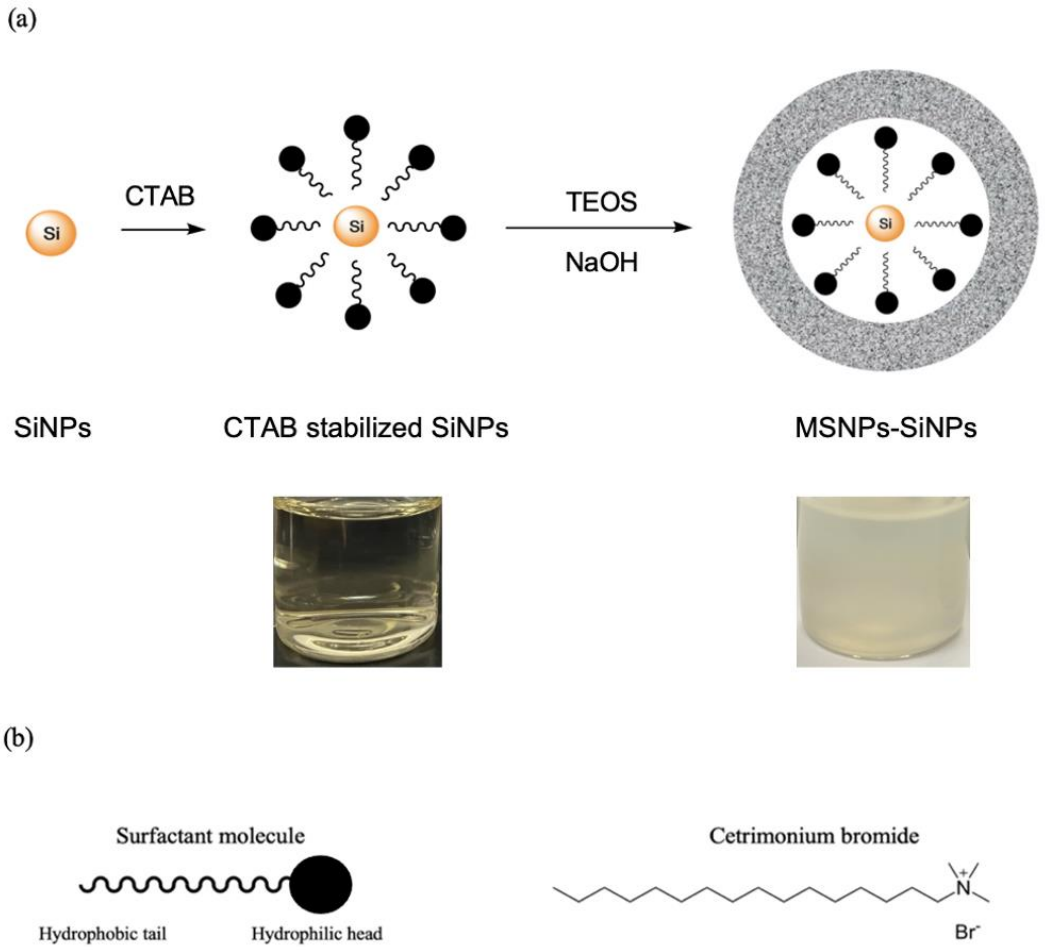

Scheme 2.2. (a) Synthesis of MSNPs-SiNPs. (b) The structure of the surfactant molecule, CTAB.

To investigate the size and morphology of the MSNPs-SiNPs, SEM was used. Secondary electron SEM images of MSNPs-SiNPs showed the pseudospherical shape of the particles with dimensions of 115 ± 16 nm (Figure 2.3 a, b, and c). The primary reason for developing MSNPs-SiNPs stemmed from the desire to prepare hybrid materials that drew on the optical response of the SiNP component. Therefore, the PL properties of the MSNPs-SiNPs were examined. The MSNPs-SiNPs showed PL maximum at 593 nm (Figure 2.3d). The Veinot group has demonstrated that dodecyl-terminated SiNPs of similar dimensions show a PL maximum at *ca.* 900 nm.[8] The PL spectrum we obtained showed that the PL maximum of the encapsulated SiNPs is blue-shifted to

593 nm. Similarly, Regli et al. demonstrated that the PL maximum of the dodecyl-terminated SiNPs blue-shifted from 750 nm to 670 nm upon encapsulation of the dodecyl-terminated SiNPs with the mesoporous shell.[4] This blue-shift is tentatively attributed to surface oxidation of the SiNPs arising from exposure to the base catalyst required for the sol-gel encapsulation.[4] In the preparation of MSNPs-SiNPs, a sol-gel reaction was performed using 13 mM aqueous NaOH.

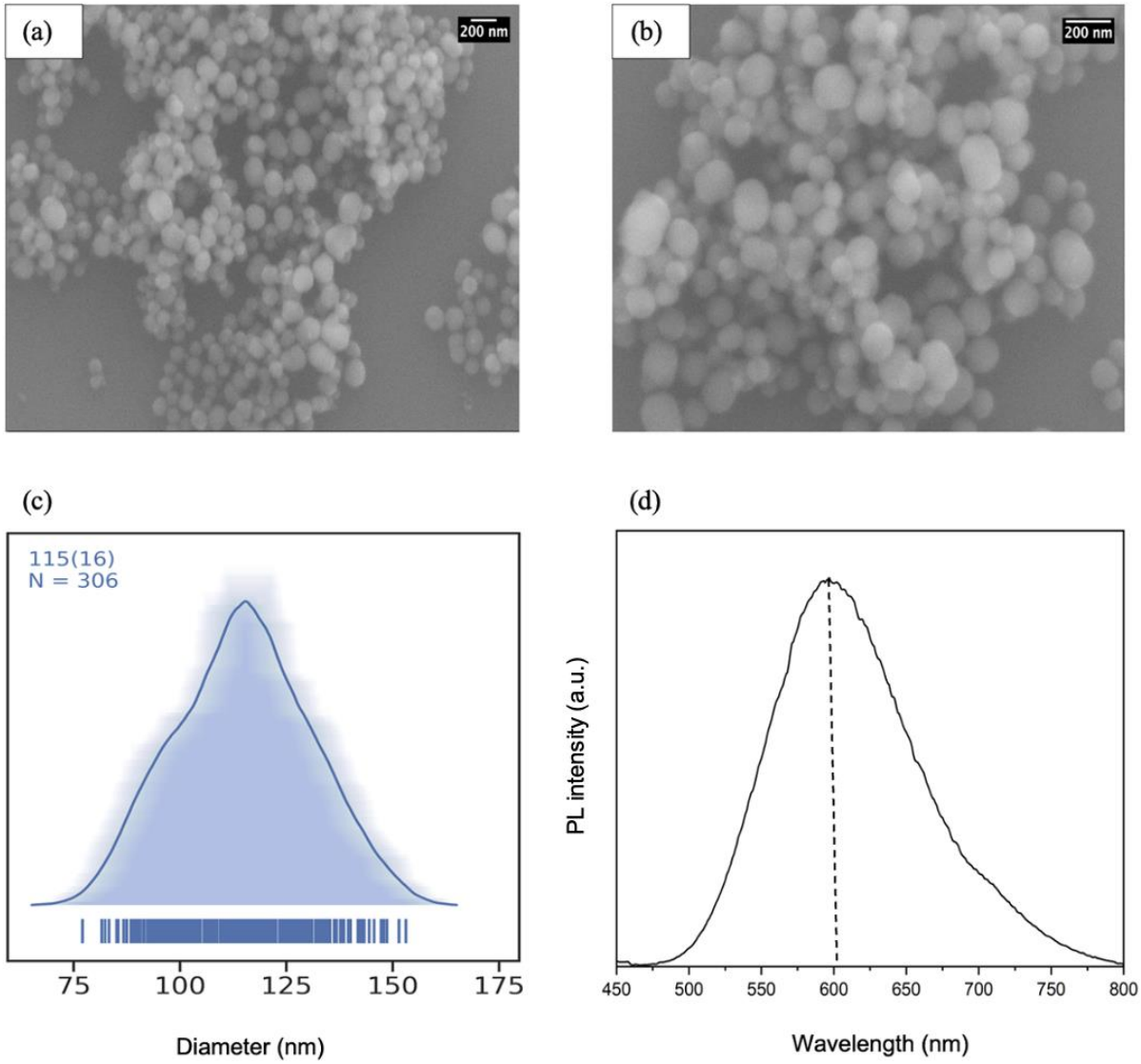

Figure 2.3. (a), (b) Secondary electron SEM images of MSNPs-SiNPs, (c) average-shifted histogram of MSNPs-SiNPs, (d) Photoluminescence spectrum of MSNPs-SiNPs.

To further investigate the morphology of the MSNPs-SiNPs, TEM was used. Bright field TEM images of the MSNPs-SiNPs showed the pseudospherical shape of the particles together with agglomerated SiNPs in/around them.

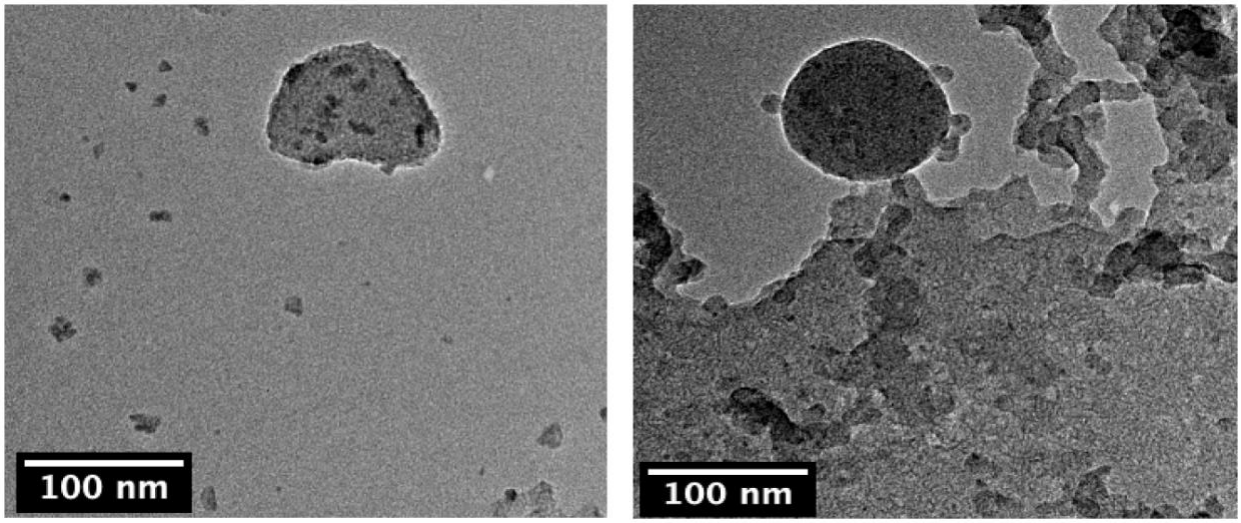

Figure 2.4. Brightfield TEM images of MSNPs-SiNPs. The presence of the agglomerated SiNPs in/around the MSNPs.

In summary, secondary electron SEM imaging of the alkyl-SiNPs showed the pseudospherical shape of the particles. Surface functionalization of the H-SiNPs with alkyl groups was successful as indicated by FTIR spectroscopy. SEM and TEM images showed the pseudospherical shape of MSNPs-SiNPs. Blue-shift was observed in the PL maximum of the SiNPs which indicated the oxidation of SiNPs during sol-gel reaction. Next, MSNPs-SiNPs were used to prepare the hybrid material coated with MIPs to provide selectivity for target molecules in drug delivery applications.

2.3.3 Surface Molecularly Imprinting on Silica

Alkene groups were introduced to the surface of MSNPs-SiNPs to make the surface available for molecular imprinting. The presence of vinyl groups on the surface of MSNPs-SiNPs was confirmed using FTIR spectroscopy (Figure 2.8 in page 21). Surface molecular imprinting of vinyl-MSNPs-SiNPs was achieved by coating the surface with poly(ethylene glycol dimethacrylate) via radical-initiated polymerization of MAA monomers. IBU was used as the template molecule. Then, internally bonded templates were removed by refluxing with ethanol. The formation of MIPs-MSNPs-SiNPs is summarized in Figure 2.5a. The proposed structure of the poly(ethylene glycol dimethacrylate) is shown in Figure 2.5b.

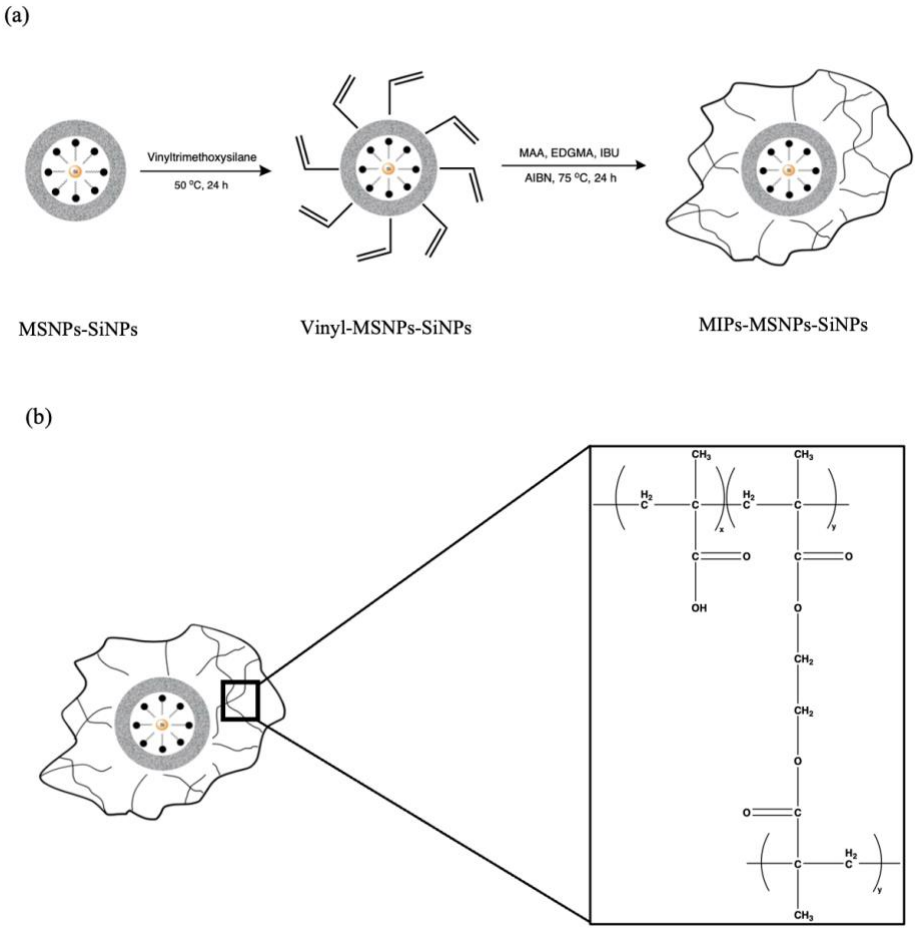

Figure 2.5. (a) The surface functionalization and surface imprinting of the MSNPs-SiNPs and (b) The molecular structure of the poly(ethylene glycol dimethacrylate).

Figure 2.6 shows the secondary electron SEM images of MIPs-MSNPs-SiNPs. When compared to the SEM images of the MSNPs-SiNPs (Figure 2.3), we note that the MIPs-MSNPs-SiNPs were densely packed inside the polymer coating. Secondary electron SEM images also indicated the shapes of the particles were no longer spherical and showed somewhat random shapes consisting with the presence of a polymer coating.

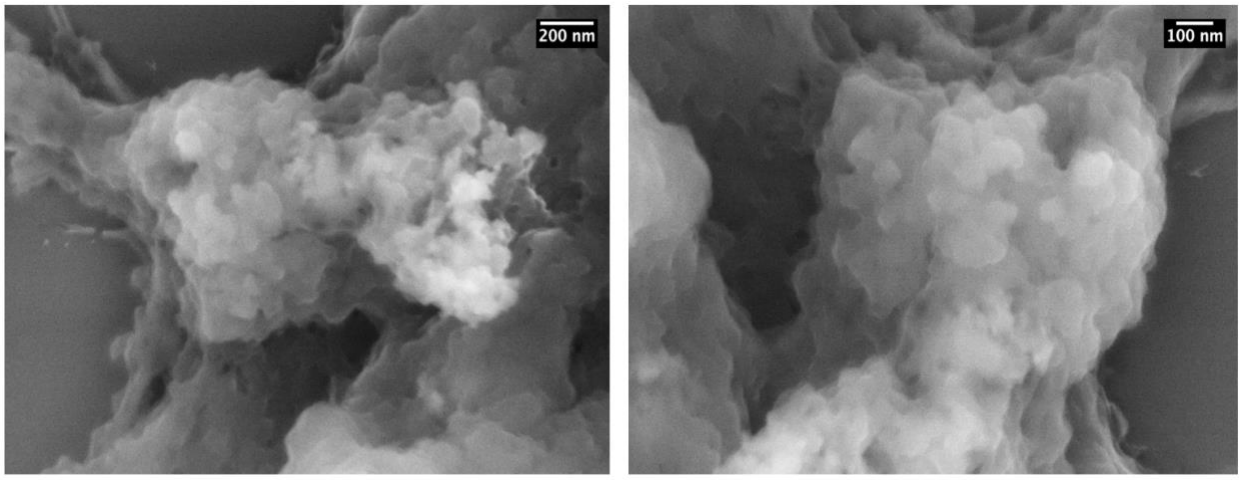

Figure 2.6. Secondary electron SEM images of MIPs-MSNPs-SiNPs.

To further investigate the presence of the MSNPs-SiNPs inside the polymer, TEM was employed. Brightfield TEM images of the MIPs-MSNPs-SiNPs are shown in Figure 2.7a. Bright regions can be tentatively attributed to the presence of agglomerated MSNPs-SiNPs. Higher magnification bright field TEM image of the MIPs-MSNPs-SiNPs (Figure 2.7b) showed pseudospherical spots with sizes of *ca.* 100 nm that can be reasonably attributed to MSNPs-SiNPs embedded inside the polymer. It also showed the presence of the smaller particles with sizes *ca.* 10 nm that may be freestanding SiNPs. Figures 2.7c and d show the dark field TEM images of the MIPs-MSNPs-SiNPs. The bright spots with the size of *ca.* 10 nm showed the presence of SiNPs.

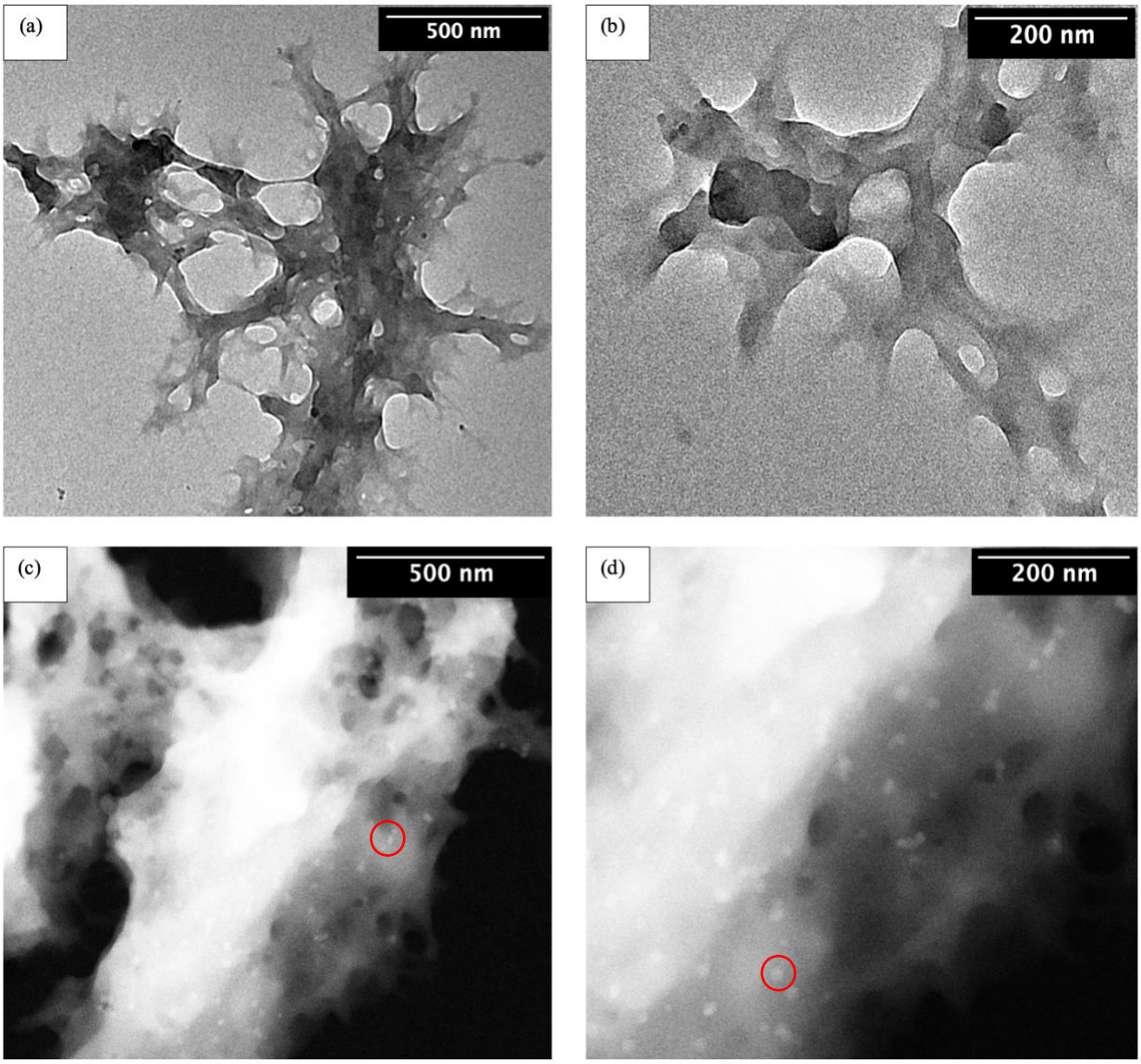

Figure 2.7. (a and b) Bright field TEM images of MIPs-MSNPs-SiNPs. (c and d) Dark field TEM images of MIPs-MSNPs-SiNPs. SiNPs (bright spots) are embedded in the polymer. SiNPs are shown with red circles.

We now turn our attention to the surface chemistry of the present materials. FTIR provides identification of chemical bonds and the corresponding functional groups on/within the presented hybrid materials. FTIR spectra of the MSNPs-SiNPs (blue trace), vinyl-MSNPs-SiNPs (red trace) and MIPs-MSNPs-SiNPs (black trace) are shown in Figure 2.8. The peaks at 3432 cm^{-1}, 1073 cm^{-1}, 956 cm^{-1} and 798 cm^{-1} are attributed to characteristic silica vibrations: Si-O-H stretching,

asymmetric stretching vibration of Si-O-Si, Si-O-H bending and symmetric stretching vibration of Si-O-Si, respectively.[10,11] The sharp peak at 1735 cm^{-1} is attributed to the C=O stretching vibration of the polymer. The peak at 1253 cm^{-1} is assigned to the C–O symmetric stretching of the ester group of the polymer. Multiple peaks related to C-H stretching vibrations appeared at around 2950 cm^{-1}. The peaks at 1450 cm^{-1} and 1388 cm^{-1} indicates the presence of $-CH_2$ and $-CH_3$ groups, respectively. Upon functionalization with the vinyl groups, a new peak appeared at 2985 cm^{-1} in the spectrum of vinyl-MSNPs-SiNPs (red trace). This peak is associated with C-H stretching of the vinyl group. The same peak appeared in the MIPs-MSNPs-SiNPs (black trace) and this suggests that polymerization reaction was not complete.

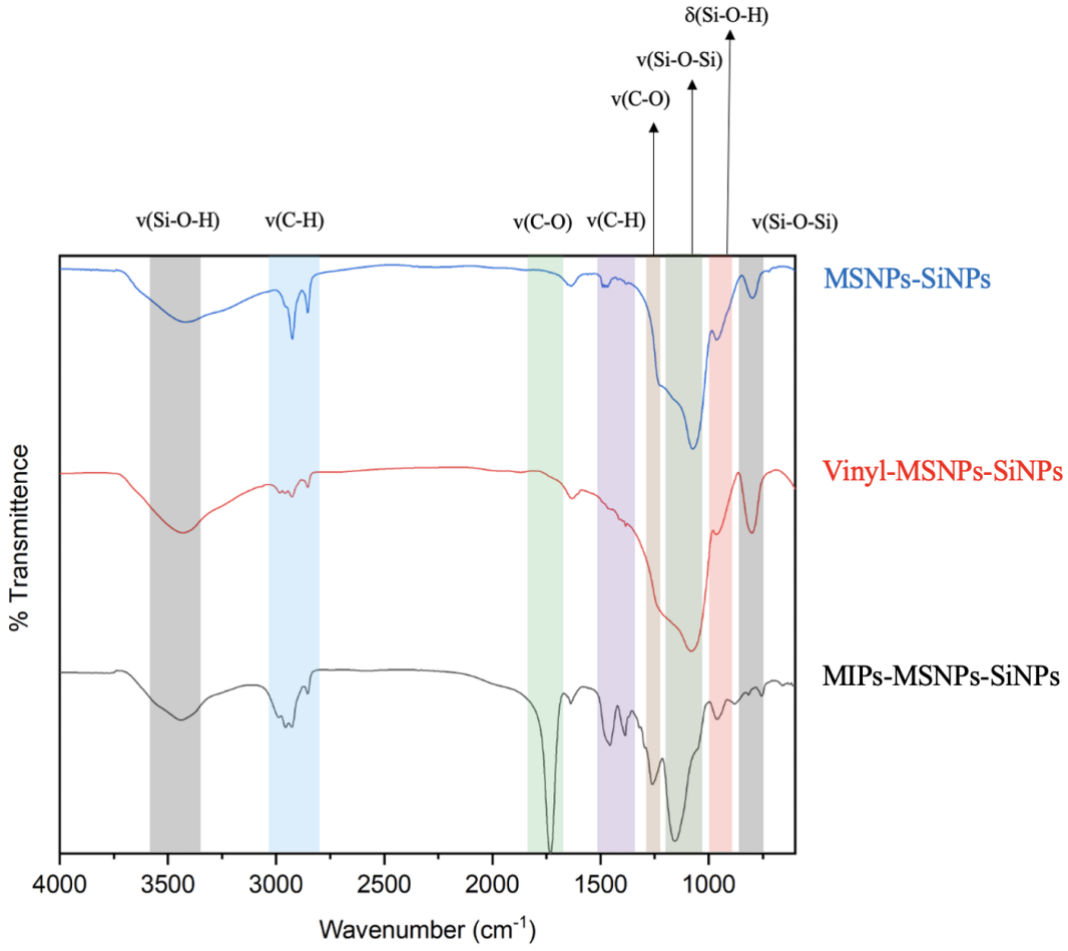

Figure 2.8. FTIR spectra of MSNPs-SiNPs (blue trace), vinyl-MSNPs-SiNPs (red trace) and MIPs-MSNPs-SiNPs (black trace). Samples were acquired as KBr pellets.

The MSNPs-SiNPs, vinyl-MSNPs-SiNPs and MIPs-MSNPs-SiNPs were characterized by SEM, TEM, FTIR and PL spectroscopy. The functional groups of the particles were characterized by FTIR spectroscopy, showing the presence of characteristic silica vibrations, vinyl functionalization, and surface imprinting. Next, the possible use of the hybrid material in the drug release applications were investigated.

2.3.4 IBU Release by the Imprinted Particles

The release of IBU from the loaded particles was performed using the procedure outlined in Section 2.2.6. Figure 2.9a shows the absorbance of an aliquot of the supernatant at a predetermined specified time interval. The characteristic absorbance intensity of IBU at 221 nm increased and then decreased over time. It was used to determine the concentration of IBU in the mixture and a release curve was plotted (Figure 2.9b). The initial sharp increase indicated the release of the IBU from the particles into the mixture. The concentration of IBU in the mixture decreased after 20 h and remained nearly unchanged at 30 hours. The decrease in the concentration of IBU indicated that there was a re-uptake of the IBU into the polymer matrix. The maximum concentration of the IBU in the mixture was determined to be 3.1 mg/mL. The desorption capacity of the MIPs-MSNPs-SiNPs was calculated as 2.07 mg/mg (mg of template desorbed per mg of the particles) using a method described in literature.[12,13]

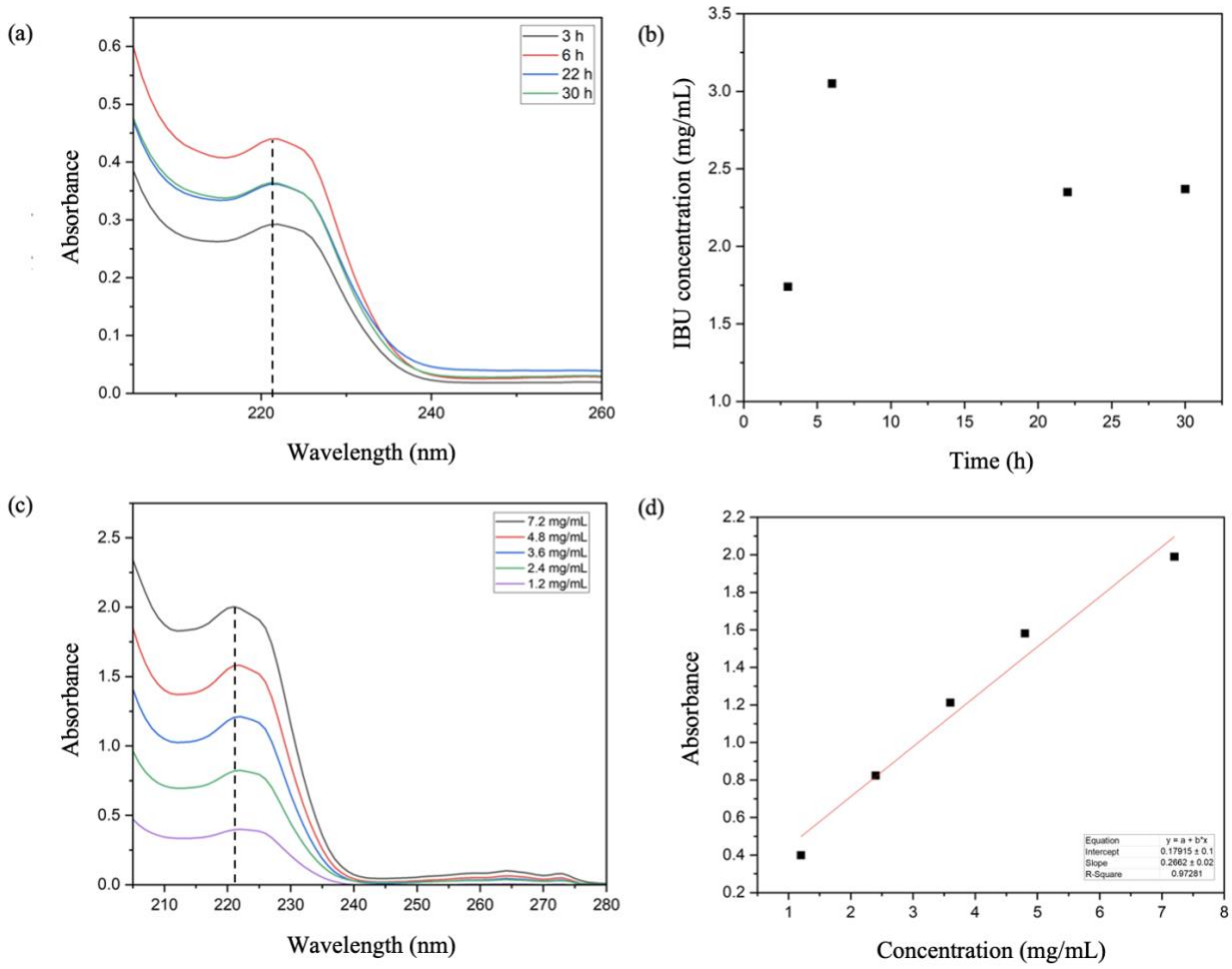

Figure 2.9. IBU release from MIPs-MSNPs-SiNPs; (a) UV-vis spectroscopy data, (b) Correlation to the concentration of IBU in the mixture, (c) UV-vis spectrum of IBU standard solutions in different concentrations, (d) Calibration curve of IBU standard solutions.

2.3.5 IBU Release by the Non-Imprinted Particles

The IBU release experiment was repeated using non-imprinted samples (i.e., NIPs-MSNPs-SiNPs) following the procedure outlined in Section 2.2.6. Figure 2.10a shows the absorbance of representative aliquots of the supernatant at the specified time intervals. The absorbance at 221 nm that corresponds to IBU was used to determine the concentration of the IBU in the mixture using the presented calibration curve and a release curve was plotted (Figure 2.10b).

The concentration of the IBU slightly increased in the first 6 hours, then decreased over time. The adsorption of the IBU into the non-imprinted polymeric network is indicated by the decrease in the concentration of IBU over 30 hours. The desorption capacity of the NIPs-MSNPs-SiNPs was calculated as 1.40 mg/mg (mg of template desorbed per mg of the particles) using a method described in literature.[12,13]

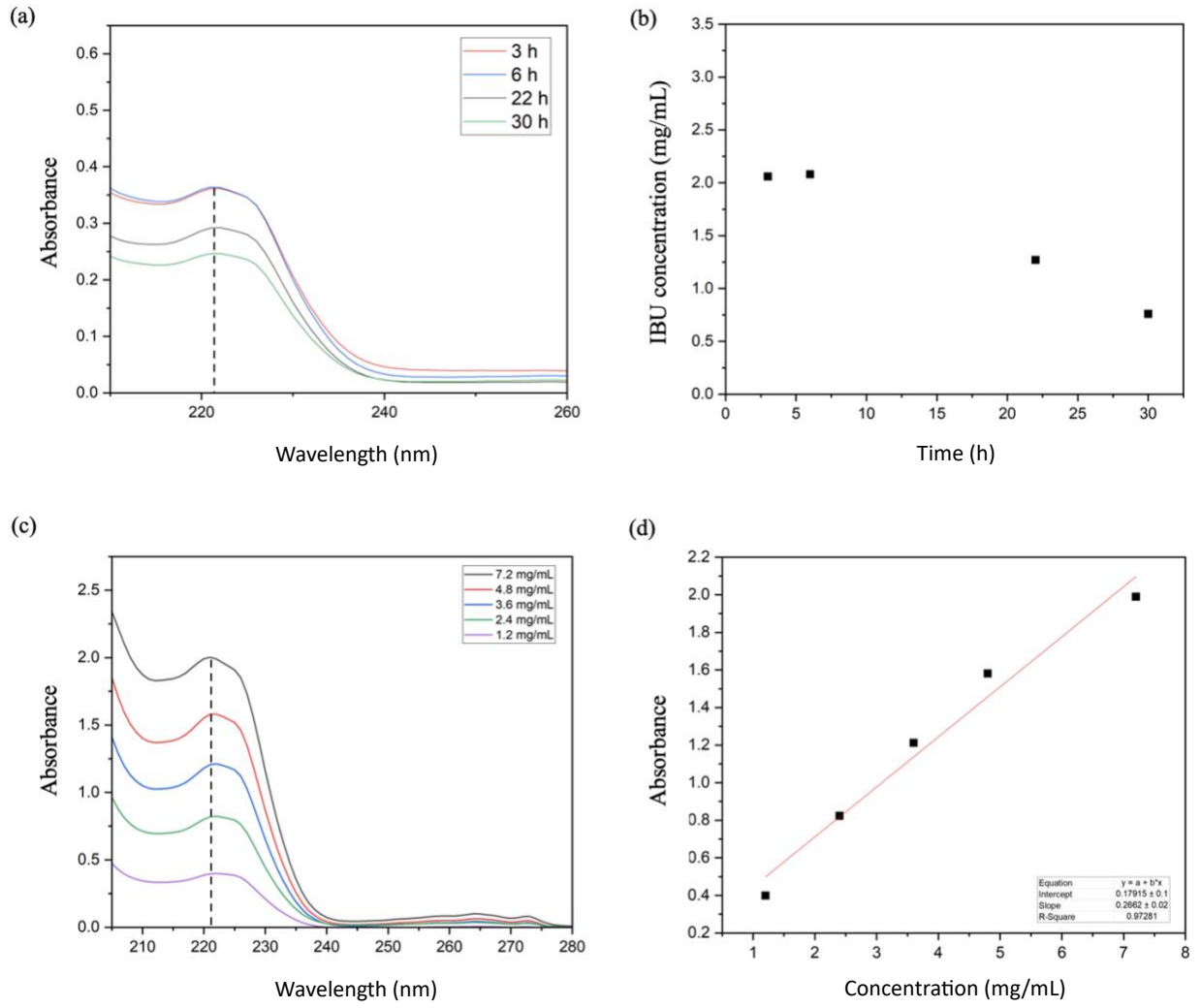

Figure 2.10. IBU release from NIPs-MSNPs-SiNPs; (a) UV-vis spectra, (b) The concentration of IBU in the mixture after release, (c) UV-vis spectra of IBU standard solutions in different concentrations, (d) Calibration curve prepared using the data presented in c.

In summary, the MIPs-MSNPs-SiNPs showed the highest release of the IBU in the first 6 hours, and the NIPs-MSNPs-SiNPs showed a slight release in the first 6 hours, followed by the IBU re-take. Desorption capacity of the MIPs-MSNPs-SiNPs and NIPs-MSNPs-SiNPs was calculated as 2.07 mg/mg and 1.40 mg/mg, respectively. It can be concluded that higher amount of IBU was released by the MIPs-MSNPs-SiNPs compared to NIPs-MSNPs-SiNPs. These results indicate that surface imprinting provided better control over template release compared to non-imprinting.

2.4 Conclusions

In this chapter, the preparation and characterization of SiNPs, MSNPs-SiNPs, MIPs-MSNPs-SiNPs and NIPs-MSNPs-SiNPs are described. SiNPs were prepared via the high temperature processing of HSQ under reducing atmosphere. The SiNPs with pseudospherical shape had an average size of 10.1 ± 1.5 nm. Functional groups on the surfaces of the particles were characterized by FTIR spectroscopy, showing the presence of the characteristic silica vibrations, vinyl functionalization, and characteristic vibrations of the polymer. IBU release experiments were performed using MIPs-MSNPs-SiNPs and NIPs-MSNPs-SiNPs. The results of the release experiments indicated that surface imprinting provided better control over template release compared to non-imprinting. Moreover, the prepared hybrid material that includes the integration of the optical properties of SiNPs, the stability and non-toxicity of MSNPs and the selectivity of MIPs suggests that these materials have potential as a versatile tool in drug delivery applications.

2.5 References

(1) Ji, X.; Wang, H.; Song, B.; Chu, B.; He, Y. Silicon Nanomaterials for Biosensing and Bioimaging Analysis. *Front. Chem.* **2018**, *6*, 1–9.

(2) Park, J. H.; Gu, L.; Von Maltzahn, G.; Ruoslahti, E.; Bhatia, S. N.; Sailor, M. J. Biodegradable Luminescent Porous Silicon Nanoparticles for in Vivo Applications. *Nat. Mater.* **2009**, *8* (4), 331–336.

(3) Hosseinpour, S.; Walsh, L. J.; Xu, C. Biomedical Application of Mesoporous Silica Nanoparticles as Delivery Systems: A Biological Safety Perspective. *J. Mater. Chem. B* **2020**, *8* (43), 9863–9876.

(4) Regli, S.; Kelly, J. A.; Barnes, M. A.; Andrei, C. M.; Veinot, J. G. C. Mesoporous Silica Encapsulation of Silicon Nanocrystals: Synthesis, Aqueous Dispersibility and Drug Release. *Mater. Lett.* **2014**, *115*, 21–24.

(5) Gagliardi, M. Design and Development of Molecularly Imprinted Biodegradable Polymers for Nanomedicine. *Adv. Ind. Eng. Polym. Res.* **2023**, *6* (4), 396–406.

(6) Leibl, N.; Haupt, K.; Gonzato, C.; Duma, L. Molecularly Imprinted Polymers for Chemical Sensing: A Tutorial Review. *Chemosensors* **2021**, *9* (6), 1–19.

(7) Wang, H. Y.; Cao, P. P.; He, Z. Y.; He, X. W.; Li, W. Y.; Li, Y. H.; Zhang, Y. K. Targeted Imaging and Targeted Therapy of Breast Cancer Cells: Via Fluorescent Double Template-Imprinted Polymer Coated Silicon Nanoparticles by an Epitope Approach. *Nanoscale* **2019**, *11* (36), 17018–17030.

(8) Clark, R. J.; Aghajamali, M.; Gonzalez, C. M.; Hadidi, L.; Islam, M. A.; Javadi, M.; Mobarok, M. H.; Purkait, T. K.; Robidillo, C. J. T.; Sinelnikov, R.; Thiessen, A. N.; Washington, J.; Yu, H.; Veinot, J. G. C. From Hydrogen Silsesquioxane to Functionalized Silicon Nanocrystals. *Chem. Mater.* **2017**, *29* (1), 80–89.

(9) Rui, C.; He, J.; Li, Y.; Liang, Y.; You, L.; He, L.; Li, K.; Zhang, S. Selective Extraction and Enrichment of Aflatoxins from Food Samples by Mesoporous Silica FDU-12 Supported Aflatoxins Imprinted Polymers Based on Surface Molecularly Imprinting Technique. *Talanta*, **2019**, pp 342–349.

(10) Baig, M. M.; Yousuf, M. A.; Alsafari, I. A.; Ali, M.; Agboola, P. O.; Shakir, I.; Haider, S.; Warsi, M. F. New Mesostructured Origami Silica Matrix: A Nano-Platform for Highly

Retentive and PH-Controlled Delivery System. *J. Taibah Univ. Sci.* **2021**, *15* (1), 133–144.

(11) Taweekarn, T.; Wongniramaikul, W.; Limsakul, W.; Sriprom, W.; Phawachalotorn, C.; Choodum, A. A Novel Colorimetric Sensor Based on Modified Mesoporous Silica Nanoparticles for Rapid On-Site Detection of Nitrite. *Microchim. Acta* **2020**, *187* (12).

(12) Yu, Q.; Fan, L.; Li, J. A Novel Process for Asparagus Polyphenols Utilization by Ultrasound Assisted Adsorption and Desorption Using Resins. *Ultrason. Sonochem.* **2020**, *63*, 104920.

(13) Zhang, J.; Zhang, J.; Wang, M.; Wang, M.; Peng, W.; Peng, W.; Chen, Z.; Chen, Z.; Chen, Z.; Chen, Z. Glutathione Surface Molecularly Imprinted Polymer from CLX1180 via Three Modes of Polymerization for Selective Adsorption of Glutathione. *ACS Omega* **2020**, *5* (23), 13777–13784.

Chapter 3

Silver Nanoparticles Embedded in Surface Imprinted Silica for Sensing

3.1 Introduction

Silver nanoparticles (AgNPs) have diverse applications (e.g., biosensing, environmental remediation, wound healing, pharmaceuticals, disinfectants, packaging, detergents, plastics) due to their unique physical and chemical properties such as high surface area, high thermal and electrical conductivity, surface Raman scattering, and catalytic activity.[1] The use of AgNPs in biosensing has been broadly studied, however, the toxicity and limited stability of these materials in biological systems has restricted their wide spread application in this field.[2]

Drawing on the well-established encapsulation procedures used to combine porous materials (e.g., mesoporous silica) with nanoparticles, we and others have explored encapsulation as an approach to both reduce the toxicity and increase the stability of AgNPs.[3,4,5] In a specific example, Fathima et al. prepared mesoporous silica-capped silver nanoparticles (Ag@m-SiO_2) via sol-gel synthesis using a long-chain cationic surfactant, dodecyltrimethylammonium bromide (DTAB), and tetraethyl orthosilicate (TEOS) and investigated SERS-based sensing.[5] The mesoporous silica shell of Ag@m-SiO_2 sieves large molecules, thus enabling the sensing of small molecules that penetrate the shell. Another level of selectivity is provided by the negative surface

charge of Ag@m-SiO_2, eliminating negatively charged molecules due to electrostatic repulsion. Despite these advances, challenges remain, and controlling selectivity toward the molecules of interest is of paramount importance as the non-selective pores of mesoporous silica do not discriminate between the molecules of interest and other molecules in the sensing medium. Molecular imprinting is an intriguing approach for producing sensors with the needed selectivity.

Molecularly imprinted polymers (MIPs) exhibit properties close to those of natural receptors in terms of selectivity and can be modified for a wide range of target molecules.[6] Rui et al. demonstrated that MIPs can be prepared using mesoporous silica as a matrix for solid phase extraction of aflatoxins in food samples.[7] While MIPs provide a selective platform to bind molecules of interest, they often need to be paired with a response system as the detection of the target molecules depends on the change in the response system. These response systems can take many forms including electrochemical, gravimetric, or optical.[6] Zhang et al. demonstrated the integration of cadmium telluride (CdTe) quantum dots into the MIPs for the fluorescent detection of a cytochrome c in biological systems by taking advantage of the high selectivity of MIPs and the strong fluorescence of the quantum dots.[8] This study demonstrated the use of quantum dots coated with MIPs for the optical detection of biomolecules; however, possible toxicity of the material in biological systems could limit its implementation.

In this regard, we demonstrate the preparation of AgNPs encapsulated in the surface imprinted mesoporous silica to combine the plasmonic properties of AgNPs with the non-toxicity and large surface area of mesoporous silica, and high selectivity of MIPs. Once in hand, the properties and possible applications of these multifunctional hybrid materials are investigated.

3.2 Experimental

3.2.1 Reagents and Materials

Glycerol (≥99.5%), silver nitrate ($AgNO_3$, ≥99%), trisodium citrate dihydrate, cetyltrimethylammonium bromide (CTAB), tetraethoxysilane (TEOS, ≥99%), vinyltrimethoxysilane (98%), acrylamide (AAm), N-isopropylacrylamide (NIPAM, 97%), N,N′-methylenebisacrylamide (BIS, ≥99.5%), ammonium persulfate (APS), N,N,N′,N′-tetramethyl ethylenediamine (TEMED, 99%), urea (99.0 – 100.5%), sodium hydroxide (NaOH, ≥98%, pellets, anhydrous), ethyl acetate (EtOAc, ≥99.5%), ethanol (EtOH, 95%) were purchased from Sigma-Aldrich. Hydrochloric acid (HCl, 37%, reagent grade) was purchased from ACP Chemicals. Unless otherwise specified, all reagents were used as received.

3.2.2 Preparation of Silver Nanoparticles

Silver nanoparticles were prepared using an adaptation of a literature procedure.[5] Briefly, glycerol (1 mL, 14 mmol) was added to distilled water (150 mL) and the mixture was heated to 95 ˚C. $AgNO_3$ (60 mg, 0.4 mmol) and trisodium citrate dihydrate (80 mg, 0.3 mmol in 6 mL water) were added to the heated glycerol solution, respectively. The hot reaction mixture was vigorously stirred under constant heating for 30 min. The presence of green/brown colloidal suspension indicated the formation of AgNPs. The precipitate was collected by centrifuging once at 5000 rpm for 20 minutes. The precipitate was resuspended in distilled water (10 mL) via sonication and purified by three cycles of centrifuging/resuspension at 5000 rpm for 20 minutes/cycle using distilled water (10 mL). The AgNPs were resuspended in 50 mL distilled water. This stock suspension was stored in subdued light in a glass vial until needed. The concentration of the AgNPs

were calculated as 8.61×10^{-10} M. AgNPs were characterized using scanning electron microscopy (SEM), dynamic light scattering (DLS), and UV-visible (UV-vis) spectroscopy.

3.2.3 Encapsulation of Silver Nanoparticles in Mesoporous Silica

Mesoporous silica encapsulated silver nanoparticles (MSNPs-AgNPs) were synthesized using a variation of a procedure developed in our laboratory.[9] AgNPs (0.5 mL of the stock suspension prepared in Section 3.2.2) were added dropwise to a solution of CTAB (5 mL in water, 55 mM) with stirring. After the addition was complete, the mixture was heated to 50 ˚C and stirred for 30 min. Solutions of NaOH (45 mL, 13 mM, pre-heated to 50 ˚C), TEOS (0.5 mL, 2 mmol) and EtOAc (3 mL, 30 mmol) were prepared separately and added into the mixture sequentially. The mixture was stirred for 3 h. The formation of a cloudy white suspension indicated the formation of MSNPs. The precipitate was collected by centrifuging once at 11400 rpm for 20 minutes. Then, the precipitate was suspended in EtOH:H_2O (v:v; 1:1) via sonication and purified by three cycles of centrifuging/resuspension at 11400 rpm for 20 minutes/cycle using EtOH:H_2O (v:v; 1:1) mixture to remove excess reagents and surface bonded CTAB. The particles obtained were transferred into a glass vial and suspended in EtOH (20 mL) for further use.

CTAB inside the pores of MSNPs was removed by adding HCl (0.1 M, 40 μL) to the MSNPs-AgNPs in EtOH (20 mL) and the mixture was heated to 70 ˚C. It was stirred vigorously for 24 h at 70 ˚C, followed by cooling to room temperature. The precipitate was collected by centrifuging once at 11400 rpm for 20 minutes. The precipitate was resuspended in EtOH:H_2O (v:v; 1:1) via sonication and purified by three cycles of centrifuging/resuspension at 11400 rpm for 20 minutes/cycle using EtOH:H_2O (v:v; 1:1) mixture. The precipitate was collected and resuspended in EtOH (20 mL) and stored in a glass vial until further use.

To investigate the position of the AgNPs in the MSNPs-AgNPs, reaction parameters were modified. The parameters that were modified was divided into two categories: "during synthesis" and "post synthesis" procedures. The parameters that were modified in "during synthesis" procedure was the concentrations of CTAB and AgNPs (qualitatively). Parameters that were changed in "post synthesis" procedure was the CTAB removal method. The reaction parameters are given in Table 3.1.

Modification number	**During synthesis**			**Post synthesis**
	CTAB concentration (mM)	**Volume of AgNPs (mL)**	**CTAB and AgNPs mixing time (min)**	**CTAB removal method**
1	55	0.5	30	Dialysis
2	75	0.5	30	Dialysis
3	75	1	30	Dialysis
4	55	1	30	Reflux with EtOH and HCl
5	55	0.5	30	Reflux with EtOH and HCl

Table 3.1. Reaction parameters in "during synthesis" and "post synthesis" procedures.

The MSNPs-AgNPs were characterized using scanning electron microscopy (SEM), energy-dispersive X-ray (EDX) spectroscopy, Fourier-transform infrared (FTIR) spectroscopy, thermogravimetric analysis (TGA), dynamic light scattering (DLS), and zeta potential analyzer.

3.2.4 Surface functionalization

Alkene groups were introduced to the surface of MSNPs-AgNPs to make the surface available for molecular imprinting.[7] Vinyltrimethyoxysilane (0.5 mL, 3 mmol) was added to a

suspension of MSNPs-AgNPs (prepared in Section 3.2.3) in EtOH:H_2O (v:v; 1:1) and it was stirred for 24 h at 50 ˚C. The precipitate was collected by centrifuging once at 11400 rpm for 20 minutes. The precipitate was resuspended in EtOH:H_2O (v:v; 1:1) via sonication and purified by three cycles of centrifuging/resuspension at 11400 rpm for 20 minutes/cycle using EtOH:H_2O (v:v; 1:1) mixture. The pellet was collected and resuspended in EtOH (10 mL). The surface functionalized MSNPs-AgNPs were characterized using Fourier-transform infrared (FTIR) spectroscopy, and thermogravimetric analysis (TGA).

3.2.5 Molecular Imprinting

Surface molecular imprinting of the vinyl functionalized MSNPs-AgNPs (vinyl-MSNPs-AgNPs) was achieved by coating the surface with poly(N-isopropylacrylamide-co-acrylamide).[7] surface polymerization of MSNPs was achieved using AAm (11.5 mg, 0.2 mmol) and NIPAm (19.5 mg, 0.2 mmol) as monomers, BIS (20 mg, 0.1 mmol) as a crosslinker, APS (60 mg, 0.3 mmol in 1 mL water) and TEMED (100 μL, 0.7 mmol) as initiators, and urea (15 mg, 0.2 mmol) as a template. The vinyl-MSNPs-AgNPs (prepared in Section 3.2.4) were dispersed in 20 mL EtOH:H_2O (v:v; 1:1) with exposure to a bath sonicator and the dispersion was transferred into a 50 mL round bottom flask. The dispersion had a light brown appearance. The monomers, crosslinker and template were added sequentially to the reaction flask while stirring. The mixture was stirred for 3 h at room temperature to thoroughly mix the monomers, crosslinker and template. Subsequently, the initiators were added and the mixture was stirred for an additional 24 h at room temperature after which, no obvious colour change was observed. The precipitate was collected by centrifuging once at 5000 rpm for 20 minutes. Then, it was resuspended in EtOH:H_2O (v:v; 1:1) via sonication and purified by five cycles of centrifuging/resuspension at 5000 rpm for 20

minutes/cycle using EtOH:H_2O (v:v; 1:1) mixture to remove unreacted monomers, excess reagents, and surface bonded templates. The purified particles were suspended in EtOH (25 mL) for further use.

To remove the template molecules, the surface molecularly imprinted MSNPs-AgNPs (MIPs-MSNPs-AgNPs) in EtOH (25 mL) were refluxed for 12 h. The precipitate was collected by centrifuging once at 5000 rpm for 20 minutes. Then, it was resuspended in EtOH:H_2O (v:v; 1:1) via sonication and purified by five cycles of centrifuging/resuspension at 5000 rpm for 20 minutes/cycle using EtOH:H_2O (v:v; 1:1) mixture to remove the extracted templates. MIPs-MSNPs-AgNPs were dried under vacuum and stored in a glass vial for further use. The MIPs-MSNPs-AgNPs were characterized by scanning electron microscopy (SEM), fourier-transform infrared (FTIR) spectroscopy, thermogravimetric analysis (TGA), dynamic light scattering (DLS), and zeta potential analyzer. The identical procedure (except the template addition during polymerization) was used to produce the MSNPs-AgNPs with the nonimprinted polymer on the surface (NIPs-MSNPs-AgNPs).

3.2.6 Template Uptake and Release

After removing the template as described on Section 3.2.5, the dried MIPs-MSNPs-AgNPs (15 mg) were added to a test tube. Subsequently, 10 mL of urea (5 mg/mL) solution in EtOH:H_2O (v:v; 1:1) were added and the mixture was sonicated briefly to suspend the particles. At predetermined time intervals, the mixture was centrifuged for 5 minutes at 5000 rpm and 100 μL of the supernatant was extracted into a vial. Distilled water was added into the vial until the volume reached to 5 mL. Two or three replicates of the samples were prepared. The solutions were analysed using UV-vis spectroscopy monitoring the absorption wavelength at 203 nm. The objective of this

study was to determine the quantity of urea taken up by the MIPs-MSNPs-AgNPs. The identical procedure was performed using the NIPs-MSNPs-AgNPs. The extracted amount of the template is calculated indirectly by determining how much template is left in solution.

To evaluate template release, template removed MIPs-MSNPs-AgNPs were first loaded with urea. To do this, vacuum dried MIPs-MSNPs-AgNPs (15 mg, without the template) was suspended in 10 mL of EtOH:H_2O (v:v; 1:1) via sonication. Urea (5 mg/mL) in EtOH:H_2O (v:v; 1:1) was added to the MIPs-MSNPs-AgNPs. The mixture was stirred for 24 h at room temperature. The loaded particles were collected by centrifuging at 5000 rpm for 20 minutes. The loaded particles that remained as the precipitate were then resuspended in EtOH:H_2O (v:v; 1:1) via sonication and purified by three cycles of centrifuging/resuspension at 5000 rpm for 20 minutes/cycle using EtOH:H_2O (v:v; 1:1) to remove excess template. They were transferred to a clean test tube and 10 mL of phosphate buffer (0.1 M, pH=7.4) was added. The particles were suspended in phosphate buffer via sonicating briefly. The mixture was centrifuged for 5 minutes at 5000 rpm at predetermined time intervals. Then, 100 μL of the supernatant was extracted from the test tube into a vial and diluted to 5 mL with distilled water. Two or three replicates of the samples were prepared. The solutions were analysed using UV-vis spectroscopy monitoring the absorption wavelength at 203 nm. The objective of this study was to determine the quantity of urea that was released by the MIPs-MSNPs-AgNPs. The identical procedure was performed using the NIPs-MSNPs-AgNPs. Standard solutions were prepared with 1, 2, 3, 4, 5, 6, and 7 mg/mL of urea using serial dilution method from a 10 mg/mL urea stock solution. The UV-vis spectra of the standards were recorded and a calibration curve was obtained.

3.2.7 Material Characterization and Instrumentation

Fourier-transform infrared (FTIR) spectra were acquired using a Thermo Nicolet 8700 FTIR Spectrometer. Powder samples (~1-3 mg of sample per ~250 mg KBr) prepared as potassium bromide pellets for the measurement. Scanning electron microscopy (SEM) images was obtained using Zeiss Sigma Field Emission equipped with a Bruker energy dispersive X-ray spectroscopy (EDX) with dual silicon drift detectors each with an area of 60 mm^2 and a resolution of 123 eV. The size distribution analyses were done using ImageJ software and at least 300 particles (except Section 3.3.1) were measured to obtain the average-shifted histograms for the size distributions. Thermogravimetric analysis (TGA) data was obtained using Perkin Elmer Pyris 1 Thermogravimetric Analyzer with a heating rate of 5 ˚C/min in an argon atmosphere. Dynamic light scattering (DLS) and zeta potential data was obtained using a Malvern Zetasizer Nano S series with a 633 nm laser. Dilute samples were prepared in EtOH:H_2O (1:1) and filtered through a 0.45-μ PTFE syringe filter to remove the large agglomerates. The samples were scanned three times. A Hewlett Packard 8453 UV-vis Spectrophotometer was used to obtain UV-vis data. Quartz cuvette was used.

3.3 Results and Discussion

The preparation of MIPs-MSNPs-AgNPs allows the formation of a multifunctional hybrid material that combines the advantages of each constituent - the optical properties of AgNPs, nontoxicity and large surface area of mesoporous silica, and selectivity of MIPs. In present study, the synthesis and characterization of one such hybrid were explored.

3.3.1 Silver Nanoparticles

AgNPs were prepared using a straightforward solution-phase chemical reduction method. Scheme 3.1 illustrates the formation of the AgNPs via the reduction of Ag^+ ions by trisodium citrate that also acts as a stabilizing agent. The colour of the mixture changed from clear colourless to cloudy green/brown consistent with the formation of the AgNPs.

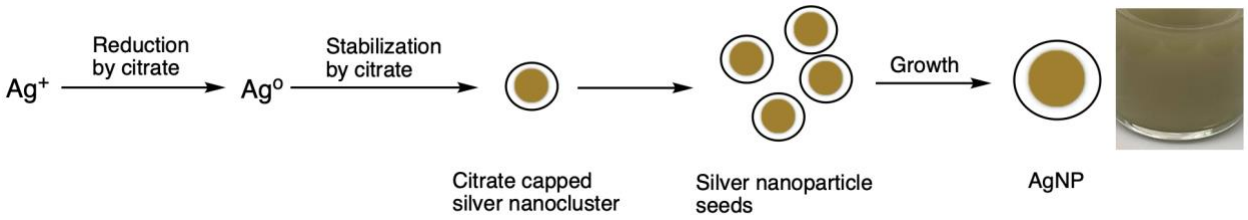

Scheme 3.1. The formation of AgNPs via the reduction of Ag^+ ions by trisodium citrate.

Secondary electron scanning electron microscopy was used to determine the size and morphology of the AgNPs (Figure 3.1a and Figure 3.1b). The AgNPs exhibit a pseudospherical shape with an average diameter of 45.7 ± 6.3 nm (Figure 3.1c) with a bimodal distribution in the associated average-shifted. Although it is ideal to evaluate at least 300 particles to ensure statistically relevant data, only 200 particles could be measured here due to the extremely agglomerated nature of the samples.[10] UV-vis spectroscopy was used to complement the SEM imaging because the optical properties of the AgNPs are highly dependent on particle dimensions. While smaller AgNPs primarily absorb light near 400 nm, larger ones exhibit increased scattering and have peaks that broaden and shift to longer wavelengths. Figure 3.1d shows a representative UV-vis spectrum of the AgNPs in distilled water. The AgNPs showed an absorption maximum at 405 nm which corresponds to an average size of 45 nm and consistent with the size data obtained from the SEM image.[11]

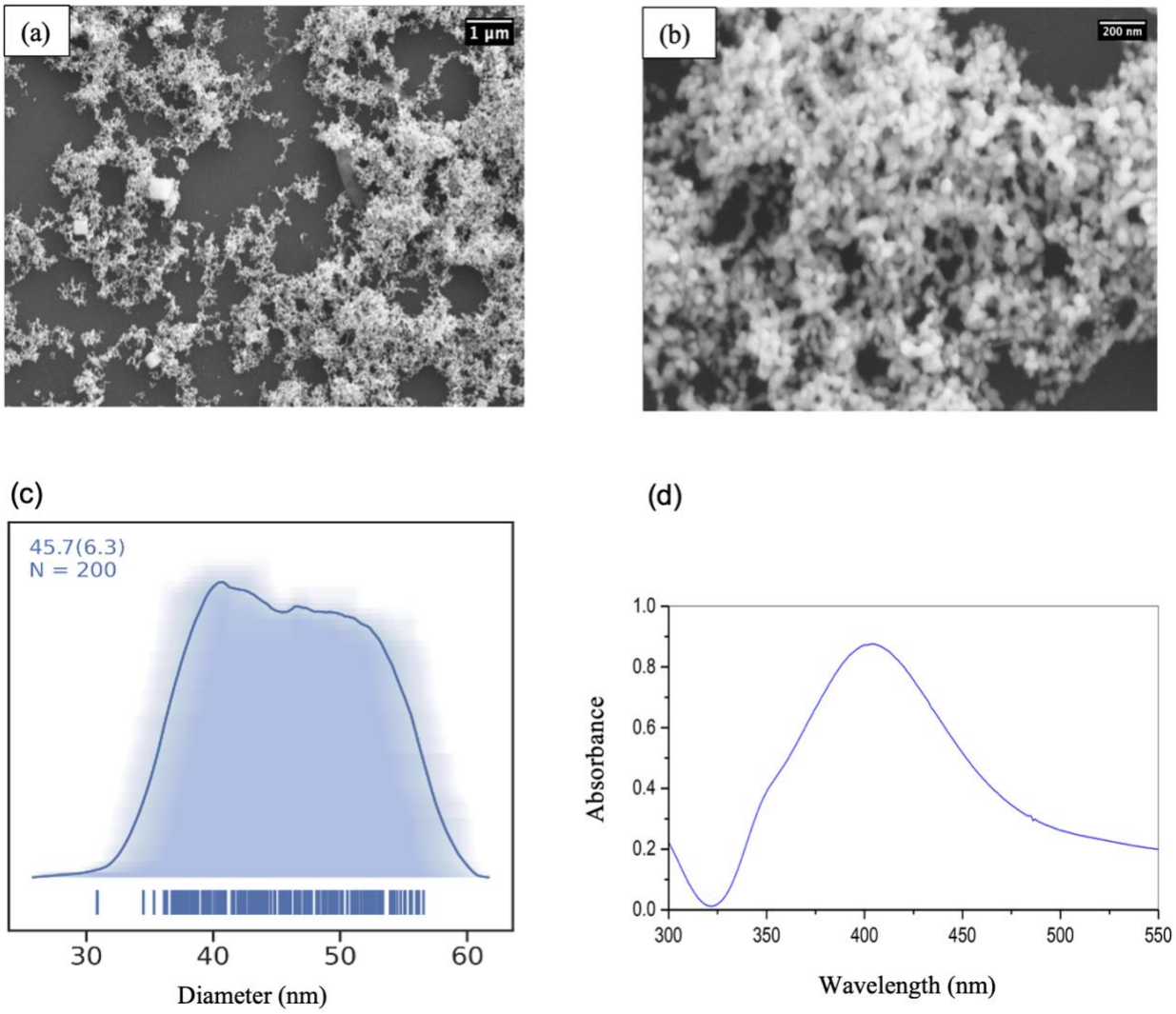

Figure 3.1. (a), (b) Secondary electron SEM images of AgNPs, (c) Average shifted histogram of AgNPs, (d) UV-vis spectrum of AgNPs.

DLS was also used to determine the size distribution profile of the particles in suspension and showed a hydrodynamic diameter of 122 nm (Figure 3.2). The hydrodynamic diameter of the AgNPs is larger than the physical diameter of the particles measured by electron microscopy because it reflects the size of the particles when in solution and includes coatings, surface modifications, and a solvation sphere.

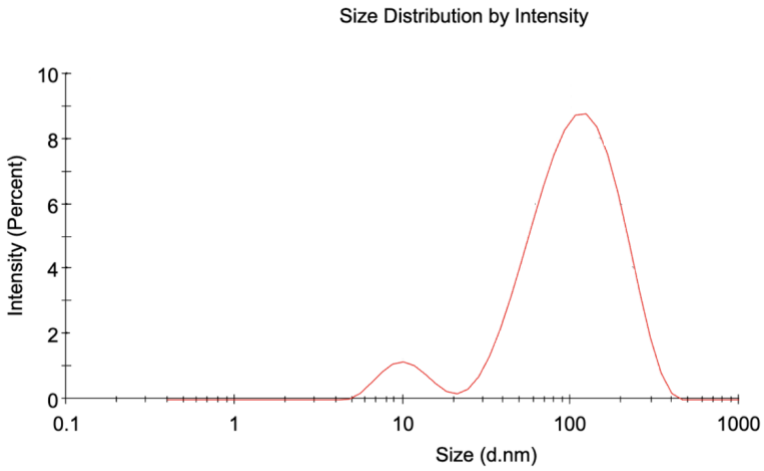

Figure 3.2. DLS size distribution of AgNPs in water.

3.3.2 Mesoporous Silica Encapsulation of Silver Nanoparticles

We attempted to deposit mesoporous silica onto the surface of AgNPs as described in Section 3.3.1. An aqueous suspension of AgNPs was added dropwise to a solution of CTAB (5 mL, 55 mM) in water with vigorous stirring. After the addition was complete, the mixture was heated to 50 ˚C and stirred for 30 min. Solutions of NaOH (45 mL, 13 mM, pre-heated to 50 ˚C), TEOS (0.5 mL, 2 mmol) and EtOAc (3 mL, 30 mmol) were prepared separately and added into the mixture sequentially, and the mixture was stirred for 3 h. The formation of a cloudy white suspension indicated the formation of the MSNPs-AgNPs (Scheme 3.2).

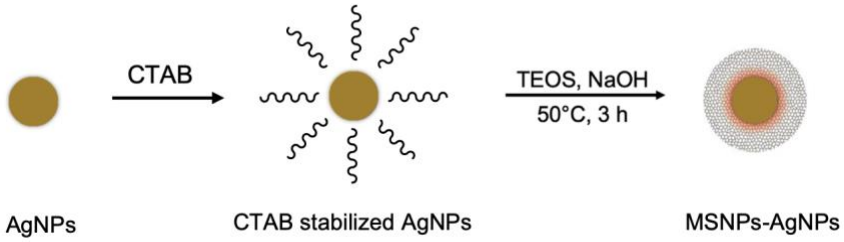

Scheme 3.2. Schematic representation of the synthesis of MSNPs-AgNPs.

Secondary electron SEM images of the isolated product were dominated by particles with dimensions of 128 ± 20 nm and showed no evidence of freestanding silver particles (Figure 3.3a). The composition of the particles was evaluated using energy-dispersive X-ray (EDX) spectroscopy which did not detect silver in the isolated product. Surprisingly, the characteristic green/brown colour of the AgNPs remained, suggesting AgNPs are present (Figure 3.3b).

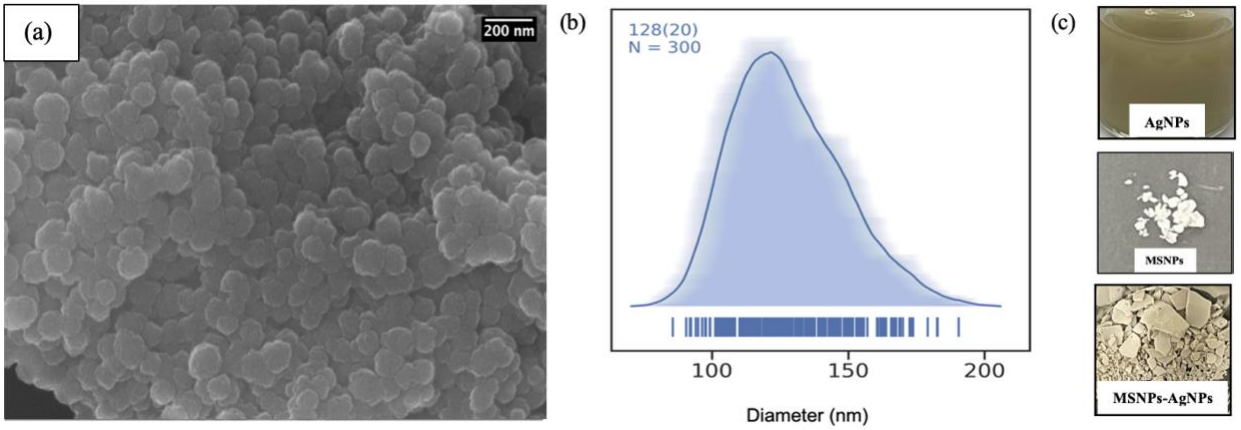

Figure 3.3. (a) SEM image of MSNPs-AgNPs. (b) Average shifted histogram of MSNPs-AgNPs. (c) Photographs of AgNPs, MSNPs, and MSNPs-AgNPs.

To investigate the AgNPs in the MSNPs-AgNPs, reaction parameters were modified. The influence of the concentrations of CTAB and AgNPs, as well as the method of CTAB were investigated. The parameters that were changed were classified into two categories: "during synthesis" and "post synthesis". Parameters that were changed in the "during synthesis" procedure include the concentrations of CTAB and AgNPs. The parameters that were changed "post synthesis" was the CTAB removal method. The reaction parameters are given in Table 3.1 in Section 3.2.3.

It is anticipated that the surface of AgNPs is negatively charged due to the presence of citrate ions (Scheme 3.3). Micelle formation occurs when CTAB is added to the mixture. The ordering of micelle assemblies is influenced by the concentration of surfactants, with a higher

concentration leading to increased ordering.[12] When CTAB is introduced to the solution, a bilayer structure forms around the AgNPs. Subsequently, the TEOS sol-gel precursor will fill the space around micelles by forming cross-linked silica network. After the CTAB template is removed, a porous silica shell remains that encapsulates the NP. After discovering our EDX analysis showed silver was not present, we hypothesized that the AgNPs are not stabilized against by the surfactant coating; as a result, they are not coated by silica. To investigate if the CTAB concentration could increase stability of the AgNPs, it was increased from 55 mM to 75 mM without changing other parameters. Still, silver was below the detection limit, and it was not detected via EDX spectroscopy.

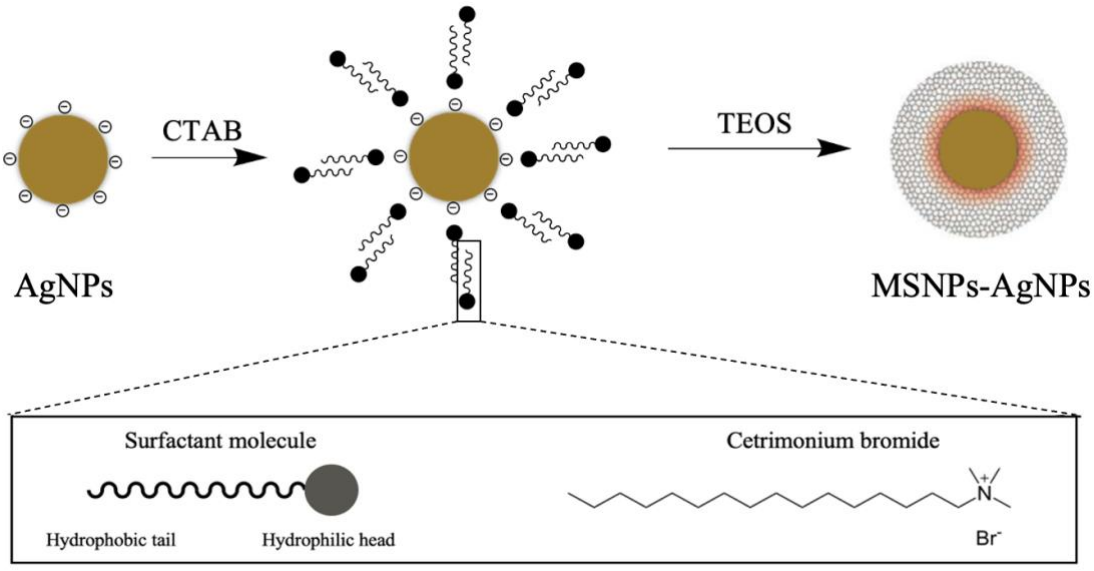

Scheme 3.3. Schematic representation of the formation of MSNPs-AgNPs. The structure of the surfactant molecule, CTAB.

Finding that changing the CTAB concentration did not lead to AgNP incorporation/coating, we turned our attention to the amount AgNPs in the reaction mixture. The concentration of the AgNPs was estimated to be 8.61×10^{-10} M using an established literature method.[13] The details of this calculation can be found in the Appendix. We increased the AgNP concentration added to the

CTAB solution increased from 0.5 mL to 1 mL. Elemental analysis based on EDX spectroscopy still did not show the presence of silver in this sample.

During the procedural investigations noted above, CTAB was removed via dialysis (8-10 kDa cellulose ester against distilled water for 72 h) after synthesis. To investigate the role of this purification method on AgNPs, we evaluated an alternative method for removing CTAB – refluxing the crude product in EtOH (20 mL) and HCl (0.1 M, 40 μL) mixture while leaving the amount of AgNPs constant and adjusting CTAB concentration to 55 mM. EDX analysis showed the presence of silver at the bright spots shown in Figures 3.4 a and b. The presence of silver was observed at 3 keV by EDX analysis at the bright spots (Figure 3.4c). However, EDX analysis at the dark regions of the sample did not show the presence of silver. Therefore, elemental analysis based on EDX spectroscopy suggested that silver was not uniformly distributed throughout the sample. To overcome this, optimizations on the ratio of CTAB:AgNPs were made in the "during synthesis" procedure. The amount of AgNPs used were lowered, keeping all other parameters constant.

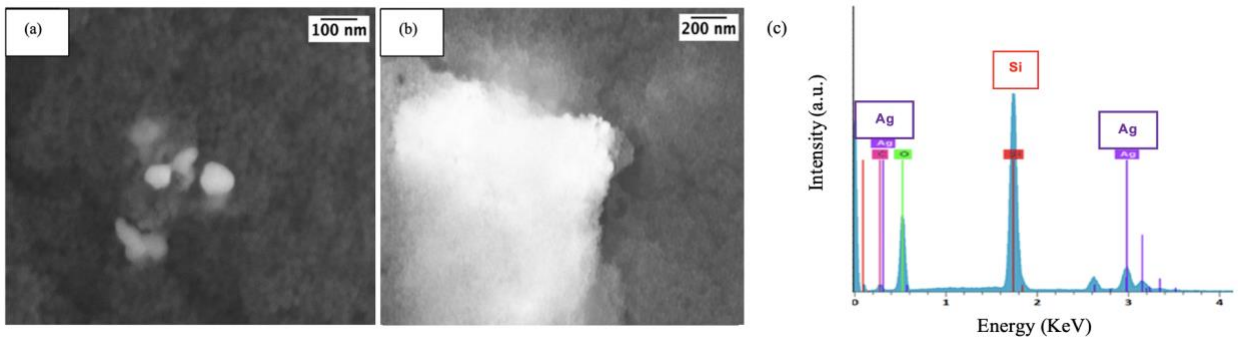

Figure 3.4. (a), (b) Secondary electron SEM image of MSNPs-AgNPs. (c) EDX spectrum of MSNPs-AgNPs at the bright spots.

Secondary electron SEM images of MSNPs-AgNPs showed improvement in terms of morphology and distribution of AgNPs, as well as the spherical shape and the porous surface of

the hybrid material synthesized (Figure 3.5 a, b, c). The average size of the particles is measured as 107 ± 10 nm (see average-shifted histogram in Figure 3.5d). EDX spectroscopy did not reveal the presence of silver.

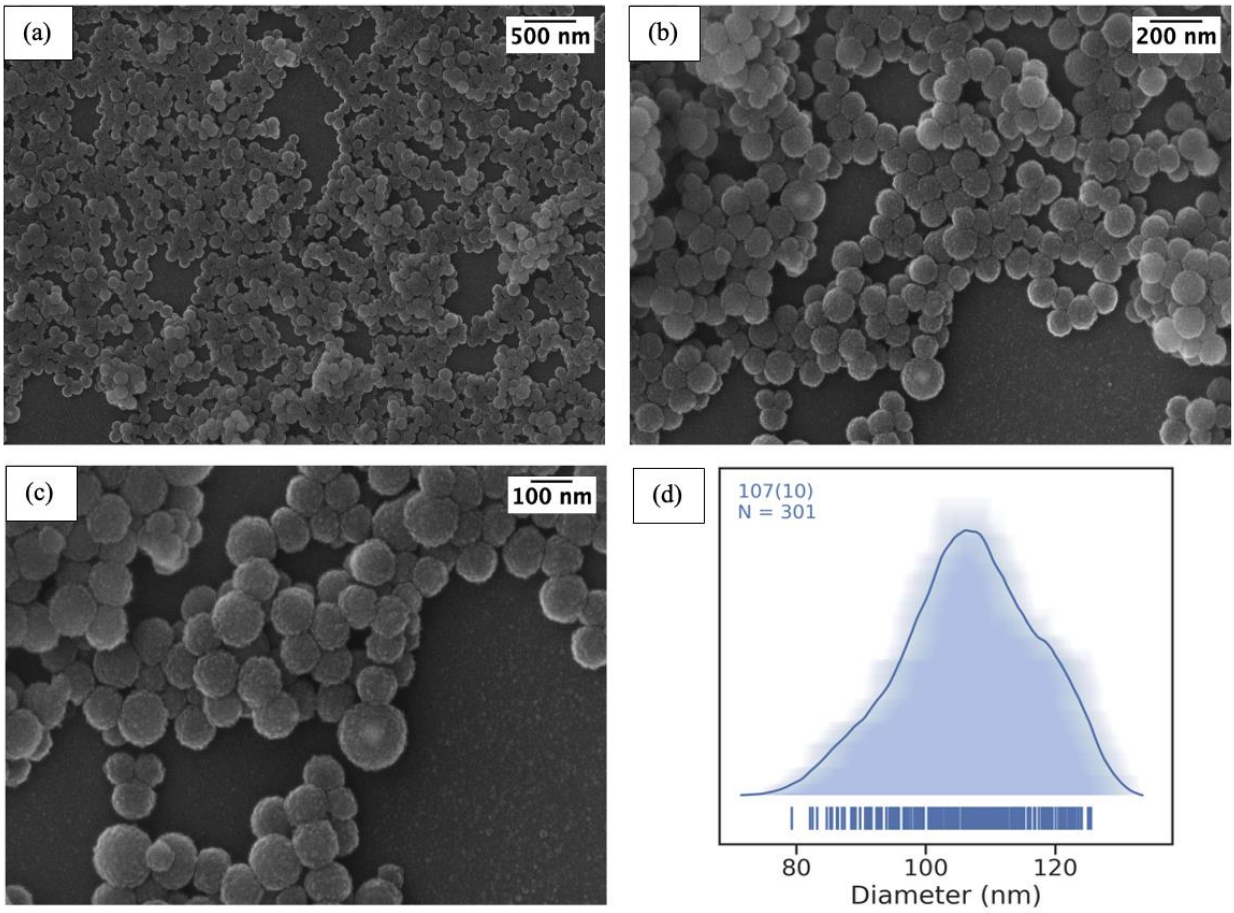

Figure 3.5. (a), (b) and (c) Secondary electron SEM images of MSNPs-AgNPs. (d) Average shifted histogram of MSNPs-AgNPs.

Backscattered electron imaging was used to gain further insight into the structure of the present nanomaterials. The contrast observed in the backscattered electron image is greatly influenced by the atomic number (Z) of the material being examined.[14] Materials containing elements with higher Z such as silver generate more backscattered electrons and appear brighter than materials with lower atomic numbers (e.g., SiO_2). SEM images of the MSNPs-AgNPs with

BSD (Figure 3.6) show bright spots consistent with presence of AgNPs embedded in mesoporous silica. However, only a small amount of AgNPs were detected inside the mesoporous silica.

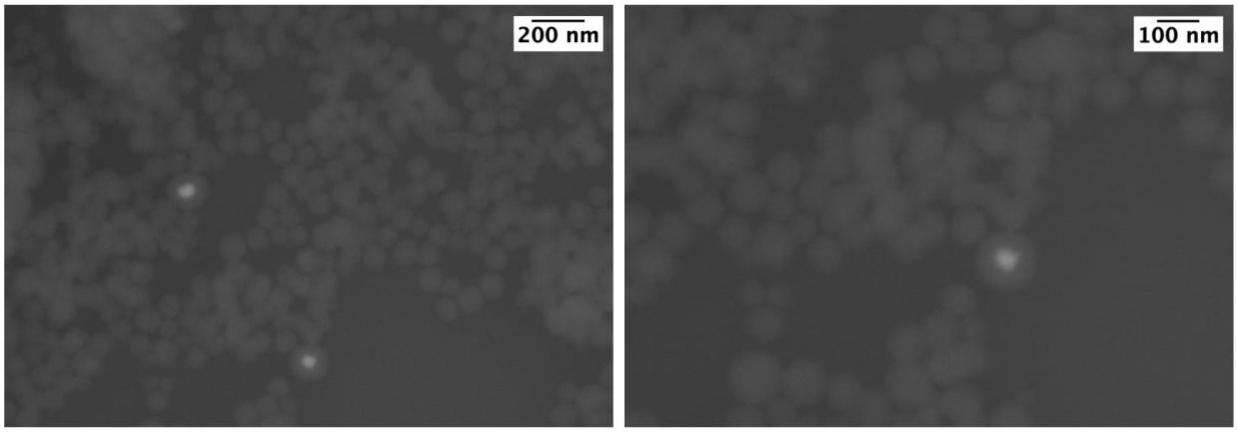

Figure 3.6. SEM/BSD images of MSNPs-AgNPs. Bright spots indicate the AgNPs embedded in MSNPs.

To further identify the presence of AgNPs in the sample, SEM imaging was performed using an in-lens secondary electron detector was used (Figure 3.7). The in-lens detector is located inside the column of the microscope in the beam path and provides efficient collection of secondary electrons, leading to high contrast images even at low voltages. Also, in-lens detector images provide information based on electronic variations (i.e., work function) in the sample as well as morphology and topography as opposed to a standard secondary electron detector where the topographic information is dominant.[15] Since the isolated product was a hybrid material, more conductive AgNPs are expected to appear with brighter contrast than the mesoporous silica component. SEM images with the in-lens secondary electron detector of the MSNPs-AgNPs showed bright regions around the silica which suggested the presence of AgNPs on the surface of mesoporous silica.

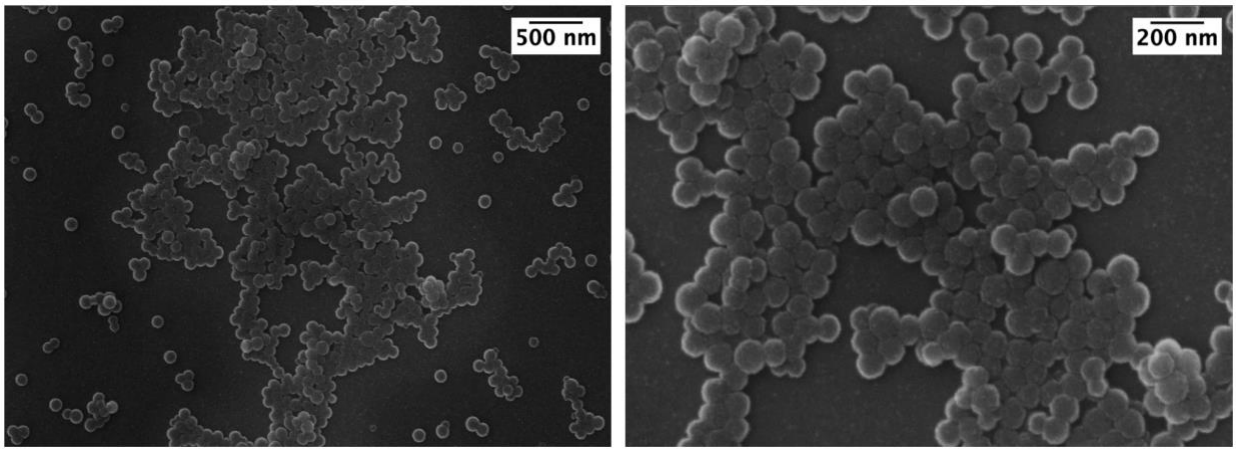

Figure 3.7. SEM/in-lens secondary electron detector images of MSNPs-AgNPs. Bright regions around the particles suggest the presence of AgNPs.

To conclude, AgNPs were not observed in mesoporous silica based on SEM/EDX analysis. Modifications based on "during" and "post" synthesis were performed to be able to characterize AgNPs and it was observed that they were deposited on the surface of the mesoporous silica. After SEM characterization, MSNPs-AgNPs were used to prepare the hybrid material coated with MIPs to provide selectivity for target molecules in sensing applications.

3.3.3 Surface Molecularly Imprinting on Silica

Alkene groups were introduced to the surface of MSNPs-AgNPs via reaction with vinyltrimethyoxysilane to make the surface available for attachment of a polymer that could be molecularly imprinted. The presence of surface vinyl groups on the MSNPs-AgNPs was confirmed using FTIR spectroscopy (Figure 3.10 in page 23). Surface molecular imprinting of vinyl-MSNPs-AgNPs was achieved by coating the surface with poly(N-isopropylacrylamide-co-acrylamide) via radical-initiated polymerization of AAm and NIPAm monomers. Urea was used as the template.

Internally incorporated templates were removed by refluxing the MIPs- MSNPs-AgNPs in ethanol. The preparation of MIPs-MSNPs-AgNPs is summarized in Figure 3.8.

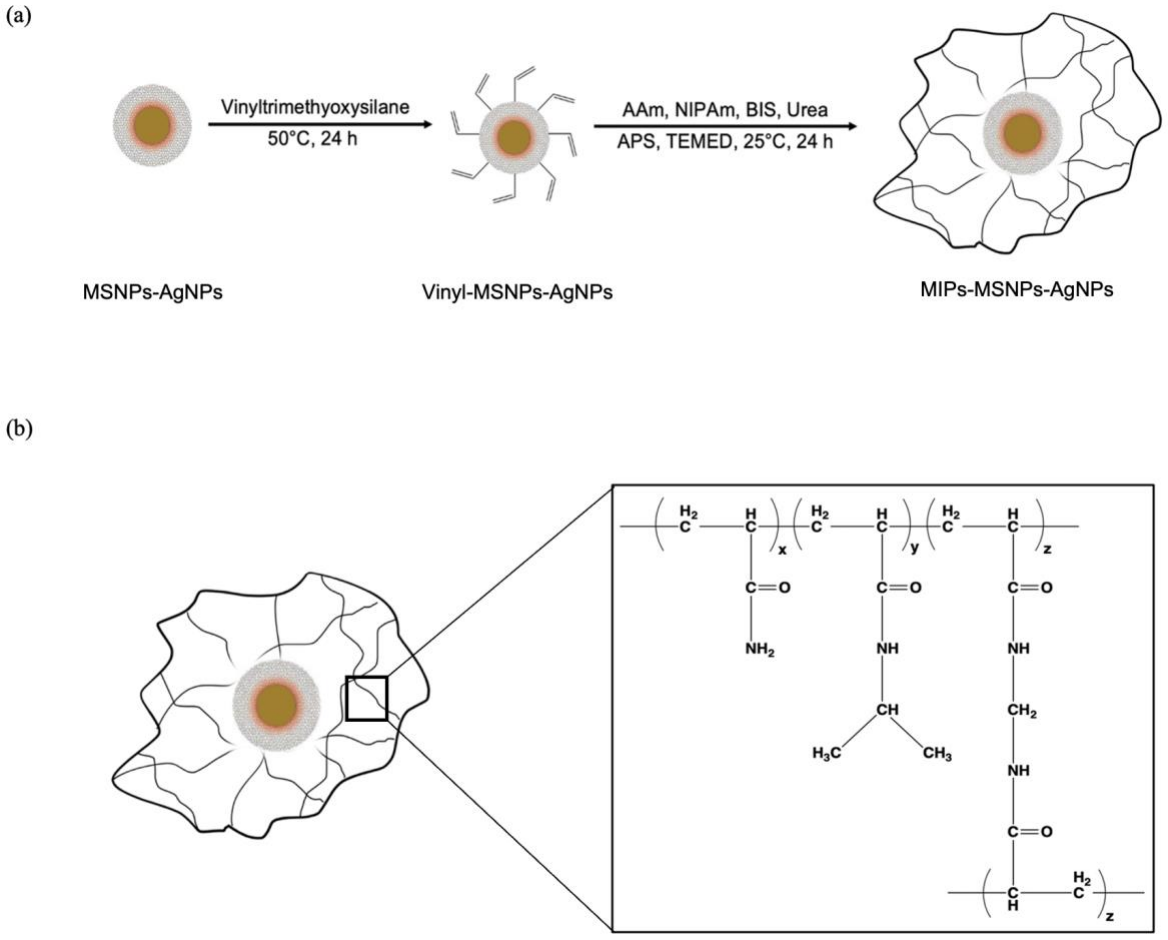

Figure 3.8. (a) The surface functionalization and surface imprinting of the MSNPs-AgNPs and (b) molecular structure of PNIPAm-co-PAAm copolymer.

Secondary electron SEM images of MIPs-MSNPs-AgNPs are shown in Figure 3.9. When compared to the SEM images of the MSNPs-AgNPs (Figure 3.5), we note that the MIPs-MSNPs-AgNPs are highly agglomerated (Figure 3.9a). Higher magnification images (Figure 3.9b and c) showed the presence of the particles were no longer well-defined spheres and showed somewhat random shapes consisting with the presence of a polymer coating. While Figure 3.9d showed high number of coated nanoparticles, it also revealed a region indicated by a red square where the

coating appeared different. The particles in this region changed after exposure to the electron beam during the SEM measurement and this may be the result of thermo responsive property of PNIPAm-co-PAAm copolymer coating. PNIPAm-co-PAAm copolymer is a thermo responsive polymer with lower critical solution temperature (LCST) of 32 ± 10 °C.[16] It is soluble in water, however, upon heating the solution over the LCST, a phase transition occurs. This transition leads to the conversion of the soluble hydrated form of the polymer into an insoluble dehydrated state. While it is not straightforward to confirm in the electron microscopy, we hypothesize that exposure to an electron beam during SEM imaging created localized heating which resulted in the formation of a more compact polymer network that is more insulating compared to the soluble form.

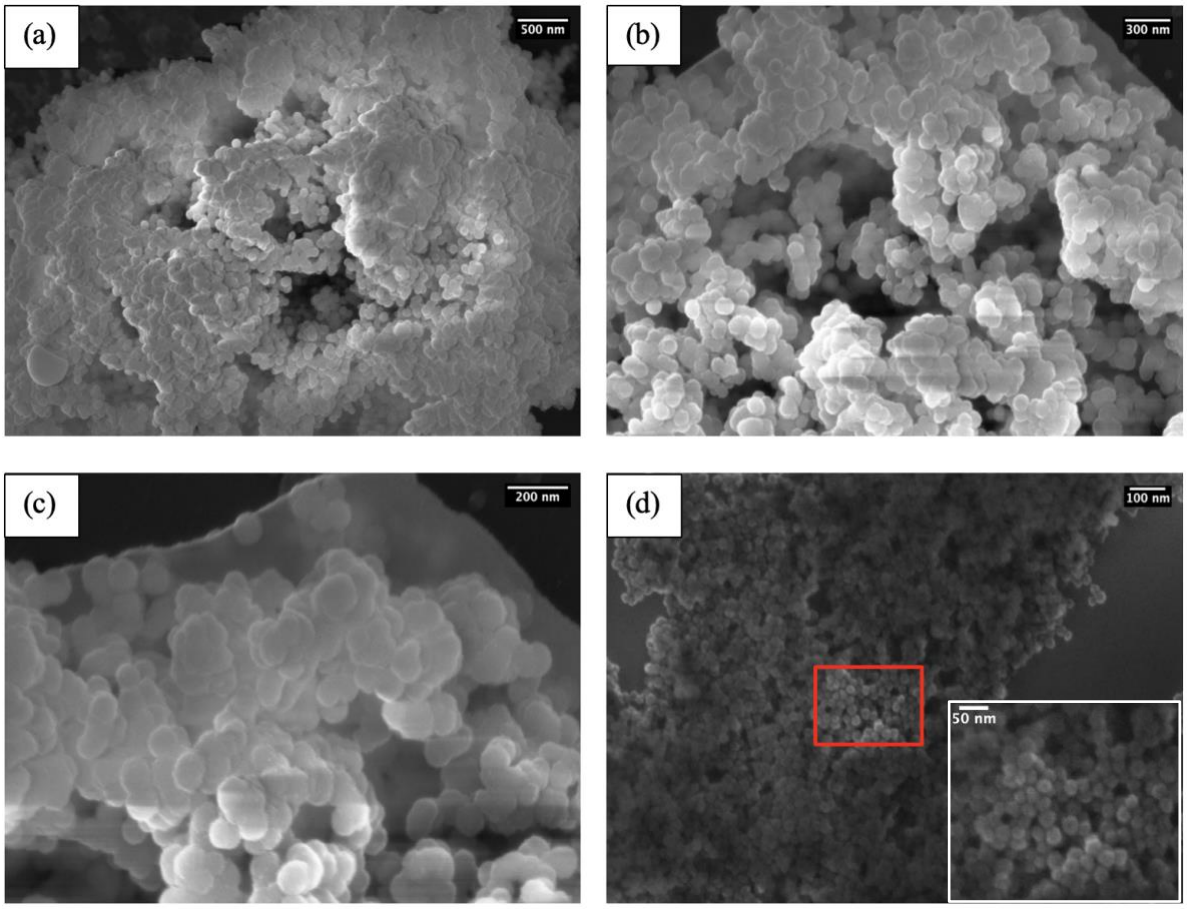

Figure 3.9. (a, b and c) SEM images of AgNPs-MSNPs with PNIPAm-co-PAAm copolymer with different magnifications. (d) SEM image of AgNPs-MSNPs with PNIPAm-co-PAAm copolymer, red box shows the region where charging occurs. Inset shows the higher magnification image of the region indicated by the red box.

We now turn our attention to the surface chemistry of the present materials. FTIR provides identification of chemical bonds and the corresponding functional groups on/within the presented hybrid materials. FTIR spectra of the MSNPs-AgNPs (blue trace), vinyl-MSNPs-AgNPs (red trace) and MIPs-MSNPs-AgNPs (black trace) are shown in Figure 3.10. The peaks at 3400 cm^{-1}, 1100 cm^{-1}, 962 cm^{-1} and 796 cm^{-1} are attributed to characteristic silica vibrations: Si-O-H stretching, asymmetric stretching vibration of Si-O-Si, Si-O-H bending and symmetric stretching vibration of Si-O-Si, respectively.[17,18] Multiple peaks related to C-H stretching vibrations appeared at around 2900 cm^{-1}. The peak at 1640 cm^{-1} was attributed to the O-H bending vibration mode of physisorbed water molecules.[18] Comparing the FTIR spectra of the MSNPs-AgNPs (blue trace) and vinyl-MSNPs-AgNPs (red trace) we note a small new peak at 1402 cm^{-1} in the latter spectrum. We tentatively attribute this feature to the C-H vibrational mode of the vinyl group. The C=C stretching mode of the vinyl group was expected at around 1600 cm^{-1} , however, this band overlaps with the vibrational mode of water molecules.

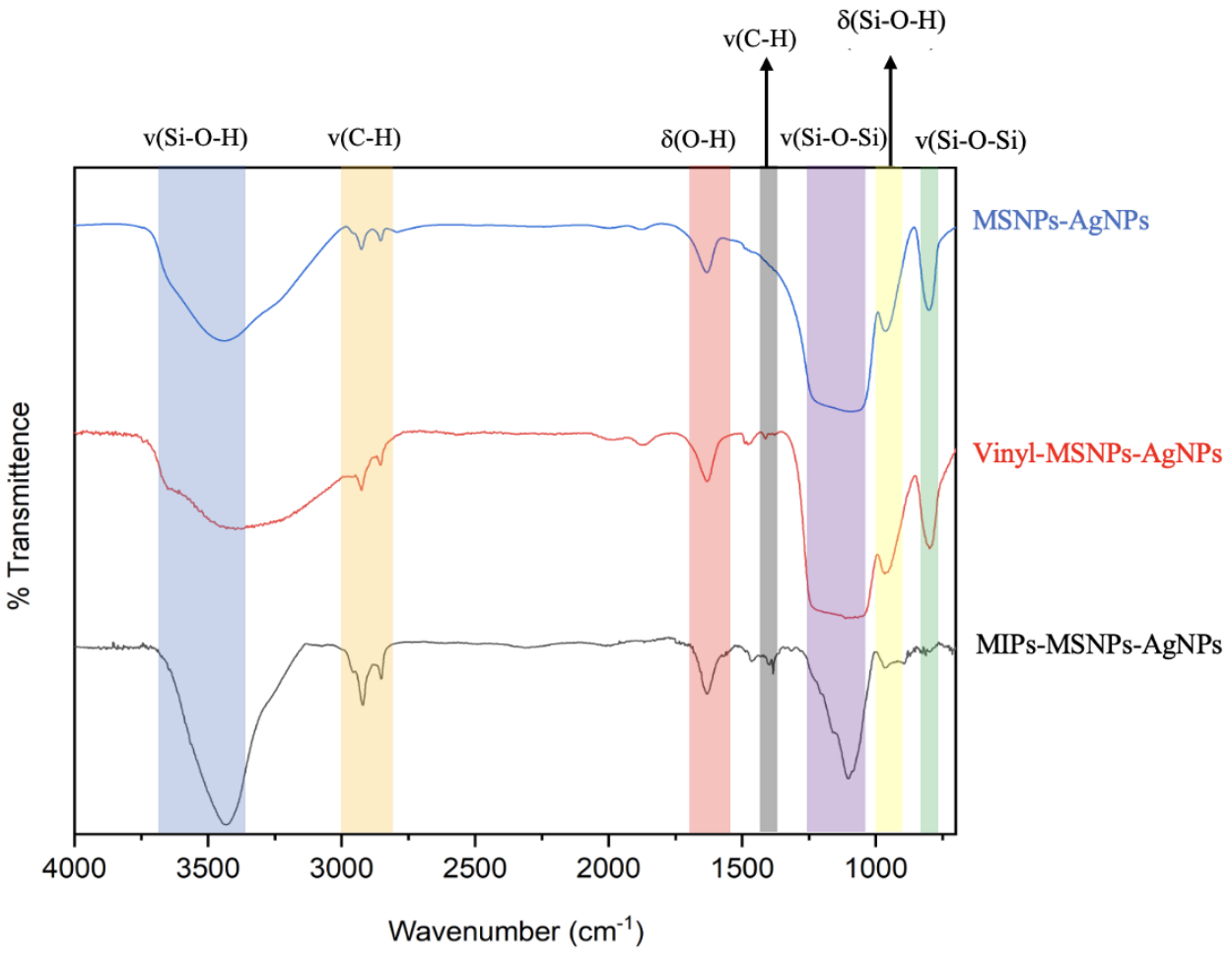

Figure 3.10. FTIR spectra of MSNPs-AgNPs (blue trace), vinyl-MSNPs-AgNPs (red trace) and MIPs-MSNPs-AgNPs (black trace). Samples were acquired as KBr pellets.

To evaluate whether the PNIPAm-co-PAAm copolymer was effectively introduced to the surface of the present particles, the FTIR spectra of the MSNPs-AgNPs (blue trace) and MIPs-MSNPs-AgNPs (black trace) were compared. Characteristic features associated with the PNIPAm-co-PAAm copolymer coating would appear in the range of 1300 – 1750 cm^{-1} (Figure 3.11). The peak at 1640 cm^{-1} is expected to be from the C=O of the polymer. The peak at 1558 cm^{-1} is attributed to the N-H stretching vibration of the NIPAm. The peak at 1517 cm^{-1} is attributed to the N-H stretching vibration of AAm. The peak at 1454 cm^{-1} and the sharp peak at 1384 cm^{-1} are attributed to the C-N stretching vibrations of AAm and NIPAm, respectively. The peak at 1402 cm^{-}

[1] corresponds to the C-H vibrational mode of the vinyl group in the FTIR of vinyl-MSNPs-AgNPs (red trace) in Figure 3.10. The same peak appeared in the MIPs-MSNPs-AgNPs (black trace) which is consistent with the presence of the double bonds on the surface and suggests polymerization reaction was not complete.

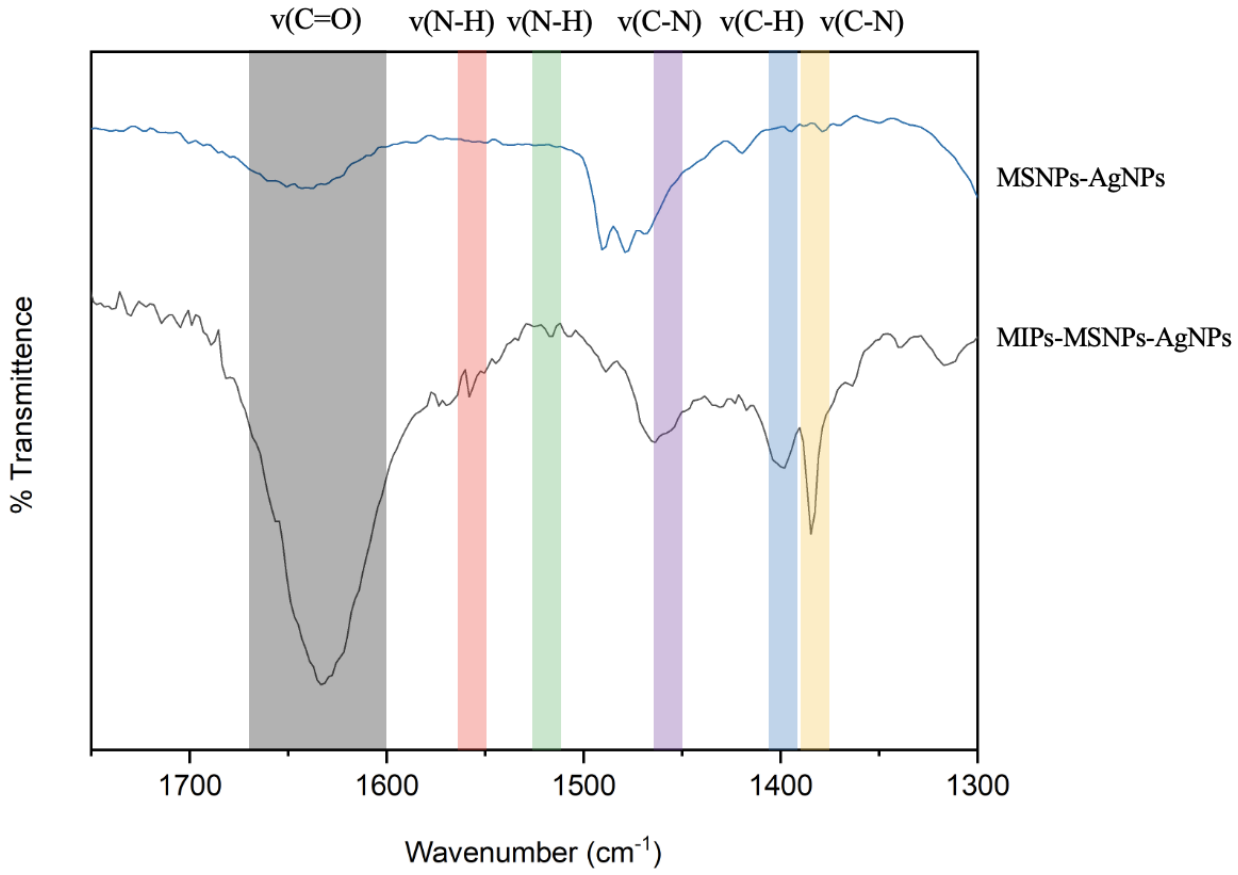

Figure 3.11. FTIR spectrum of MSNPs-AgNPs (blue trace) and MIPs-MSNPs-AgNPs (black trace). Samples were acquired as KBr pellets.

To further investigate the surface functionalization of the present particles TGA performed after each stage of the material synthesis. TGA data for MSNPs-AgNPs, vinyl-MSNPs-AgNPs and MIPs-MSNPs-AgNPs are presented in Figure 3.12. Each sample showed an initial weight loss at 100 °C that we attribute to surface adsorbed water. Comparing the TGA analyses of MSNPs-

AgNPs (a) and vinyl-MSNPs-AgNPs (b), we note a weight loss between 100 and 200 °C in the thermal trace of the later that we propose arises from the thermal decomposition of surface bonded vinyl groups. Finally, a mass loss between 300 and 400 °C is observed for both samples that arises from dehydroxylation of mainly vicinal silanol groups.[19] TGA data in Figure 3.12c for MIPs-MSNPs-AgNPs (without the template) showed a mass loss (7 %) between 200 and 500 °C that is not present in the TGA traces for MSNPs-AgNPs, vinyl-MSNPs-AgNPs and is indicative of the decomposition of the polymer on the surface of the nanoparticles.[20] Figure 3.12d is provided for ease of comparison of the TGA analysis of the presented materials.

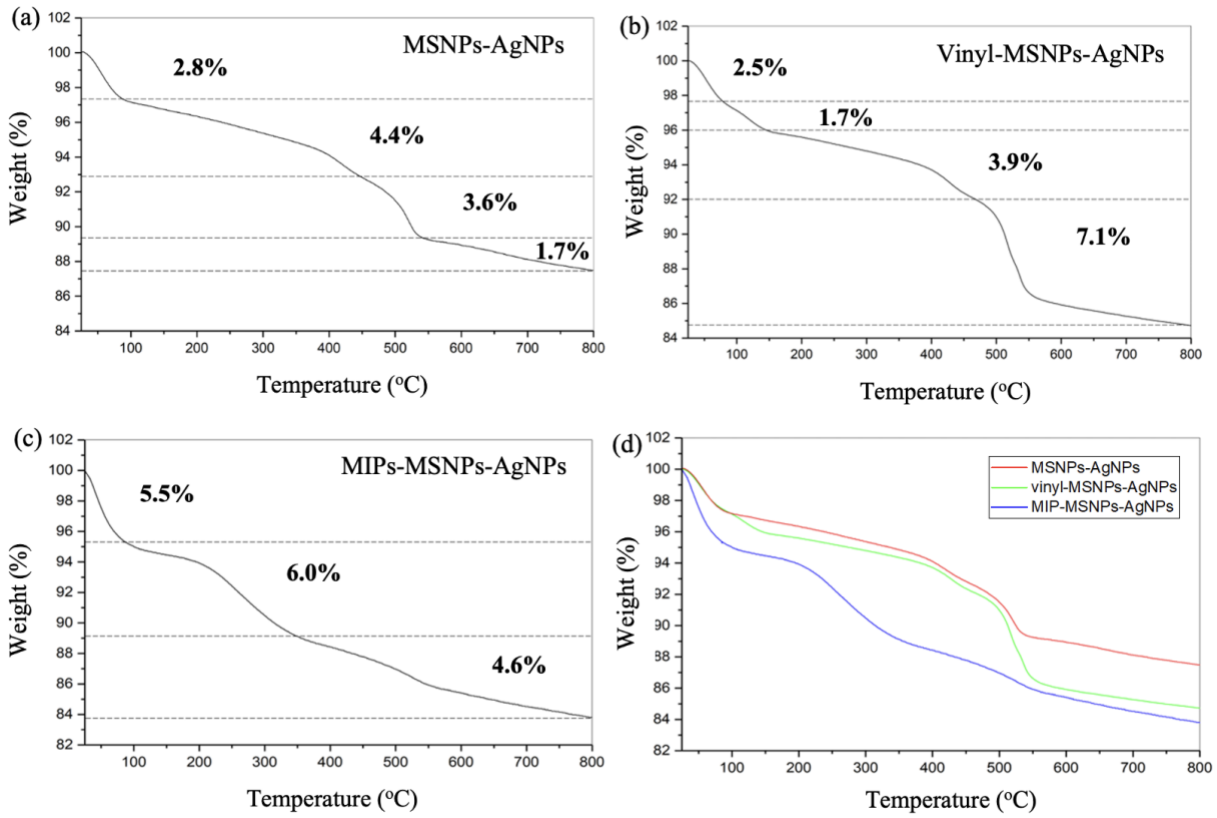

Figure 3.12. TGA data of (a) MSNPs-AgNPs, (b) vinyl-MSNPs-AgNPs, (c) MIPs-MSNPs-AgNPs and (d) Comparison of the TGA data.

To further understand the impact of the changes in surface chemistry from the functionality changes on the surface of the particles, zeta potential was used. Zeta potential measurements were performed for EtOH:H_2O (1:1) suspensions of the parent AgNPs, MSNPs-AgNPs and MIPs-MSNPs-AgNPs (Figure 3.13). AgNPs exhibited a negative surface charge -16.8 mV which is consistent with presence of citrate ions associated with the surfaces of the nanoparticles. Following deposition of the mesoporous silica layer on the surface of the AgNPs to form MSNPs-AgNPs, the zeta potential became -20.4 mV consistent with the surface of the MSNPs-AgNPs being terminated with Si-OH.[5] Finally, coating the surface of the MSNPs-AgNPs with PNIPAm-co-PAAm copolymer, the zeta potential became -18.3 mV. The less negative zeta potential is consistent with a decrease in the amount of Si-OH groups on the surface.

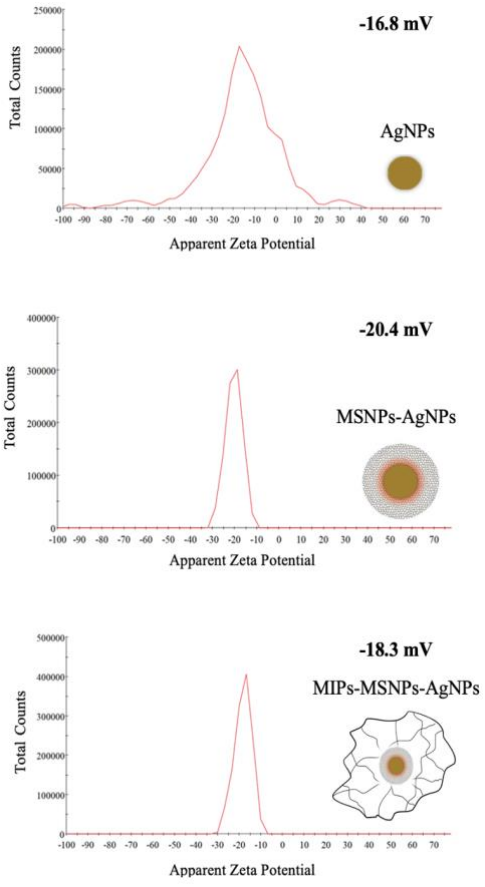

Figure 3.13. Zeta potential data of AgNPs, MSNPs-AgNPs and MIPs-AgNPs-MSNPs.

Finally, MSNPs-AgNPs and MIPs-MSNPs-AgNPs were interrogated using DLS to determine their hydrodynamic size and the size distribution. MSNPs-AgNPs showed a hydrodynamic diameter of 395 nm (Figure 3.14a). MIPs-MSNPs-AgNPs had the hydrodynamic size of 462 nm, consisting of the monodispersed particles (polydispersity index = 0.403) (Figure 3.14b). The increase in the hydrodynamic size upon coating the MSNPs-AgNPs is consistent with a polymer being on the surface of the final nanoparticles. When the SEM images of the MSNPs-AgNPs and MIPs-MSNPs-AgNPs compared, a similar trend in terms of the increase in the size of the particles was observed.

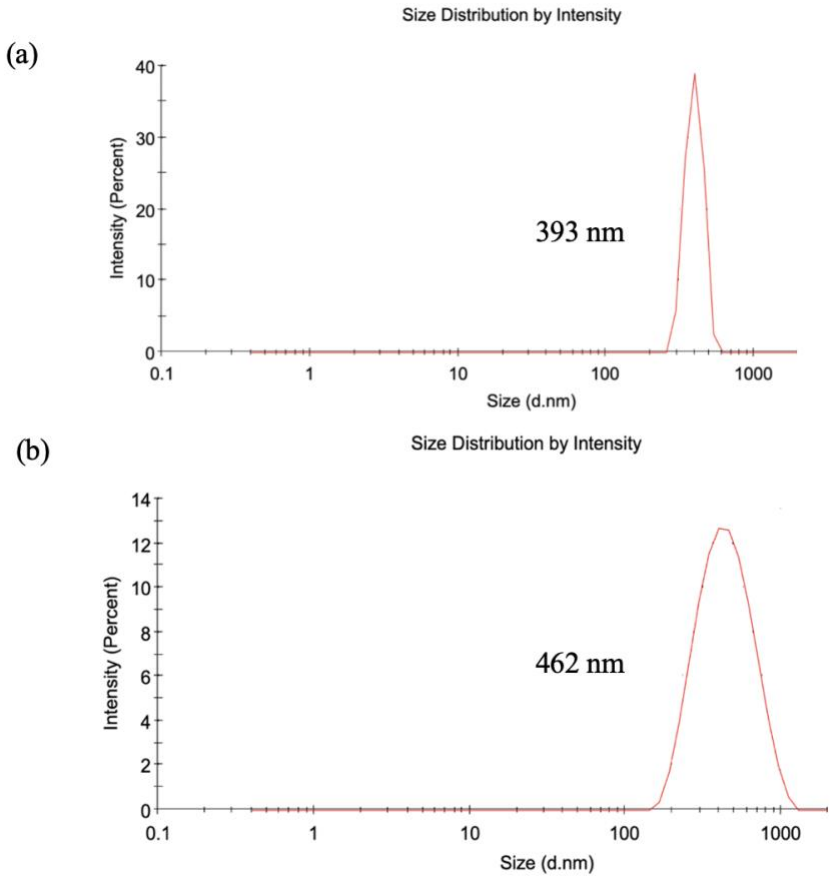

Figure 3.14. DLS size distribution of (a) MSNPs-AgNPs and (b) MIPs-MSNPs-AgNPs.

The MSNPs-AgNPs, vinyl-MSNPs-AgNPs and MIPs-MSNPs-AgNPs were characterized by SEM, EDX spectroscopy, FTIR spectroscopy, TGA, DLS and zeta potential. The functional groups of the particles were characterized by FTIR spectroscopy, showing the presence of characteristic silica vibrations, vinyl functionalization, and surface imprinting. TGA, DLS and zeta potential provided information for the changes in surface functionalization after each synthesis step that indicated the formation of the hybrid material. Next, the possible use of the hybrid material in the drug loading and release applications were investigated.

3.3.4 Urea Uptake by the Surface Imprinted Particles

The MIPs-MSNPs-AgNPs can be loaded with a template, such as urea, using the procedure outlined in Section 3.2.6. Urea uptake was performed while monitoring the mixture of the MIPs-MSNPs-AgNPs and urea by using UV-vis spectroscopy. At predetermined time intervals, the test tube was centrifuged for 5 minutes at 5000 rpm. Subsequently, 100 μL of solution was extracted from the test tube into a vial and distilled water was added until the volume reached to 5 mL for the analysis using UV-vis spectroscopy. Figure 3.15a shows the absorbance of representative aliquots of the supernatant extracted at the specified time intervals. The absorbance at 203 nm for urea was correlated to the concentration of the urea in the mixture and an uptake curve was plotted (Figure 3.15b). The urea concentration decreases over time as the urea was taken up by MIPs-MSNPs-AgNPs. The first measured data point provided a concentration of 3.6 mg/mL even though the initial urea concentration was 5 mg/mL. This suggests an initial rapid uptake of urea by MIPs-MSNPs-AgNPs occurred immediately upon mixing. The adsorption capacity (Q_a) of the MIPs-MSNPs-AgNPs was calculated as 1.98 mg/mg (mg of template absorbed per mg of the adsorbent)

using a method described in literature.[21] The details of this calculation can be found in the Appendix.

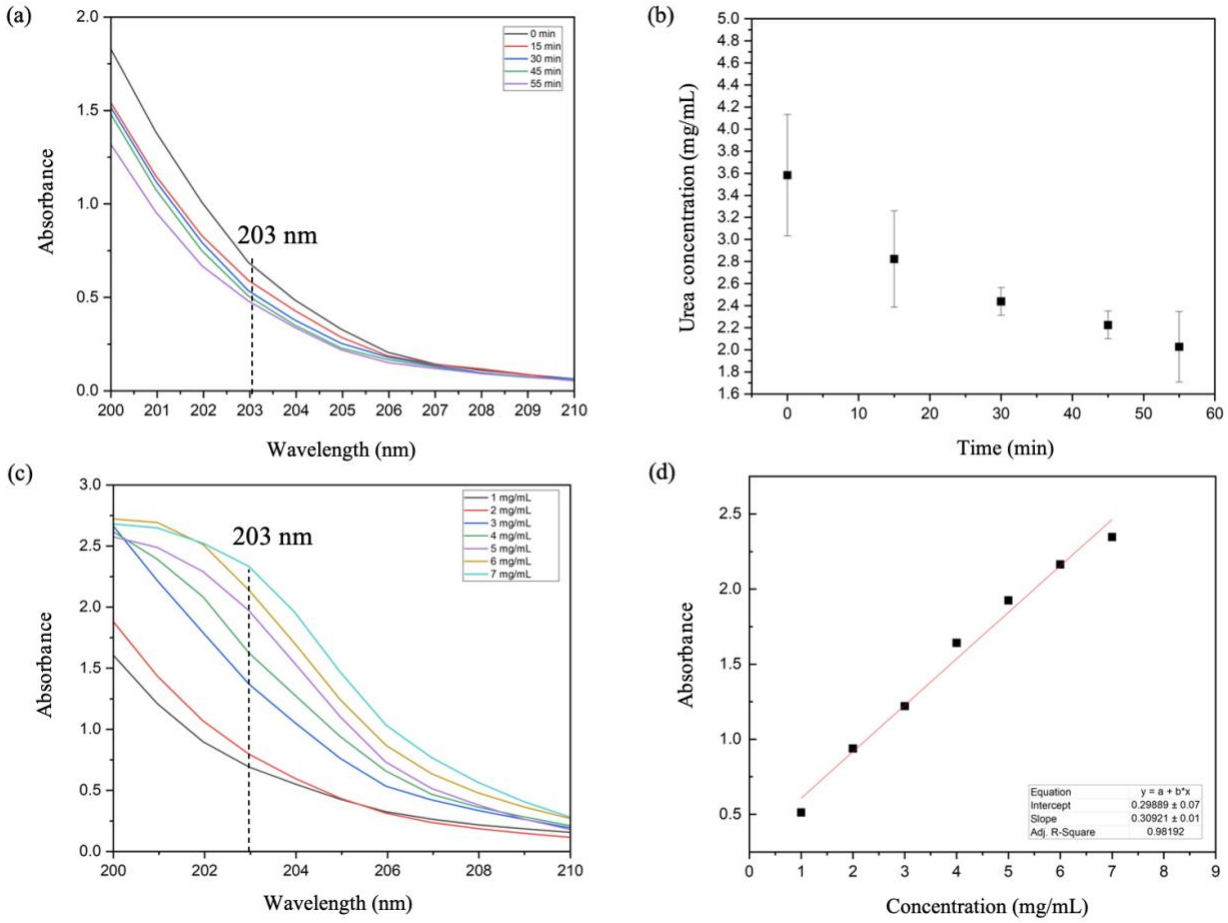

Figure 3.15. Urea uptake by the MIPs-MSNPs-AgNPs; (a) UV-vis spectroscopy data, (b) The relationship between urea concentration in the mixture and exposure/uptake time, (c) UV-vis spectra of the urea standard solutions in different concentrations, (d) Calibration curve of the urea standard solutions. Error bars indicate the standard deviation of the replicates (n = 2 or 3).

3.3.5 Urea Uptake by the Non-imprinted Particles

The uptake experiment was repeated with non-imprinted NIPs-MSNPs-AgNPs using the same procedure outlined in Section 3.2.6. Figure 3.16a shows the absorbance spectra of representative aliquots of the supernatant at predetermined specified time intervals. The

absorbance spectra showed random intensity fluctuations over time. The absorbance at 203 nm characteristic of urea was correlated to the urea concentration in the mixture and an uptake curve was plotted (Figure 3.16b). The concentrations randomly varied within a concentration window (i.e., ca. 3.7 – 4.7 mg/mL) consistent with no preferential or predictable uptake. The adsorption capacity (Q_a) of the NIPs-MSNPs-AgNPs was calculated as 0.708 mg/mg (mg of template absorbed per mg of the adsorbent) using a method described in literature.[21] The details of the calculation can be found in the Appendix. Comparing these observations with those made for the imprinted equivalent material clearly highlight the importance of molecular imprinting to control urea uptake.

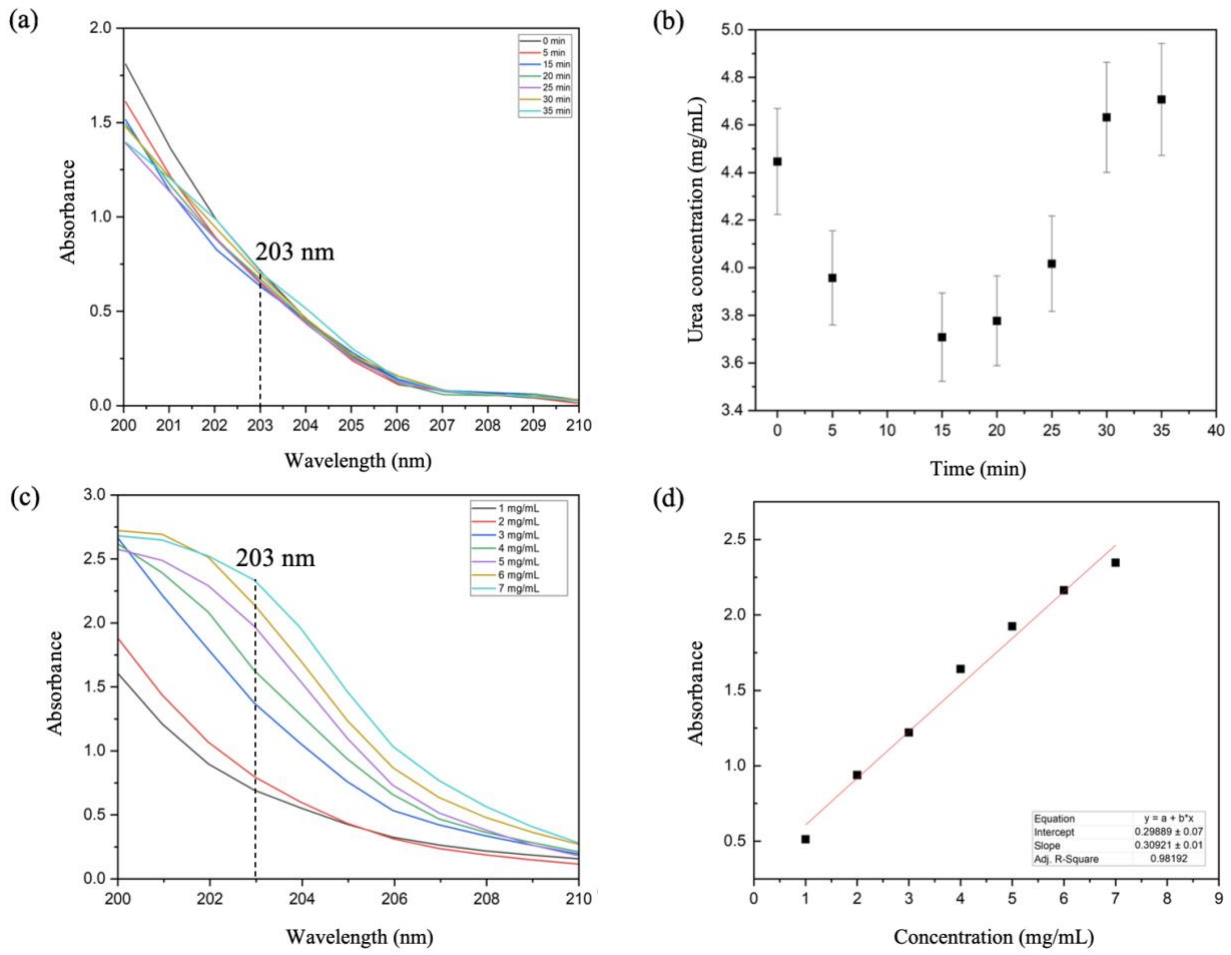

Figure 3.16. Urea uptake of the NIPs-MSNPs-AgNPs; (a) UV-vis spectroscopy data, (b) The relationship between urea concentration in the mixture and exposure/uptake time. (c) UV-vis spectra of urea standard solutions in different concentrations, (d) Calibration curve of urea standard solutions. Error bars indicate the standard deviation of the replicates (n = 2 or 3).

3.3.6 Urea Release by the Imprinted Particles

The release of urea from the loaded particles was performed using the procedure outlined in Section 3.2.6. Figure 3.17a shows the absorbance spectra of aliquots of the supernatant at a predetermined specified time interval. The absorbance intensity at 203 nm, characteristic of urea, increased and then slightly decreased over time. It was used to determine the concentration of urea in the mixture and a release curve was plotted (Figure 3.17b). The initial sharp increase indicated

the release of the urea from the particles into the buffer. The slight decrease after 21 h suggested there may be a slight re-uptake of the urea into the polymer matrix. The maximum concentration of the urea in the mixture was determined to be 0.7 mg/mL. The desorption capacity (Q_d) of the MIPs-MSNPs-AgNPs was calculated as 0.47 mg/mg (mg of template desorbed per mg of the particles) using a method described in literature.[22,23]

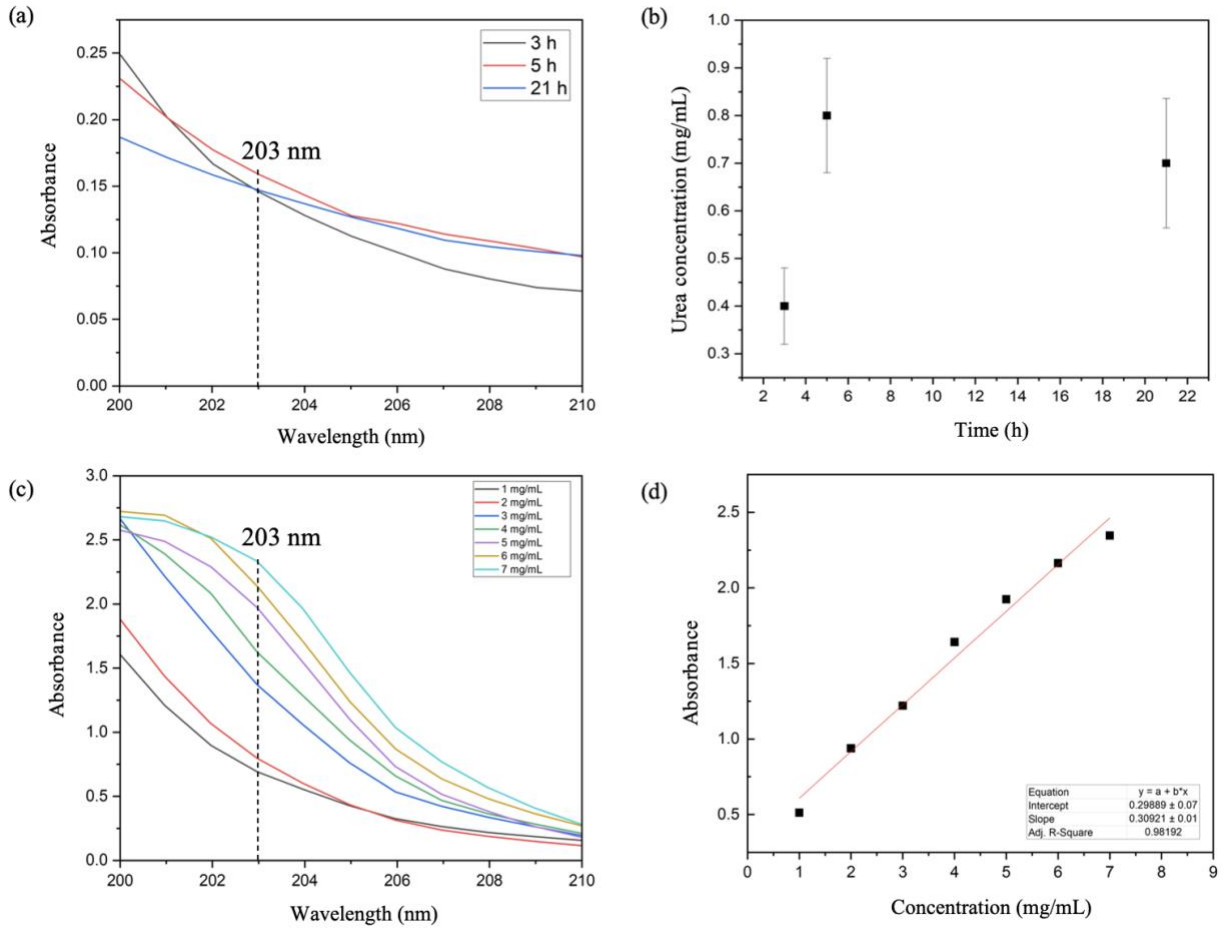

Figure 3.17. Urea release from MIPs-MSNPs-AgNPs; (a) UV-vis spectroscopy data, (b) Correlation to the concentration of urea in the mixture, (c) UV-vis spectrum of urea standard solutions in different concentrations, (d) Calibration curve of urea standard solutions. Error bars indicate the standard deviation of the replicates (n = 2 or 3).

3.3.7 Urea Release by the Non-imprinted Particles

The urea release experiment was repeated using non-imprinted samples (i.e., NIPs-MSNPs-AgNPs) following the procedure outlined in Section 3.2.6. Figure 3.18a shows the absorbance spectra of representative aliquots of the supernatant at the specified time intervals. The absorbance at 203 nm that corresponds to urea was used to determine the concentration of the urea in the mixture using the presented calibration curve and a release curve was plotted (Figure 3.18b). NIPs-MSNPs-AgNPs showed a random behaviour as the concentration of the urea decreased and increased over time. It indicated that the urea was both adsorbed and released. It can be explained by the adsorption of the urea in the non-imprinted polymeric network and then the diffusion into the mixture as the non-imprinted polymer did not have regions imprinted specific to the template molecule. The desorption capacity (Q_d) of the NIPs-MSNPs-AgNPs was calculated as 0.27 mg/mg (mg of template desorbed per mg of the particles) using a method described in literature.[22,23]

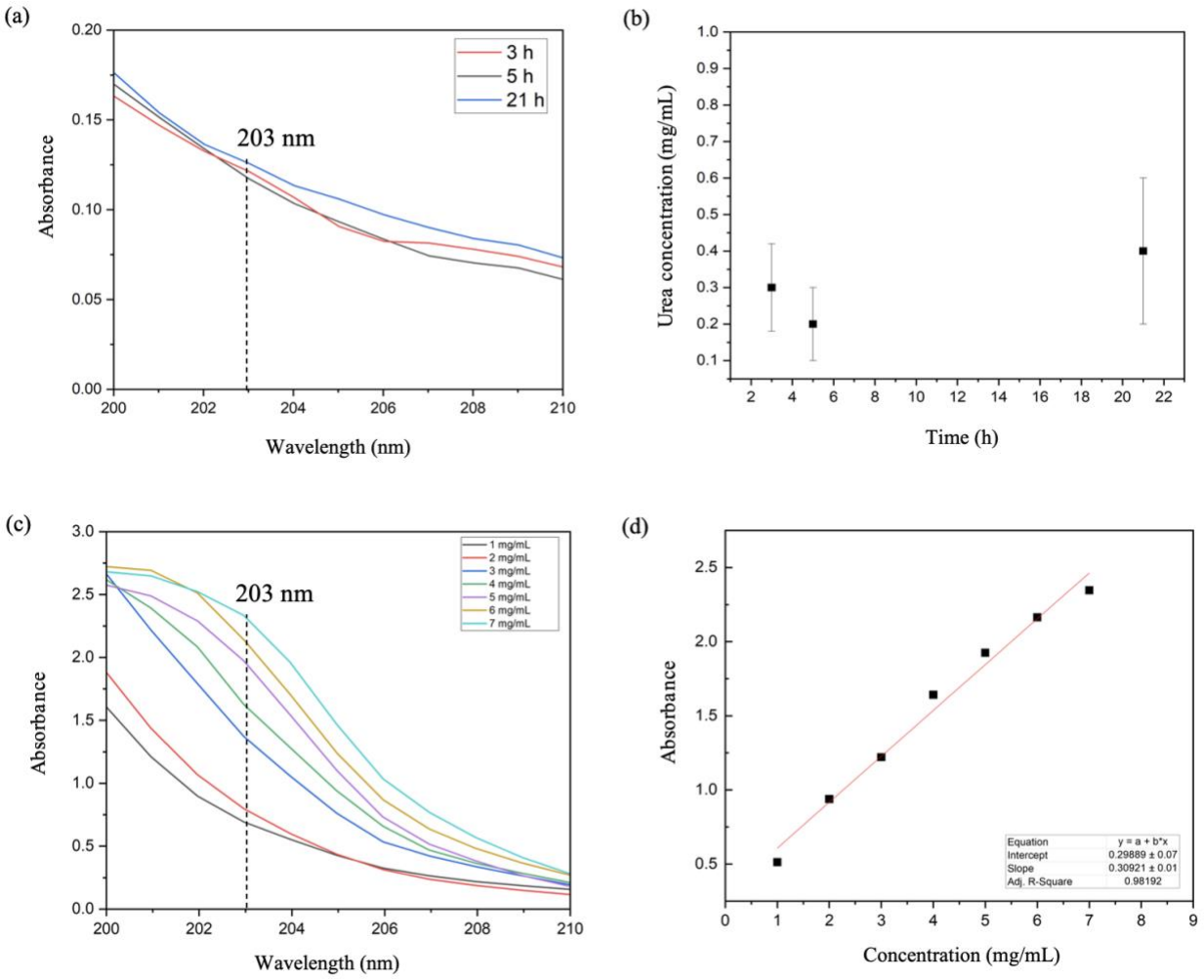

Figure 3.18. Urea release from NIPs-MSNPs-AgNPs; (a) UV-vis spectra, (b) The concentration of urea in the mixture after release, (c) UV-vis spectra of urea standard solutions in different concentrations, (d) Calibration curve prepared using the data presented in c. Error bars indicate the standard deviation of the replicates (n = 2 or 3).

3.3.8 Urea Uptake and Release

Urea uptake and release data of MIPs-MSNPs-AgNPs and NIPs-MSNPs-AgNPs were compared to evaluate the effect of molecular imprinting on the efficiency of uptake and release. The adsorption capacities of MIPs-MSNPs-AgNPs and NIPs-MSNPs-AgNPs for urea was 1.98 mg/mg and 0.71 mg/mg. The MIPs-MSNPs-AgNPs adsorbed larger amounts of urea than NIPs-MSNPs-AgNPs, indicating that there was preferential adsorption of MIPs-MSNPs-AgNPs toward

urea. We propose the selective adsorption occurred due to the presence of recognition sites on the MIPs-MSNPs-AgNPs. The weak adsorption of the urea by NIPs-MSNPs-AgNPs was due to the non-specific interaction with the non-imprinted polymer.

In case of the urea release, the MIPs-MSNPs-AgNPs showed the highest release of the urea in the first 6 h, and the NIPs-MSNPs-AgNPs showed a random release behaviour. Desorption capacity of the MIPs-MSNPs-AgNPs and NIPs-MSNPs-AgNPs was calculated as 0.47 mg/mg and 0.27 mg/mg, respectively.

We propose the that higher amount of urea was taken up by the MIPs-MSNPs-AgNPs compared to NIPs-MSNPs-AgNPs. Similarly, higher amount of urea was released by the MIPs-MSNPs-AgNPs compared to NIPs-MSNPs-AgNPs. These results indicate that surface imprinting provided better control over template uptake and release compared to non-imprinting.

3.4 Conclusions

In this chapter, the preparation and characterization of AgNPs, MSNPs-AgNPs, MIPs-MSNPs-AgNPs and NIPs-MSNPs-AgNPs are described. AgNPs were prepared using a solution-phase chemical reduction method. The AgNPs with pseudospherical shape had an average size of 45.7 ± 6.3 nm. Functional groups on the surfaces of the particles were characterized by FTIR spectroscopy, showing the presence of the characteristic silica vibrations, vinyl functionalization, and characteristic vibrations of the polymer. TGA, DLS and zeta potential provided information for the changes in the surface functionalization after each synthesis step that indicated the formation of the hybrid material. Urea uptake and release experiments were performed using MIPs-MSNPs-AgNPs and NIPs-MSNPs-AgNPs. The results of the uptake and release experiments indicated that surface imprinting provided better control over template uptake and

release compared to non-imprinting. Moreover, the prepared hybrid material that includes the integration of the plasmonic properties of AgNPs, the stability and non-toxicity of MSNPs and the selectivity of MIPs suggests that these materials have potential as a versatile tool in sensing and reagent delivery applications.

3.5 References

(1) Ihtisham, M.; Noori, A.; Yadav, S.; Sarraf, M.; Kumari, P.; Brestic, M.; Imran, M.; Jiang, F.; Yan, X.; Rastogi, A. Silver Nanoparticle's Toxicological Effects and Phytoremediation. *Nanomaterials* **2021**, *11* (9), 1–18.

(2) Beck, F.; Loessl, M.; Baeumner, A. J. Signaling Strategies of Silver Nanoparticles in Optical and Electrochemical Biosensors: Considering Their Potential for the Point-of-Care. *Microchim. Acta* **2023**, *190* (3).

(3) Chandran, S.; Ravichandran, V.; Chandran, S.; Chemmanda, J.; Chandarshekar, B. Biosynthesis of PVA Encapsulated Silver Nanoparticles. *J. Appl. Res. Technol.* **2016**, *14* (5), 319–324.

(4) Schultz, J.; Kirner, F.; Potapov, P.; Büchner, B.; Lubk, A.; Sturm, E. V. Tailoring Plasmonics of Au@Ag Nanoparticles by Silica Encapsulation. *Adv. Opt. Mater.* **2021**, *9* (22), 1–7.

(5) Fathima, H.; Paul, L.; Thirunavukkuarasu, S.; Thomas, K. G. Mesoporous Silica-Capped Silver Nanoparticles for Sieving and Surface-Enhanced Raman Scattering-Based Sensing. *ACS Appl. Nano Mater.* **2020**, *3* (7), 6376–6384.

(6) Leibl, N.; Haupt, K.; Gonzato, C.; Duma, L. Molecularly Imprinted Polymers for Chemical Sensing: A Tutorial Review. *Chemosensors* **2021**, *9* (6), 1–19.

(7) Rui, C.; He, J.; Li, Y.; Liang, Y.; You, L.; He, L.; Li, K.; Zhang, S. Selective Extraction and Enrichment of Aflatoxins from Food Samples by Mesoporous Silica FDU-12 Supported Aflatoxins Imprinted Polymers Based on Surface Molecularly Imprinting Technique. *Talanta*. **2019**, 342–349.

(8) Zhang, W.; He, X. W.; Chen, Y.; Li, W. Y.; Zhang, Y. K. Composite of CdTe Quantum Dots and Molecularly Imprinted Polymer as a Sensing Material for Cytochrome C. *Biosens. Bioelectron.* **2011**, *26* (5), 2553–2558.

(9) Regli, S.; Kelly, J. A.; Barnes, M. A.; Andrei, C. M.; Veinot, J. G. C. Mesoporous Silica Encapsulation of Silicon Nanocrystals: Synthesis, Aqueous Dispersibility and Drug Release. *Mater. Lett.* **2014**, *115*, 21–24.

(10) Murphy, C. J.; Buriak, J. M. Best Practices for the Reporting of Colloidal Inorganic Nanomaterials. *Chem. Mater.* **2015**, *27* (14), 4911–4913.

(11) Amirjani, A.; Firouzi, F.; Haghshenas, D. F. Predicting the Size of Silver Nanoparticles from

Their Optical Properties. *Plasmonics* **2020**, *15* (4), 1077–1082.

(12) Tanaka, A.; Ikeda, S. Adsorption of Dodecyltrimethylammonium Bromide on Aqueous Surfaces of Sodium Bromide Solutions. *Colloids and Surfaces* **1991**, *56* (C), 217–228.

(13) Mariam, J.; Dongre, P. M.; Kothari, D. C. Study of Interaction of Silver Nanoparticles with Bovine Serum Albumin Using Fluorescence Spectroscopy. *J. Fluoresc.* **2011**, *21* (6), 2193–2199.

(14) Ul-Hamid, A. *A Beginners' Guide to Scanning Electron Microscopy* **2018**.

(15) Rasch, R.; Stricher, A.; Truss, R. W. Energy Filtered Low Voltage "in Lens Detector" SEM and XPS of Natural Fiber Surfaces. *J. Appl. Polym. Sci.* **2014**, *131* (9), 1–7.

(16) Feng, H.; Tang, N.; An, M.; Guo, R.; Ma, D.; Yu, X.; Zang, J.; Yang, N. Thermally-Responsive Hydrogels Poly(N-Isopropylacrylamide) as the Thermal Switch. *J. Phys. Chem. C* **2019**, *123* (51), 31003–31010.

(17) Baig, M. M.; Yousuf, M. A.; Alsafari, I. A.; Ali, M.; Agboola, P. O.; Shakir, I.; Haider, S.; Warsi, M. F. New Mesostructured Origami Silica Matrix: A Nano-Platform for Highly Retentive and PH-Controlled Delivery System. *J. Taibah Univ. Sci.* **2021**, *15* (1), 133–144.

(18) Taweekarn, T.; Wongniramaikul, W.; Limsakul, W.; Sriprom, W.; Phawachalotorn, C.; Choodum, A. A Novel Colorimetric Sensor Based on Modified Mesoporous Silica Nanoparticles for Rapid On-Site Detection of Nitrite. *Microchim. Acta* **2020**, *187* (12).

(19) Zhuravlev, L. T. The Surface Chemistry of Amorphous Silica. Zhuravlev Model. *Colloids Surfaces A Physicochem. Eng. Asp.* **2000**, *173* (1–3), 1–38.

(20) Jiang, Y.; Li, G.; Yang, C.; Kong, F.; Yuan, Z. Multiresponsive Cellulose Nanocrystal Cross-Linked Copolymer Hydrogels for the Controlled Release of Dyes and Drugs. *Polymers (Basel).* **2021**, *13* (8).

(21) Shahhoseini, F. Thin Film Molecularly Imprinted Polymers for Environmental and Biological Sample Preparations and Analysis. **2022**.

(22) Yu, Q.; Fan, L.; Li, J. A Novel Process for Asparagus Polyphenols Utilization by Ultrasound Assisted Adsorption and Desorption Using Resins. *Ultrason. Sonochem.* **2020**, *63*, 104920.

(23) Zhang, J.; Zhang, J.; Wang, M.; Wang, M.; Peng, W.; Peng, W.; Chen, Z.; Chen, Z.; Chen, Z.; Chen, Z. Glutathione Surface Molecularly Imprinted Polymer from CLX1180 via Three Modes of Polymerization for Selective Adsorption of Glutathione. *ACS Omega* **2020**, *5* (23), 13777–13784.

(24) Ang, Q. Y.; Zolkeflay, M. H.; Low, S. C. Configuration Control on the Shape Memory Stiffness of Molecularly Imprinted Polymer for Specific Uptake of Creatinine. *Appl. Surf. Sci.* **2016**, *369*, 326–333.

Chapter 4

Conclusions and Future Work

4.1 Conclusions

MSNPs are used in a range of applications including catalysis, drug delivery, controlled release, imaging, and biosensing due to their stability, large pore volumes, high surface area, and non-toxicity.[1] Despite their advantages in biological applications, MSNPs lack favorable optical properties that would be useful for *in-situ* response.[2] To enhance functionality, nanoparticles are often combined with mesoporous silica to create hybrid materials that are particularly useful for biological applications. A significant limitation of these hybrid materials is the non-selective chemical nature of the system - pores of the mesoporous silica cannot selectively target molecules within a given medium. Consequently, molecular imprinting becomes crucial to the imparting of chemical selectivity to these materials. This thesis explores the integration of nanoparticles with surface-imprinted mesoporous silica and investigates the properties of these materials that could lead to future applications.

Chapter 2 describes a synthesis procedure for preparing SiNPs embedded in surface imprinted mesoporous silica. We found that the SiNPs appear in and around MSNPs and the imprinted polymer encapsulates the MSNPs-SiNPs. The results of a IBU release experiments suggested that surface imprinting provided improved control over template release compared to non-imprinted sample.

Drawing inspiration from the synthesis methodology described in Chapter 2, we developed an analogous procedure involving AgNPs that is described in Chapter 3. As expected, we found that AgNPs were on and around the MSNPs and that the imprinted polymer encapsulated the MSNPs-AgNPs. These imprinted MSNPs-AgNPs were investigated for urea uptake and release and showed higher urea uptake compared to NIPs-MSNPs-AgNPs. Similarly, a higher amount of urea was released by the MIPs-MSNPs-AgNPs compared to NIPs-MSNPs-AgNPs. These results suggest that surface imprinting provides some control over template uptake and release compared to non-imprinting.

4.2 Future Directions

4.2.1 Further Characterization

In Chapter 2, one of the reasons for preparing MIPs-MSNPs-SiNPs was to develop hybrid materials with tailorable optical response. Unfortunately, due time constraints these properties were not investigated, optimized, or applied. As such determining the PL properties of the present MIPs-MSNPs-SiNPs is a reasonable target. Once procedures are optimized to provide bright photoluminescence and possible photothermal response the resulting MIPs-MSNPs-SiNPs can be investigated in luminescent cell imaging and selective cell disruption.

Similarly, MIPs-MSNPs-AgNPs prepared in Chapter 3 have target applications as SERS-based sensors (Figure 4.1). This avenue has not been explored and could be achieved by extracting the template molecules that create selective binding sites specific to the template. Subsequently, the template molecules can selectively bind to these cavities and their presence be detected using SERS. The use of the present MIPs-MSNPs-AgNPs in selective SERS detection of target

molecules can introduce new possibilities across various fields, ranging from forensic sciences to biomedical research.

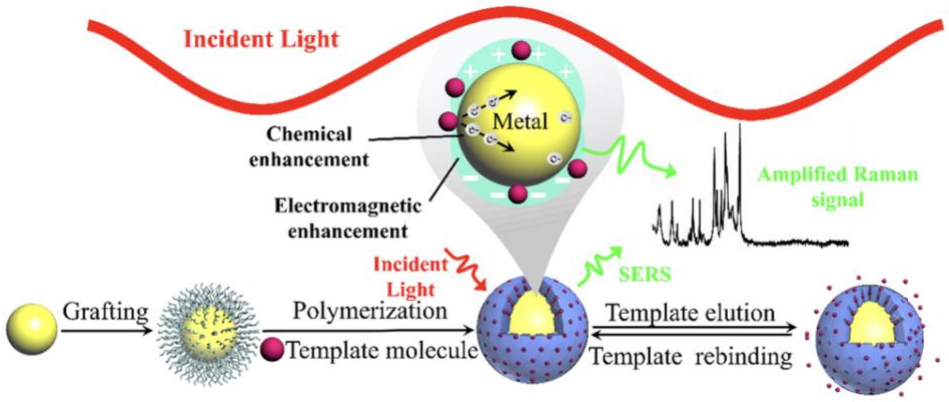

Figure 4.1. Schematic of MIP-SERS sensors construction and enhancement principle. Reprinted (adapted) with permission from Guo, X.; Li, J.; Arabi, M.; Wang, X.; Wang, Y.; Chen, L. Molecular-Imprinting-Based Surface-Enhanced Raman Scattering Sensors. ACS Sensors **2020**, 5 (3), 601–619. Copyright 2020 American Chemical Society.

4.2.2 Investigations involving Drug Delivery and Sensing

To assess the MIPs-MSNPs-SiNPs studied in Chapter 2 as possible drug delivery agents, exploration of the drug release in the cancer cells is an attractive target. Wang et al. demonstrated using EGDMA-based MIPs in targeted drug delivery.[3] The double template-imprinting technique enabled the MIP to carry drugs and achieve precise drug delivery directly to cells. The acidic environment inside cells can disrupt the molecular interactions between the drug molecules and the MIP, resulting in the release of the drug molecules from the MIP. Subsequently, drug molecules accumulate in the cell nucleus, effectively killing them (Figure 4.2). Similarly, MIPs-MSNPs-SiNPs can be dual-imprinted to develop a combined probe for treatment at the cellular level by merging the PL properties of the SiNPs with the selectivity provided by the molecular imprinting method.

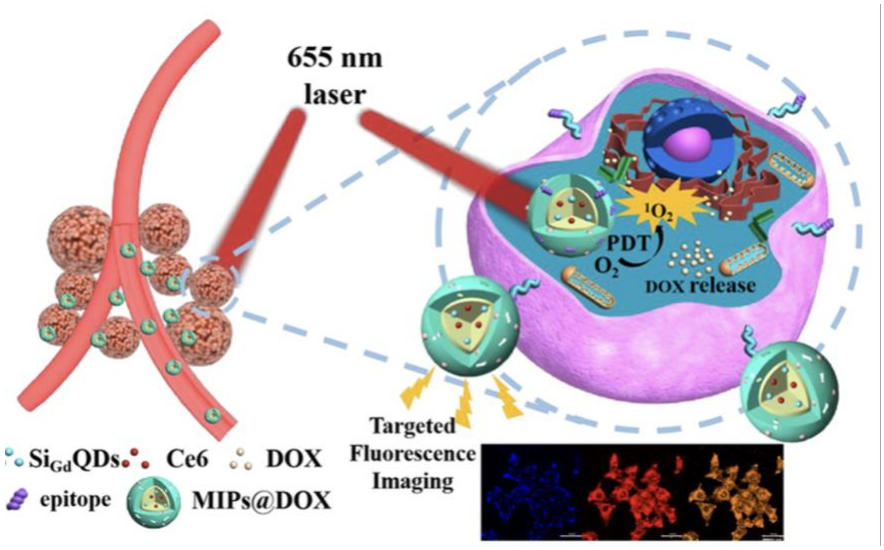

Figure 4.2. The preparation of the MIP for targeted fluorescence imaging and targeted therapy in the cancer cell. Reprinted (adapted) with permission from Peng, H.; Qin, Y. T.; He, Xe. w.; Li, W. Y.; Zhang, Y. K. Epitope Molecularly Imprinted Polymer Nanoparticles for Chemo-/Photodynamics Synergistic Cancer Therapy Guided by Targeted Fluorescence Imaging. ACS Appl. Mater. Interfaces 2020, 12 (11), 13360−13370. Copyright 2020 American Chemical Society.

It is necessary to explore the functionality of the MIPs-MSNPs-AgNPs in in-vivo applications. Photothermal therapy (PTT) have become the focus of research for a variety of cancers.[4] In PTT, light is used to activate a photothermal agent that transforms light energy into heat. PTT offers several benefits including minimal invasiveness, reduced toxicity, improved targeting, and precise control over the timing and location of drug release.[5] The first hypothesis is that the increased temperature around the nanoparticles may lead to cell death. Also, the template release from MIPs may be induced by the PT heating of the AgNPs. Despite there are many studies that hold promise that AgNPs can be used for PTT, challenges remain and more studies are necessary for a deeper understanding of the outcomes, bioaccumulation, and long-term effects of AgNPs in the body.

4.2.3 Selectivity and Reusability of Imprinted Polymers

Selectivity is an essential factor for assessing the recognition capabilities of imprinted polymers.[5] It depends on the arrangement of binding sites and the alignment of functional groups within those sites. There are several methods to determine the selectivity of the MIPs. One method is batch adsorption studies that is based on equilibrating the different concentrations of the template in a suitable solvent with the MIPs. Then, the equilibrium solution concentration is measured, and an adsorption isotherm is constructed (Figure 4.3). The same experiment is also be done with the NIPs. Similar measurements are also made with the likely interfering compounds to compare the equilibrium concentrations of the molecules on the polymer.[6]

Reusability of MIPs is also an important factor in the preparation of economic and sustainable materials.[7] As promising adsorption materials, regeneration ability of the MIPs are very important for practical applications. To test the reusability of MIPs, the adsorption-desorption cycles are done several times using the same MIP particles. Zhi et al. demonstrated that the binding capacity of the MIPs slightly decreased (6.5%) after 5 regeneration cycles.[7] These results indicated the MIPs held great application potential and could be used multiple times without significant decrease in binding capacity.

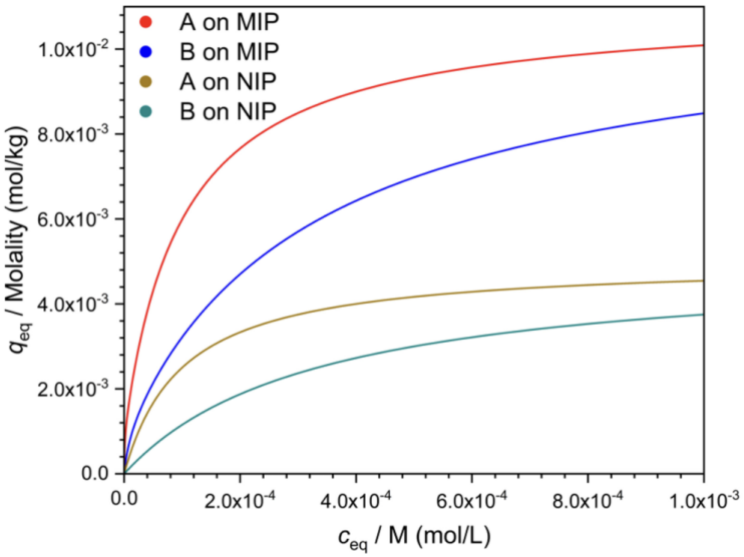

Figure 4.3. Adsorption isotherms of the template (A) and of an interfering compound (B) on the MIPs and NIPs, respectively. c_{eq} and q_{eq} are the equilibrium concentrations in the solution and on the polymer. The curves are constructed using bi-Langmuir and Langmuir models for the MIPs and NIPs, respectively. Adapted from reference 6.

To conclude, further characterization and follow up research can be done to evaluate the drug delivery and the sensing properties of the prepared hybrid materials in Chapter 2 and Chapter 3. Also, the selectivity and reusability of the imprinted materials can be evaluated. This thesis has laid the preliminary groundwork for the preparation of the nanoparticles with the surface imprinted silica to be potentially used in drug delivery and biosensing applications.

4.3 References

(1) Hosseinpour, S.; Walsh, L. J.; Xu, C. Biomedical Application of Mesoporous Silica Nanoparticles as Delivery Systems: A Biological Safety Perspective. *J. Mater. Chem. B* **2020**, *8* (43), 9863–9876.

(2) Xu, B.; Li, S.; Shi, R.; Liu, H. Multifunctional Mesoporous Silica Nanoparticles for Biomedical Applications. *Signal Transduct. Target. Ther.* **2023**, *8* (1).

(3) Peng, H.; Qin, Y. T.; He, Xe. w.; Li, W. Y.; Zhang, Y. K. Epitope Molecularly Imprinted Polymer Nanoparticles for Chemo-/Photodynamics Synergistic Cancer Therapy Guided by Targeted Fluorescence Imaging. *ACS Appl. Mater. Interfaces* **2020**, *12* (11), 13360–13370.

(4) Farzam, O. R.; Mehran, N.; Bilan, F.; Aghajani, E.; Dabbaghipour, R.; Shahgoli, G. A.; Baradaran, B. Nanoparticles for Imaging-Guided Photothermal Therapy of Colorectal Cancer. *Heliyon* **2023**, *9* (11), e21334.

(5) Guo, X.; Li, J.; Arabi, M.; Wang, X.; Wang, Y.; Chen, L. Molecular-Imprinting-Based Surface-Enhanced Raman Scattering Sensors. *ACS Sensors* **2020**, *5* (3), 601–619.

(6) Becskereki, G.; Horvai, G.; Tóth, B. The Selectivity of Molecularly Imprinted Polymers. *Polymers (Basel).* **2021**, *13* (11).

(7) Zhi, K.; Wang, L.; Zhang, Y.; Zhang, X.; Zhang, L.; Liu, L.; Yao, J.; Xiang, W. Preparation and Evaluation of Molecularly Imprinted Polymer for Selective Recognition and Adsorption of Gossypol. *J. Mol. Recognit.* **2018**, *31* (3), 1–9.

Bibliography

Chapter 1

(1) Eberhard, W. G.; Wcislo, W. T. Plenty of Room at the Bottom? *Am. Sci.* **2012**, *100* (3), 226–233.

(2) Madkour, L. H. *Advanced Structured Materials, Nanoelectronic Materials Fundamentals and Applications*, **2019**.

(3) Jin, R.; Higaki, T. Open Questions on the Transition between Nanoscale and Bulk Properties of Metals. *Commun. Chem.* **2021**, *4* (1), 6–9.

(4) Riehle, F. S. The Rational Synthesis of Defect-Free CdE (E = S , Se) Nanocrystals From Precursor Reactivity to Surface Stability, **2016**.

(5) Tibbals, H. F. *Medical Nanotechnology and Nanomedicine, Perspectives in Nanotechnology Series*, **2011**.

(6) Mekuye, B.; Abera, B. Nanomaterials: An Overview of Synthesis, Classification, Characterization, and Applications. *Nano Sel.* **2023**, *4* (8), 486–501.

(7) Zhang, L.; Yang, X.; Yin, Z.; Sun, L. A Review on Carbon Quantum Dots: Synthesis, Photoluminescence Mechanisms and Applications. *Luminescence* **2022**, *37* (10), 1612–1638.

(8) Wang, E. C. W. and A. Z. Targeted Nanoparticles and Their Applications in Biology. *Library (Lond).* **2014**, *6* (1), 576.

(9) Stander, L.; Theodore, L. Environmental Implications of Nanotechnology-an Update. *Int. J. Environ. Res. Public Health* **2011**, *8* (2), 470–479.

(10) García de Arquer, F. P.; Talapin, D. V.; Klimov, V. I.; Arakawa, Y.; Bayer, M.; Sargent, E. H. Semiconductor Quantum Dots: Technological Progress and Future Challenges. *Science* **2021**, *373* (6555).

(11) Verma, S.; Arya, S. *Applications of Quantum Dots in Batteries*; Elsevier Inc., **2021**.

(12) Beard, M. C. Multiple Exciton Generation in Semiconductor Quantum Dots. *J. Phys. Chem. Lett.* **2011**, *2* (11), 1282–1288.

(13) Xiang, X.: Wang, L.; Zhang, J.; Cheng, B.; Yu. J.; Macyk, W. Cadmium Chalcogenide

(CdS, CdSe, CdTe) Quantum Dots for Solar-to-Fuel Conversion. *Adv. Photonics Res.* **2022**, *3* (11).

(14) Yu, K.; Schanze, K. S. Commemorating The Nobel Prize in Chemistry 2023 for the Discovery and Synthesis of Quantum Dots. *ACS Cent. Sci.* **2023**, *9* (11), 1989–1992.

(15) Kargozar, S.; Hoseini, S. J.; Milan, P. B.; Hooshmand, S.; Kim, H. W.; Mozafari, M. Quantum Dots: A Review from Concept to Clinic. *Biotechnol. J.* **2020**, *15* (12), 1–18.

(16) Galstyan, V. "Quantum Dots: Perspectives in next-Generation Chemical Gas Sensors" – A Review. *Anal. Chim. Acta* **2021**, *1152*, 238192.

(17) McVey, B. F. P.; Prabakar, S.; Gooding, J. J.; Tilley, R. D. Solution Synthesis, Surface Passivation, Optical Properties, Biomedical Applications, and Cytotoxicity of Silicon and Germanium Nanocrystals. *Chempluschem* **2017**, *82* (1), 60–73.

(18) Chang, H.; Sun, S. Q. Silicon Nanoparticles: Preparation, Properties, and Applications. *Chinese Phys. B* **2014**, *23* (8).

(19) Delerue, C.; Allan, G.; Lannoo, M. Theoretical Aspects of the Luminescence of Porous Silicon. *Phys. Rev. B* **1993**, *48* (15), 11024–11036.

(20) De Mello Donegá, C. *Nanoparticles: Workhorses of Nanoscience*; 2014; Vol. 9783662448.

(21) Kůsová, K.; Hapala, P.; Valenta, J.; Jelínek, P.; Cibulka, O.; Ondič, L.; Pelant, I. Direct Bandgap Silicon: Tensile-Strained Silicon Nanocrystals. *Adv. Mater. Interfaces* **2014**, *1* (2), 1–9.

(22) Chen, Y.; Tan, C.; Wang, Z.; Miao, J.; Ge, X.; Zhao, T.; Liao, K.; Ge, H.; Wang, Y.; Wang, F.; Zhou, Y.; Wang, P.; Zhou, X.; Shan, C.; Peng, H.; Hu, W. Momentum-Matching and Band-Alignment van Der Waals Heterostructures for High-Efficiency Infrared Photodetection. *Sci. Adv.* **2022**, *8* (30).

(23) Liang, J.; Huang, C.; Gong, X. Silicon Nanocrystals and Their Composites: Syntheses, Fluorescence Mechanisms, and Biological Applications. *ACS Sustain. Chem. Eng.* **2019**, *7* (22), 18213–18227.

(24) Robidillo, C. J. T.; Veinot, J. G. C. Functional Bio-Inorganic Hybrids from Silicon Quantum Dots and Biological Molecules. *ACS Appl. Mater. Interfaces* **2020**, *12* (47), 52251–52270.

(25) Chinnathambi, S.; Chen, S.; Ganesan, S.; Hanagata, N. Silicon Quantum Dots for Biological Applications. *Adv. Healthc. Mater.* **2014**, *3* (1), 10–29.

(26) Zhang, Y.; Cai, N.; Chan, V. Recent Advances in Silicon Quantum Dot-Based Fluorescent

Biosensors. *Biosensors* **2023**, *13* (3), 1–16.

(27) Milliken, S.; Thiessen, A. N.; Cheong, I. T.; O'Connor, K. M.; Li, Z.; Hooper, R. W.; Robidillo, C. J. T.; Veinot, J. G. C. "turning the Dials": Controlling Synthesis, Structure, Composition, and Surface Chemistry to Tailor Silicon Nanoparticle Properties. *Nanoscale* **2021**, *13* (39), 16379–16404.

(28) Hwang, J.; Jeong, Y.; Lee, K. H.; Seo, Y.; Kim, J.; Hong, J. W.; Kamaloo, E.; Camesano, T. A.; Choi, J. Simple Preparation of Fluorescent Silicon Nanoparticles from Used Si Wafers. *Ind. Eng. Chem. Res.* **2015**, *54* (22), 5982–5989.

(29) Clark, R. J.; Aghajamali, M.; Gonzalez, C. M.; Hadidi, L.; Islam, M. A.; Javadi, M.; Mobarok, M. H.; Purkait, T. K.; Robidillo, C. J. T.; Sinelnikov, R.; Thiessen, A. N.; Washington, J.; Yu, H.; Veinot, J. G. C. From Hydrogen Silsesquioxane to Functionalized Silicon Nanocrystals. *Chem. Mater.* **2017**, *29* (1), 80–89.

(30) Yamauchi, Y.; Sakurai, T.; Hirohata, Y.; Hino, T.; Nishikawa, M. Blue Shift of Photoluminescence Spectrum of Porous Silicon by Helium Ion Irradiation. *Vacuum* **2002**, *66* (3–4), 415–418.

(31) Kim, T.; Lee, J. Silicon Nanoparticles: Fabrication, Characterization, Application and Perspectives. *Micro Nano Syst. Lett.* **2023**, *11* (1).

(32) Švrček, V.; Sasaki, T.; Shimizu, Y.; Koshizaki, N. Blue Luminescent Silicon Nanocrystals Prepared by Ns Pulsed Laser Ablation in Water. *Appl. Phys. Lett.* **2006**, *89* (21).

(33) Balachandran, A.; Sreenilayam, S. P.; Madanan, K.; Thomas, S.; Brabazon, D. Nanoparticle Production via Laser Ablation Synthesis in Solution Method and Printed Electronic Application - A Brief Review. *Results Eng.* **2022**, *16*, 100646.

(34) Gupta, A.; Swihart, M. T.; Wiggers, H. Luminescent Colloidal Dispersion of Silicon Quantum Dots from Microwave Plasma Synthesis: Exploring the Photoluminescence Behavior across the Visible Spectrum. *Adv. Funct. Mater.* **2009**, *19* (5), 696–703.

(35) Overview, E. Praxair Material Safety Data Sheet Praxair Material Safety Data Sheet. **2012**, No. March, 1–10.

(36) Wilcoxon, J. P.; Samara, G. A.; Provencio, P. N. Optical and Electronic Properties of Si Nanoclusters Synthesized in Inverse Micelles. *Phys. Rev. B - Condens. Matter Mater. Phys.* **1999**, *60* (4), 2704–2714.

(37) Veinot, J.; Fok, E.; Boates, K.; Macdonald, J. Chemical Safety : LiAlH4 Reduction of SiCl4.

2006, *83* (51), 2006.

(38) Mangolini, L. Synthesis, Properties, and Applications of Silicon Nanocrystals. *J. Vac. Sci. Technol. B, Nanotechnol. Microelectron. Mater. Process. Meas. Phenom.* **2013**, *31* (2).

(39) Cheng, K.; Anthony, R.; Kortshagen, U. R.; Holmes, R. J. High-Efficiency Silicon Nanocrystal Light-Emitting Devices. **2011**, 1952–1956.

(40) Cheng, K. Y.; Anthony, R.; Kortshagen, U. R.; Holmes, R. J. Hybrid Silicon Nanocrystal?Organic Light-Emitting Devices for Infrared Electroluminescence. *Nano Lett.* **2010**, *10* (4), 1154–1157.

(41) Kim, T. W.; Cho, C. H.; Kim, B. H.; Park, S. J. Quantum Confinement Effect in Crystalline Silicon Quantum Dots in Silicon Nitride Grown Using SiH4 and NH3. *Appl. Phys. Lett.* **2006**, *88* (12).

(42) Gonzalez, C. M.; Iqbal, M.; Dasog, M.; Piercey, D. G.; Lockwood, R.; Klapötke, T. M.; Veinot, J. G. C. Detection of High-Energy Compounds Using Photoluminescent Silicon Nanocrystal Paper Based Sensors. *Nanoscale* **2014**, *6* (5), 2608–2612.

(43) Robidillo, C. J. T.; Wandelt, S.; Dalangin, R.; Zhang, L.; Yu, H.; Meldrum, A.; Campbell, R. E.; Veinot, J. G. C. Ratiometric Detection of Nerve Agents by Coupling Complementary Properties of Silicon-Based Quantum Dots and Green Fluorescent Protein. *ACS Appl. Mater. Interfaces* **2019**, *11* (36), 33478–33488.

(44) Robidillo, C. J. T.; Aghajamali, M.; Faramus, A.; Sinelnikov, R.; Veinot, J. G. C. Interfacing Enzymes with Silicon Nanocrystals through the Thiol-Ene Reaction. *Nanoscale* **2018**, *10* (39), 18706–18719.

(45) Su, Y.; Wang, C.; Hong, Z.; Sun, W. Thermal Disproportionation for the Synthesis of Silicon Nanocrystals and Their Photoluminescent Properties. *Front. Chem.* **2021**, *9* (August), 1–17.

(46) Park, J. H.; Gu, L.; Von Maltzahn, G.; Ruoslahti, E.; Bhatia, S. N.; Sailor, M. J. Biodegradable Luminescent Porous Silicon Nanoparticles for in Vivo Applications. *Nat. Mater.* **2009**, *8* (4), 331–336.

(47) Fujioka, K.; Hiruoka, M.; Sato, K.; Manabe, N.; Miyasaka, R.; Hanada, S.; Hoshino, A.; Tilley, R. D.; Manome, Y.; Hirakuri, K.; Yamamoto, K. Luminescent Passive-Oxidized Silicon Quantum Dots as Biological Staining Labels and Their Cytotoxicity Effects at High Concentration. *Nanotechnology* **2008**, *19* (41).

(48) Wang, L.; Nagesha, D. K.; Selvarasah, S.; Dokmeci, M. R.; Carrier, R. L. Toxicity of CdSe Nanoparticles in Caco-2 Cell Cultures. **2012**, *15*, 1–15.

(49) Cheng, X.; Lowe, S. B.; Reece, P. J.; Gooding, J. J. Colloidal Silicon Quantum Dots: From Preparation to the Modification of Self-Assembled Monolayers (SAMs) for Bio-Applications. *Chem. Soc. Rev.* **2014**, *43* (8), 2680–2700.

(50) Ihtisham, M.; Noori, A.; Yadav, S.; Sarraf, M.; Kumari, P.; Brestic, M.; Imran, M.; Jiang, F.; Yan, X.; Rastogi, A. Silver Nanoparticle's Toxicological Effects and Phytoremediation. *Nanomaterials* **2021**, *11* (9), 1–18.

(51) Nie, P.; Zhao, Y.; Xu, H. Synthesis, Applications, Toxicity and Toxicity Mechanisms of Silver Nanoparticles: A Review. *Ecotoxicol. Environ. Saf.* **2023**, *253*, 114636.

(52) Daniel, M. C.; Astruc, D. Gold Nanoparticles: Assembly, Supramolecular Chemistry, Quantum-Size-Related Properties, and Applications Toward Biology, Catalysis, and Nanotechnology. *Chem. Rev.* **2004**, *104* (1), 293–346.

(53) Abou El-Nour, K. M. M.; Eftaiha, A.; Al-Warthan, A.; Ammar, R. A. A. Synthesis and Applications of Silver Nanoparticles. *Arab. J. Chem.* **2010**, *3* (3), 135–140.

(54) Scheibel, H. G.; Porstendörfer, J. Generation of Monodisperse Ag- and NaCl-Aerosols with Particle Diameters between 2 and 300 Nm. *J. Aerosol Sci.* **1983**, *14* (2), 113–126.

(55) Rafique, M.; Rafique, M. S.; Kalsoom, U.; Afzal, A.; Butt, S. H.; Usman, A. Laser Ablation Synthesis of Silver Nanoparticles in Water and Dependence on Laser Nature. *Opt. Quantum Electron.* **2019**, *51* (6), 1–11.

(56) Sportelli, M. C.; Izzi, M.; Volpe, A.; Clemente, M.; Picca, R. A.; Ancona, A.; Lugarà, P. M.; Palazzo, G.; Cioffi, N. The Pros and Cons of the Use of Laser Ablation Synthesis for the Production of Silver Nano-Antimicrobials. *Antibiotics* **2018**, *7* (3).

(57) Khayati, G. R.; Janghorban, K. The Nanostructure Evolution of Ag Powder Synthesized by High Energy Ball Milling. *Adv. Powder Technol.* **2012**, *23* (3), 393–397.

(58) Lotfy, W. A.; Alkersh, B. M.; Sabry, S. A.; Ghozlan, H. A. Biosynthesis of Silver Nanoparticles by Aspergillus Terreus: Characterization, Optimization, and Biological Activities. *Front. Bioeng. Biotechnol.* **2021**, *9*.

(59) Rosman, N. S. R.; Harun, N. A.; Idris, I.; Wan Ismail, W. I. Nanobiotechnology: Nature-Inspired Silver Nanoparticles towards Green Synthesis. *Energy Environ.* **2021**, *32* (7), 1183–1206.

(60) Iravani, S.; Korbekandi, H.; Mirmohammadi, S. V; Zolfaghari, B. Synthesis of Silver Nanoparticles: Chemical, PhysicIravani, S., Korbekandi, H., Mirmohammadi, S. V, & Zolfaghari, B. (2014). Synthesis of Silver Nanoparticles: Chemical, Physical and Biological Methods. Research in Pharmaceutical Sciences, 9(6), 385–406. . *Res. Pharm. Sci.* **2014**, *9* (6), 385–406.

(61) Whitehead, C. B.; Özkar, S.; Finke, R. G. LaMer's 1950 Model of Particle Formation: A Review and Critical Analysis of Its Classical Nucleation and Fluctuation Theory Basis, of Competing Models and Mechanisms for Phase-Changes and Particle Formation, and Then of Its Application to Silver Halide, S. *Mater. Adv.* **2021**, *2* (1), 186–235.

(62) You, H.; Fang, J. Particle-Mediated Nucleation and Growth of Solution-Synthesized Metal Nanocrystals: A New Story beyond the LaMer Curve. *Nano Today* **2016**, *11* (2), 145–167.

(63) Jana, S. Advances in Nanoscale Alloys and Intermetallics: Low Temperature Solution Chemistry Synthesis and Application in Catalysis. *Dalt. Trans.* **2015**, *44* (43), 18692–18717.

(64) Liu, B.; Hu, X. *Hollow Micro- and Nanomaterials: Synthesis and Applications*; Elsevier Inc., **2020**.

(65) Saravanan, M.; Barik, S. K.; MubarakAli, D.; Prakash, P.; Pugazhendhi, A. Synthesis of Silver Nanoparticles from Bacillus Brevis (NCIM 2533) and Their Antibacterial Activity against Pathogenic Bacteria. *Microb. Pathog.* **2018**, *116*, 221–226.

(66) Krajczewski, J.; Kołątaj, K.; Kudelski, A. Plasmonic Nanoparticles in Chemical Analysis. *RSC Adv.* **2017**, *7* (28), 17559–17576.

(67) Zhang, W.; Zi, X.; Bi, J.; Liu, G.; Cheng, H.; Bao, K.; Qin, L.; Wang, W. Plasmonic Nanomaterials in Dark Field Sensing Systems. *Nanomaterials* **2023**, *13* (13).

(68) Wang, L.; Hasanzadeh Kafshgari, M.; Meunier, M. Optical Properties and Applications of Plasmonic-Metal Nanoparticles. *Adv. Funct. Mater.* **2020**, *30* (51), 1–28.

(69) Amirjani, A.; Kamani, P.; Hosseini, H. R. M.; Sadrnezhaad, S. K. SPR-Based Assay Kit for Rapid Determination of Pb2+. *Anal. Chim. Acta* **2022**, *1220* (February), 340030.

(70) Cobley, C. M.; Skrabalak, S. E.; Campbell, D. J.; Xia, Y. Shape-Controlled Synthesis of Silver Nanoparticles for Plasmonic and Sensing Applications. *Plasmonics* **2009**, *4* (2), 171–179.

(71) Chen, J.; Huang, M.; Kong, L. Flexible Ag/Nanocellulose Fibers SERS Substrate and Its

Applications for in-Situ Hazardous Residues Detection on Food. *Appl. Surf. Sci.* **2020**, *533*, 147454.

(72) Zahoor, M.; Nazir, N.; Iftikhar, M.; Naz, S.; Zekker, I.; Burlakovs, J.; Uddin, F.; Kamran, A. W.; Kallistova, A.; Pimenov, N.; Khan, F. A. A Review on Silver Nanoparticles: Classification, Various Methods of Synthesis, and Their Potential Roles in Biomedical Applications and Water Treatment. *Water (Switzerland)* **2021**, *13* (16), 1–28.

(73) Agnihotri, S.; Mukherji, S.; Mukherji, S. Size-Controlled Silver Nanoparticles Synthesized over the Range 5-100 Nm Using the Same Protocol and Their Antibacterial Efficacy. *RSC Adv.* **2014**, *4* (8), 3974–3983.

(74) Ong, W. T. J.; Nyam, K. L. Evaluation of Silver Nanoparticles in Cosmeceutical and Potential Biosafety Complications. *Saudi J. Biol. Sci.* **2022**, *29* (4), 2085–2094.

(75) Nowak, M.; Tolińska, A.; Marciniak, L.; Skrobańska, M.; Tylkowski, B.; Frankowski, M.; Kaczmarek, M. T.; Jastrzab, R. Green Preparation and Characterization of Silver Nanocolloids Used as Antibacterial Material in Soap. *J. Mater. Sci.* **2022**, *57* (18), 8481–8488.

(76) Villanueva, M. E.; Ghibaudo, M. F.; Tovar, G. I.; Copello, G. J.; Campo Dall' Orto, V. Oligomer-Stabilized Silver Nanoparticles for Antimicrobial Coatings for Plastics. *Nano-Structures and Nano-Objects* **2020**, *24*, 100610.

(77) Beck, F.; Loessl, M.; Baeumner, A. J. Signaling Strategies of Silver Nanoparticles in Optical and Electrochemical Biosensors: Considering Their Potential for the Point-of-Care. *Microchim. Acta* **2023**, *190* (3).

(78) Ibrahim, N.; Jamaluddin, N. D.; Tan, L. L.; Yusof, N. Y. M. A Review on the Development of Gold and Silver Nanoparticles-Based Biosensor as a Detection Strategy of Emerging and Pathogenic RNA Virus. *Sensors* **2021**, *21* (15).

(79) Loiseau, A.; Asila, V.; Boitel-Aullen, G.; Lam, M.; Salmain, M.; Boujday, S. Silver-Based Plasmonic Nanoparticles for and Their Use in Biosensing. *Biosensors* **2019**, *9* (2).

(80) Bélteky, P.; Rónavári, A.; Igaz, N.; Szerencsés, B.; Tóth, I. Y.; Pfeiffer, I.; Kiricsi, M.; Kónya, Z. Silver Nanoparticles: Aggregation Behavior in Biorelevant Conditions and Its Impact on Biological Activity. *Int. J. Nanomedicine* **2019**, *14*, 667–687.

(81) Porrang, S.; Davaran, S.; Rahemi, N.; Allahyari, S.; Mostafavi, E. How Advancing Are Mesoporous Silica Nanoparticles? A Comprehensive Review of the Literature. *Int. J.*

Nanomedicine **2022**, *17*, 1803–1827.

(82) Mukhopadhyay, S.; Veroniaina, H.; Chimombe, T.; Han, L.; Zhenghong, W.; Xiaole, Q. Synthesis and Compatibility Evaluation of Versatile Mesoporous Silica Nanoparticles with Red Blood Cells: An Overview. *RSC Adv.* **2019**, 9 (61), 35566-35578.

(83) Bruckner, J. R.; Bauhof, J.; Gebhardt, J.; Beurer, A. K.; Traa, Y.; Giesselmann, F. Mechanisms and Intermediates in the True Liquid Crystal Templating Synthesis of Mesoporous Silica Materials. *J. Phys. Chem. B* **2021**, *125* (12), 3197–3207.

(84) Nagaraj, M. Liquid Crystals Templating. **2020**, *Crystals*, 10, 648, 1–20.

(85) Hoffmann, F.; Fröba, M. Vitalising Porous Inorganic Silica Networks with Organic Functions—PMOs and Related Hybrid Materials. *Chem. Soc. Rev.* **2011**, *40* (2), 608–620.

(86) Steinbach, J. C.; Fait, F.; Mayer, H. A.; Kandelbauer, A. Sol-Gel-Controlled Size and Morphology of Mesoporous Silica Microspheres Using Hard Templates. *ACS Omega* **2023**, *8* (33), 30273–30284.

(87) Vallet-Regí, M.; Schüth, F.; Lozano, D.; Colilla, M.; Manzano, M. Engineering Mesoporous Silica Nanoparticles for Drug Delivery: Where Are We after Two Decades? *Chem. Soc. Rev.* **2022**, *51* (13), 5365–5451.

(88) Yu, X.; Williams, C. T. Recent Advances in the Applications of Mesoporous Silica in Heterogeneous Catalysis. *Catal. Sci. Technol.* **2022**, *12* (19), 5765–5794.

(89) Cashin, V. B.; Eldridge, D. S.; Yu, A.; Zhao, D. Surface Functionalization and Manipulation of Mesoporous Silica Adsorbents for Improved Removal of Pollutants: A Review. *Environ. Sci. Water Res. Technol.* **2018**, *4* (2), 110–128.

(90) Fowler, C. E.; Khushalani, D.; Lebeau, B.; Mann, S. Nanoscale Materials with Mesostructured Interiors. *Adv. Mater.* **2001**, *13* (9), 649–652.

(91) Hosseinpour, S.; Walsh, L. J.; Xu, C. Biomedical Application of Mesoporous Silica Nanoparticles as Delivery Systems: A Biological Safety Perspective. *J. Mater. Chem. B* **2020**, *8* (43), 9863–9876.

(92) Xu, B.; Li, S.; Shi, R.; Liu, H. Multifunctional Mesoporous Silica Nanoparticles for Biomedical Applications. *Signal Transduct. Target. Ther.* **2023**, *8* (1).

(93) Hu, X.; Zrazhevskiy, P.; Gao, X. Encapsulation of Single Quantum Dots with Mesoporous Silica. *Ann. Biomed. Eng.* **2009**, *37* (10), 1960–1966.

(94) Mancini, M. C.; Kairdolf, B. A.; Smith, A. M.; Nie, S. Oxidative Quenching and

Degradation of Polymer-Encapsulated Quantum Dots: New Insights into the Long-Term Fate and Toxicity of Nanocrystals in Vivo. *J. Am. Chem. Soc.* **2008**, *130* (33), 10836–10837.

(95) Moreira, A. F.; Rodrigues, C. F.; Reis, C. A.; Costa, E. C.; Correia, I. J. Gold-Core Silica Shell Nanoparticles Application in Imaging and Therapy: A Review. *Microporous Mesoporous Mater.* **2018**, *270*, 168–179.

(96) Singh, P.; Pandit, S.; Mokkapati, V. R. S. S.; Garg, A.; Ravikumar, V.; Mijakovic, I. Gold Nanoparticles in Diagnostics and Therapeutics for Human Cancer. *Int. J. Mol. Sci.* **2018**, *19* (7).

(97) Li, Z.; Guo, J.; Zhang, M.; Li, G.; Hao, L. Gadolinium-Coated Mesoporous Silica Nanoparticle for Magnetic Resonance Imaging. *Front. Chem.* **2022**, *10*, 1–10.

(98) Alsharif, N. H.; Berger, C. E. M.; Varanasi, S. S.; Chao, Y.; Horrocks, B. R.; Datta, H. K. Alkyl-Capped Silicon Nanocrystals Lack Cytotoxicity and Have Enhanced Intracellular Accumulation in Malignant Cells via Cholesterol-Dependent Endocytosis. *Small* **2009**, *5* (2), 221–228.

(99) Leibl, N.; Haupt, K.; Gonzato, C.; Duma, L. Molecularly Imprinted Polymers for Chemical Sensing: A Tutorial Review. *Chemosensors* **2021**, *9* (6), 1–19.

(100) Belbruno, J. J. Molecularly Imprinted Polymers. *Chem. Rev.* **2019**, *119* (1), 94–119.

(101) Poma, A.; Turner, A. P. F.; Piletsky, S. A. Advances in the Manufacture of MIP Nanoparticles. *Trends Biotechnol.* **2010**, *28* (12), 629–637.

Chapter 2

(1) Ji, X.; Wang, H.; Song, B.; Chu, B.; He, Y. Silicon Nanomaterials for Biosensing and Bioimaging Analysis. *Front. Chem.* **2018**, *6*, 1–9.

(2) Park, J. H.; Gu, L.; Von Maltzahn, G.; Ruoslahti, E.; Bhatia, S. N.; Sailor, M. J. Biodegradable Luminescent Porous Silicon Nanoparticles for in Vivo Applications. *Nat. Mater.* **2009**, *8* (4), 331–336.

(3) Hosseinpour, S.; Walsh, L. J.; Xu, C. Biomedical Application of Mesoporous Silica Nanoparticles as Delivery Systems: A Biological Safety Perspective. *J. Mater. Chem. B* **2020**, *8* (43), 9863–9876.

(4) Regli, S.; Kelly, J. A.; Barnes, M. A.; Andrei, C. M.; Veinot, J. G. C. Mesoporous Silica Encapsulation of Silicon Nanocrystals: Synthesis, Aqueous Dispersibility and Drug Release. *Mater. Lett.* **2014**, *115*, 21–24.

(5) Gagliardi, M. Design and Development of Molecularly Imprinted Biodegradable Polymers for Nanomedicine. *Adv. Ind. Eng. Polym. Res.* **2023**, *6* (4), 396–406.

(6) Leibl, N.; Haupt, K.; Gonzato, C.; Duma, L. Molecularly Imprinted Polymers for Chemical Sensing: A Tutorial Review. *Chemosensors* **2021**, *9* (6), 1–19.

(7) Wang, H. Y.; Cao, P. P.; He, Z. Y.; He, X. W.; Li, W. Y.; Li, Y. H.; Zhang, Y. K. Targeted Imaging and Targeted Therapy of Breast Cancer Cells: Via Fluorescent Double Template-Imprinted Polymer Coated Silicon Nanoparticles by an Epitope Approach. *Nanoscale* **2019**, *11* (36), 17018–17030.

(8) Clark, R. J.; Aghajamali, M.; Gonzalez, C. M.; Hadidi, L.; Islam, M. A.; Javadi, M.; Mobarok, M. H.; Purkait, T. K.; Robidillo, C. J. T.; Sinelnikov, R.; Thiessen, A. N.; Washington, J.; Yu, H.; Veinot, J. G. C. From Hydrogen Silsesquioxane to Functionalized Silicon Nanocrystals. *Chem. Mater.* **2017**, *29* (1), 80–89.

(9) Rui, C.; He, J.; Li, Y.; Liang, Y.; You, L.; He, L.; Li, K.; Zhang, S. Selective Extraction and Enrichment of Aflatoxins from Food Samples by Mesoporous Silica FDU-12 Supported Aflatoxins Imprinted Polymers Based on Surface Molecularly Imprinting Technique. *Talanta* **2019**, 342–349.

(10) Baig, M. M.; Yousuf, M. A.; Alsafari, I. A.; Ali, M.; Agboola, P. O.; Shakir, I.; Haider, S.; Warsi, M. F. New Mesostructured Origami Silica Matrix: A Nano-Platform for Highly Retentive and PH-Controlled Delivery System. *J. Taibah Univ. Sci.* **2021**, *15* (1), 133–144.

(11) Taweekarn, T.; Wongniramaikul, W.; Limsakul, W.; Sriprom, W.; Phawachalotorn, C.; Choodum, A. A Novel Colorimetric Sensor Based on Modified Mesoporous Silica Nanoparticles for Rapid On-Site Detection of Nitrite. *Microchim. Acta* **2020**, *187* (12).

(12) Yu, Q.; Fan, L.; Li, J. A Novel Process for Asparagus Polyphenols Utilization by Ultrasound Assisted Adsorption and Desorption Using Resins. *Ultrason. Sonochem.* **2020**, *63*, 104920.

(13) Zhang, J.; Zhang, J.; Wang, M.; Wang, M.; Peng, W.; Peng, W.; Chen, Z.; Chen, Z.; Chen, Z.; Chen, Z. Glutathione Surface Molecularly Imprinted Polymer from CLX1180 via Three Modes of Polymerization for Selective Adsorption of Glutathione. *ACS Omega* **2020**, *5* (23), 13777–13784.

Chapter 3

(1) Ihtisham, M.; Noori, A.; Yadav, S.; Sarraf, M.; Kumari, P.; Brestic, M.; Imran, M.; Jiang, F.; Yan, X.; Rastogi, A. Silver Nanoparticle's Toxicological Effects and Phytoremediation. *Nanomaterials* **2021**, *11* (9), 1–18.

(2) Beck, F.; Loessl, M.; Baeumner, A. J. Signaling Strategies of Silver Nanoparticles in Optical and Electrochemical Biosensors: Considering Their Potential for the Point-of-Care. *Microchim. Acta* **2023**, *190* (3).

(3) Chandran, S.; Ravichandran, V.; Chandran, S.; Chemmanda, J.; Chandarshekar, B. Biosynthesis of PVA Encapsulated Silver Nanoparticles. *J. Appl. Res. Technol.* **2016**, *14* (5), 319–324.

(4) Schultz, J.; Kirner, F.; Potapov, P.; Büchner, B.; Lubk, A.; Sturm, E. V. Tailoring Plasmonics of Au@Ag Nanoparticles by Silica Encapsulation. *Adv. Opt. Mater.* **2021**, *9* (22), 1–7.

(5) Fathima, H.; Paul, L.; Thirunavukkuarasu, S.; Thomas, K. G. Mesoporous Silica-Capped Silver Nanoparticles for Sieving and Surface-Enhanced Raman Scattering-Based Sensing. *ACS Appl. Nano Mater.* **2020**, *3* (7), 6376–6384.

(6) Leibl, N.; Haupt, K.; Gonzato, C.; Duma, L. Molecularly Imprinted Polymers for Chemical Sensing: A Tutorial Review. *Chemosensors* **2021**, *9* (6), 1–19.

(7) Rui, C.; He, J.; Li, Y.; Liang, Y.; You, L.; He, L.; Li, K.; Zhang, S. Selective Extraction and Enrichment of Aflatoxins from Food Samples by Mesoporous Silica FDU-12 Supported Aflatoxins Imprinted Polymers Based on Surface Molecularly Imprinting Technique. *Talanta* **2019**, pp 342–349.

(8) Zhang, W.; He, X. W.; Chen, Y.; Li, W. Y.; Zhang, Y. K. Composite of CdTe Quantum Dots and Molecularly Imprinted Polymer as a Sensing Material for Cytochrome C. *Biosens. Bioelectron.* **2011**, *26* (5), 2553–2558.

(9) Regli, S.; Kelly, J. A.; Barnes, M. A.; Andrei, C. M.; Veinot, J. G. C. Mesoporous Silica Encapsulation of Silicon Nanocrystals: Synthesis, Aqueous Dispersibility and Drug Release. *Mater. Lett.* **2014**, *115*, 21–24.

(10) Murphy, C. J.; Buriak, J. M. Best Practices for the Reporting of Colloidal Inorganic Nanomaterials. *Chem. Mater.* **2015**, *27* (14), 4911–4913.

(11) Amirjani, A.; Firouzi, F.; Haghshenas, D. F. Predicting the Size of Silver Nanoparticles from Their Optical Properties. *Plasmonics* **2020**, *15* (4), 1077–1082.

(12) Tanaka, A.; Ikeda, S. Adsorption of Dodecyltrimethylammonium Bromide on Aqueous Surfaces of Sodium Bromide Solutions. *Colloids and Surfaces* **1991**, *56* (C), 217–228.

(13) Mariam, J.; Dongre, P. M.; Kothari, D. C. Study of Interaction of Silver Nanoparticles with Bovine Serum Albumin Using Fluorescence Spectroscopy. *J. Fluoresc.* **2011**, *21* (6), 2193–2199.

(14) Ul-Hamid, A. *A Beginners' Guide to Scanning Electron Microscopy*; 2018.

(15) Rasch, R.; Stricher, A.; Truss, R. W. Energy Filtered Low Voltage "in Lens Detector" SEM and XPS of Natural Fiber Surfaces. *J. Appl. Polym. Sci.* **2014**, *131* (9), 1–7.

(16) Feng, H.; Tang, N.; An, M.; Guo, R.; Ma, D.; Yu, X.; Zang, J.; Yang, N. Thermally-Responsive Hydrogels Poly(N-Isopropylacrylamide) as the Thermal Switch. *J. Phys. Chem. C* **2019**, *123* (51), 31003–31010.

(17) Baig, M. M.; Yousuf, M. A.; Alsafari, I. A.; Ali, M.; Agboola, P. O.; Shakir, I.; Haider, S.; Warsi, M. F. New Mesostructured Origami Silica Matrix: A Nano-Platform for Highly Retentive and PH-Controlled Delivery System. *J. Taibah Univ. Sci.* **2021**, *15* (1), 133–144.

(18) Taweekarn, T.; Wongniramaikul, W.; Limsakul, W.; Sriprom, W.; Phawachalotorn, C.; Choodum, A. A Novel Colorimetric Sensor Based on Modified Mesoporous Silica Nanoparticles for Rapid On-Site Detection of Nitrite. *Microchim. Acta* **2020**, *187* (12).

(19) Zhuravlev, L. T. The Surface Chemistry of Amorphous Silica. Zhuravlev Model. *Colloids Surfaces A Physicochem. Eng. Asp.* **2000**, *173* (1–3), 1–38.

(20) Jiang, Y.; Li, G.; Yang, C.; Kong, F.; Yuan, Z. Multiresponsive Cellulose Nanocrystal Cross-Linked Copolymer Hydrogels for the Controlled Release of Dyes and Drugs. *Polymers (Basel).* **2021**, *13* (8).

(21) Shahhoseini, F. Thin Film Molecularly Imprinted Polymers for Environmental and Biological Sample Preparations and Analysis. **2022**.

(22) Yu, Q.; Fan, L.; Li, J. A Novel Process for Asparagus Polyphenols Utilization by Ultrasound Assisted Adsorption and Desorption Using Resins. *Ultrason. Sonochem.* **2020**, *63*, 104920.

(23) Zhang, J.; Zhang, J.; Wang, M.; Wang, M.; Peng, W.; Peng, W.; Chen, Z.; Chen, Z.; Chen, Z.; Chen, Z. Glutathione Surface Molecularly Imprinted Polymer from CLX1180 via Three Modes of Polymerization for Selective Adsorption of Glutathione. *ACS Omega* **2020**, *5*

(23), 13777–13784.

(24) Ang, Q. Y.; Zolkeflay, M. H.; Low, S. C. Configuration Control on the Shape Memory Stiffness of Molecularly Imprinted Polymer for Specific Uptake of Creatinine. *Appl. Surf. Sci.* **2016**, *369*, 326–333.

Chapter 4

(1) Hosseinpour, S.; Walsh, L. J.; Xu, C. Biomedical Application of Mesoporous Silica Nanoparticles as Delivery Systems: A Biological Safety Perspective. *J. Mater. Chem. B* **2020**, *8* (43), 9863–9876.

(2) Xu, B.; Li, S.; Shi, R.; Liu, H. Multifunctional Mesoporous Silica Nanoparticles for Biomedical Applications. *Signal Transduct. Target. Ther.* **2023**, *8* (1).

(3) Peng, H.; Qin, Y. T.; He, Xe. w.; Li, W. Y.; Zhang, Y. K. Epitope Molecularly Imprinted Polymer Nanoparticles for Chemo-/Photodynamics Synergistic Cancer Therapy Guided by Targeted Fluorescence Imaging. *ACS Appl. Mater. Interfaces* **2020**, *12* (11), 13360–13370.

(4) Farzam, O. R.; Mehran, N.; Bilan, F.; Aghajani, E.; Dabbaghipour, R.; Shahgoli, G. A.; Baradaran, B. Nanoparticles for Imaging-Guided Photothermal Therapy of Colorectal Cancer. *Heliyon* **2023**, *9* (11).

(5) Guo, X.; Li, J.; Arabi, M.; Wang, X.; Wang, Y.; Chen, L. Molecular-Imprinting-Based Surface-Enhanced Raman Scattering Sensors. *ACS Sensors* **2020**, *5* (3), 601–619.

(6) Becskereki, G.; Horvai, G.; Tóth, B. The Selectivity of Molecularly Imprinted Polymers. *Polymers (Basel).* **2021**, *13* (11).

(7) Zhi, K.; Wang, L.; Zhang, Y.; Zhang, X.; Zhang, L.; Liu, L.; Yao, J.; Xiang, W. Preparation and Evaluation of Molecularly Imprinted Polymer for Selective Recognition and Adsorption of Gossypol. *J. Mol. Recognit.* **2018**, *31* (3), 1–9.

Appendix

Appendix A

Desorption Capacity

In chapter 2, the desorption capacity of the MIPs-MSNPs-SiNPs and NIPs-MSNPs-SiNPs were calculated using a method described in literature. The calculation was done as follows;

$$Q_d = \frac{(C_d)V}{m}$$

Where Q_d = Desorption capacity

C_d = Concentration of IBU after desorption

V = Volume of the solution

m = Mass of the polymer

Q_d of the MIPs-MSNPs-SiNPs was calculated as 2.07 mg/mg (mg of template desorbed per mg of the particles) when C_d, V and m were 3.1 mg/mL, 10 mL and 15 mg, respectively. Q_d of the NIPs-MSNPs-SiNPs was calculated as 1.40 mg/mg (mg of template desorbed per mg of the particles) when C_d, V and m were 2.1 mg/mL, 10 mL and 15 mg, respectively.

Appendix B

The concentration of AgNPs

In chapter 3, the concentration of the AgNPs were calculated using the method described in literature. The concentration of the AgNPs were calculated by assuming that AgNPs are spherical in shape and considering that the volume ratio of silver atom to AgNPs is 74.1% in the cubic structure. The calculation is as follows;

Radius of a silver atom = 0.144 nm

Volume of a silver atom = $\frac{4}{3}\pi(r)^3$ = 0.0125 nm^3

Volume of AgNPs with the diameter of d (nm) = $\frac{\pi}{6}d^3$

Number of silver atoms (N) in each AgNPs = $\frac{74.1}{100}\ x\ \frac{\pi}{6}d^3\ x\ \frac{1}{0.0125} = 31\ d^3$

The concentration of the AgNPs = $\frac{N_{total}}{NVN_A}$

Where N_{total} = Total number of silver atoms added to the reaction solution

N = Number of silver atoms present in each nanoparticle

V = Volume of the reaction solution in liters

N_A = Avogadro's number

The total number of silver atoms added to the reaction solution (N_{total}) was ($0.4x10^{-3}$) x ($6.02x10^{23}$) atoms. The volume of the reaction solution was 0.157 L.

Adsorption and Desorption Capacity

In chapter 3, the adsorption capacity of the MIPs-MSNPs-AgNPs and NIPs-MSNPs-AgNPs were calculated using a method described in literature. The adsorption capacity is defined as the adsorption of the template molecules at equilibrium from the solution by MIPs-MSNPs-AgNPs or NIPs-MSNPs-AgNPs. The extracted amount is calculated indirectly by determining how much template is left in solution. The calculation was done as follows;

$$Q_a = \frac{(C_o - C_f)V}{m}$$

Where Q_a = Adsorption capacity

C_o = Initial concentration of urea

C_f = Analyzed concentration

V = Volume of the solution

m = Mass of the polymer

The adsorption capacity (Q_a) of the MIPs-MSNPs-AgNPs was calculated as 1.98 mg/mg (mg of template absorbed per mg of the adsorbent) when C_o, C_f, V and m were 5 mg/mL, 2.027 mg/mL, 10 mL and 15 mg, respectively. Q_a of the NIPs-MSNPs-AgNPs was calculated as 0.708 mg/mg (mg of template absorbed per mg of the adsorbent) when C_o, C_f, V and m were 5 mg/mL, 4.707 mg/mL, 10 mL and 15 mg, respectively.

In chapter 3, the desorption capacity of the MIPs-MSNPs-AgNPs and NIPs-MSNPs-AgNPs were calculated using a method described in literature. The calculation was done as follows;

$$Q_d = \frac{(C_d)V}{m}$$

Where Q_d = Desorption capacity

C_d = Concentration of urea after desorption

V = Volume of the solution

m = Mass of the polymer

Q_d of the MIPs-MSNPs-AgNPs and NIPs-MSNPs-AgNPs was calculated as 0.47 mg/mg (mg of template desorbed per mg of the particles) when C_d, V and m were 0.7 mg/mL, 10 mL and 15 mg, respectively. Q_d of the NIPs-MSNPs-AgNPs was calculated as 0.27 mg/mg (mg of template desorbed per mg of the particles) when C_d, V and m were 0.4 mg/mL, 10 mL and 15 mg, respectively.